www.sciencemag.org/cgi/content/full/338/6114/1583/DC1

Supplementary Materials for

Radar-Enabled Recovery of the Sutter's Mill Meteorite, a Carbonaceous Chondrite Regolith Breccia

Peter Jenniskens,* Marc D. Fries, Qing-Zhu Yin, Michael Zolensky, Alexander N. Krot, Scott A. Sandford, Derek Sears, Robert Beauford, Denton S. Ebel, Jon M. Friedrich, Kazuhide Nagashima, Josh Wimpenny, Akane Yamakawa, Kunihiko Nishiizumi, Yasunori Hamajima, Marc W. Caffee, Kees C. Welten, Matthias Laubenstein, Andrew M. Davis, Steven B. Simon, Philipp R. Heck, Edward D. Young, Issaku E. Kohl, Mark H. Thiemens, Morgan H. Nunn, Takashi Mikouchi, Kenji Hagiya, Kazumasa Ohsumi, Thomas A. Cahill, Jonathan A. Lawton, David Barnes, Andrew Steele, Pierre Rochette, Kenneth L. Verosub, Jérôme Gattacceca, George Cooper, Daniel P. Glavin, Aaron S. Burton, Jason P. Dworkin, Jamie E. Elsila, Sandra Pizzarello, Ryan Ogliore, Phillipe Schmitt-Kopplin, Mourad Harir, Norbert Hertkorn, Alexander Verchovsky, Monica Grady, Keisuke Nagao, Ryuji Okazaki, Hiroyuki Takechi, Takahiro Hiroi, Ken Smith, Elizabeth A. Silber, Peter G. Brown, Jim Albers, Doug Klotz, Mike Hankey, Robert Matson, Jeffrey A. Fries, Richard J. Walker, Igor Puchtel, Cin-Ty A. Lee, Monica E. Erdman, Gary R. Eppich, Sarah Roeske, Zelimir Gabelica, Michael Lerche, Michel Nuevo, Beverly Girten, Simon P. Worden (the Sutter's Mill Meteorite Consortium)

*To whom correspondence should be addressed. E-mail: Petrus.M.Jenniskens@nasa.gov

Published 21 December 2012, *Science* **338**, 1583 (2012)
DOI: 10.1126/science.1227163

This PDF file includes:

Supplementary Materials:

Table of Content

1. Fall and Recovery

2. Meteorite Characterization

1. Fall and Recovery

1.1. Trajectory and Orbit

The trajectory of the 14:51:12 – 17 UTC, April 22, fireball was calculated (*49*) based on photographs taken at Rancho Haven, NV, and two videos at Incline Village, NV, and Brush Creek, CA. Astrometric data were obtained by matching the foreground features in each image to those in a similar image containing a star background, taken at a later time. The accuracy of the star background position and orientation is limited by the image resolution, but also by how precise foreground features were matched.

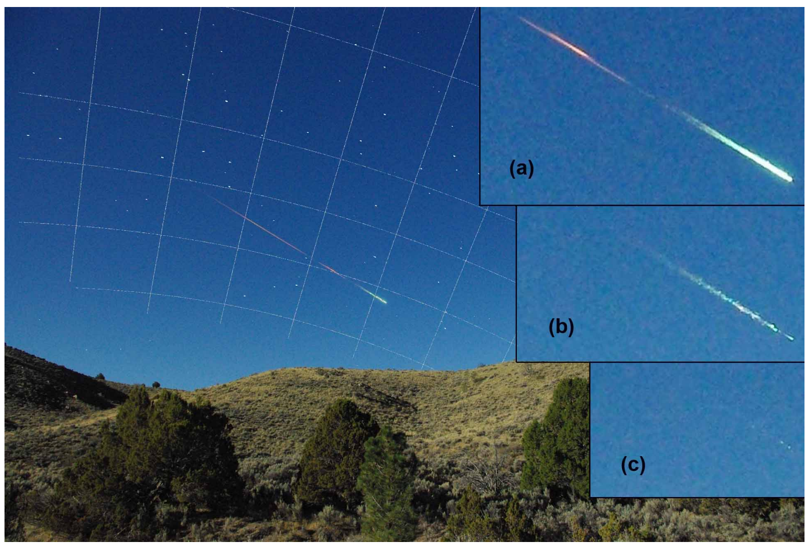

Fig. S1. At Rancho Haven, NV, three photographs were obtained within the time span of two seconds by Lisa Warren from +39º54'24.8"N, 239º59'31.9"E, and 1381m altitude, with a Pentax K200D f = 18 mm Digital Still Camera. Image shows the second photograph taken. A star background image is overlaid as photographed on May 24, 2012 at 4h27m21s UTC. Insets show enlargements of the fragment train in each of the three photographs.

The star background image for the Rancho Haven location (Fig. S1) was taken with the same camera as the fireball photograph. Small perspective differences remained due to an uncertainty of the exact location of the observer. The perspective was matched in azimuth to trees furthest in the field of view. The fireball appeared at a range between 147 and 152 km from the observer.

The Lake Tahoe video (Fig. S2) was saved as 352 × 288 pixel sized video frames. The orientation and scale of the image is fixed by the location of the mountain range and the position of the moon in twilight at three known points in time. A 64º vertical field of view (0.22º/pixel) was fitted with an accuracy of about ±1 pixel, but a possible systematic uncertainty of order 0.4º/pixel may exist. The range to the fireball was a short 94 to 105 km. The meteor is first detected well after fragmentation and is an extended image in each frame. The speed of the leading fragment was measured. Different parts of the fragment train seemed to end at about the same altitude.

Fig. S2. At Incline Village, NV, David Lockard provided this HikVision video security camera footage overlooking Lake Tahoe from +39º14'16.3"N, 240º03'21.6"E, and altitude 1837m. A map of the star background is overlaid as it would appear on May 8, 2012 at 13h04m UTC.

The Brush Creek video (Fig. S3) has detailed and relatively distant foreground features, which were matched in azimuth to ~0.3º accuracy, and ~0.1º in elevation. A different GoPro camera was used to calibrate the image projection, after which the perspective was corrected for lens projection. Star background images were taken with a different camera, which were then used to identify the foreground features in Google maps. The estimated observer position may be off by a few meters. The video shows a steady field, but with some motion jitter. The fireball was 332 - 337 km from the observer. There is overlap with the Rancho Haven photographs: the onset of persistent emission (Fig. S1) is visible in the Brush Creek video towards the end.

Fig. S3. At Brush Creek near Johnsondale, CA, the fireball was filmed by Shon Bollock (http://vimeo.com/41031380) with a fixed position GoPro Hero 2 wide angle video camera at 720p (1280 × 720 pixels, 60 frame/s) from 35º58'25.2"N, 241º31'58.2"E, and altitude 1504m. The image was reprojected in a gnomonic projection. Together with selected frames of the fireball, a map is shown of the reference star background field at 9h25m00s UT on June 3, 2012.

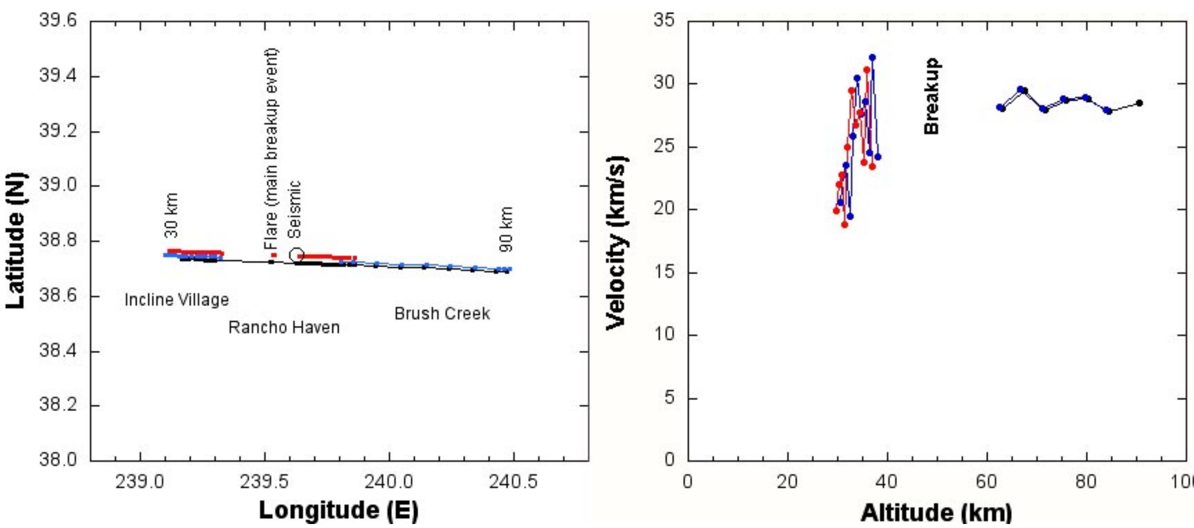

Fig. S4. Left: the ground-projected fireball trajectory from triangulation of combinations Rancho Haven – Lake Tahoe (red), Brush Creek – Rancho Haven (blue), and Lake Tahoe – Brush Creek (black). The position of the blast wave origin derived from seismic measurements is also plotted (o). Right: the measured velocity along the fireball trajectory.

The triangulated trajectories for the combinations Lake Tahoe – Brush Creek (convergence angle between planes from each site: Q = 71.5º), Rancho Haven – Lake Tahoe (Q = 23.2º), and Brush Creek – Rancho Haven (Q = 48.4º) show only a small divergence (Fig. S4). They are in agreement (within uncertainty interval) with the position of the blast wave origin calculated from seismic records. The velocity profile is constant in the Brush Creek video (Fig. S4), but strong deceleration is observed towards the end of the trajectory in the Lake Tahoe video.

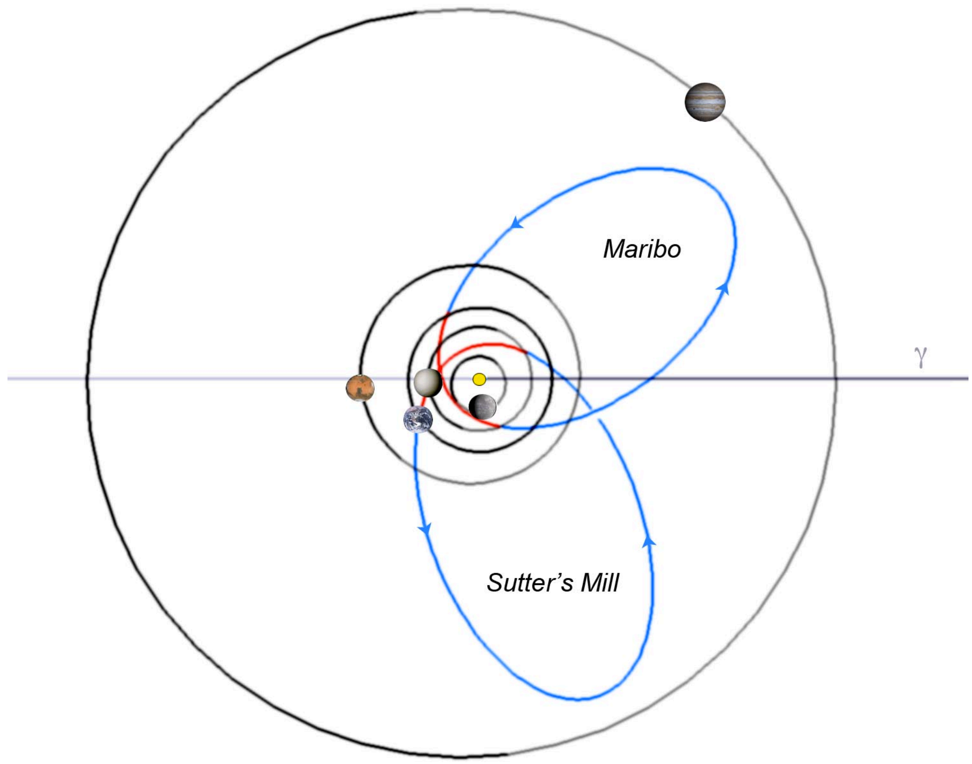

Fig. S5. The preatmospheric orbit of CM chondrites Sutter's Mill and Maribo in the solar system (Table 1, main text). Blue is the part of the orbit below the ecliptic plane, red above. γ is towards the direction of vernal equinox. Planet positions are for 22 April, 2012.

Orbital elements (Table 1, and Fig. S5) were calculated (*49*) based on the mean radiant position of all three solutions, using the standard deviation between solutions as a measure of uncertainty. The orbit prior to entry in Earth's atmosphere is close to that of a Jupiter Family comet, with aphelion just inside of Jupiter's orbit and perihelion near the orbit of Mercury. The asteroid approached Earth from the sunward direction. One node is at Earth's orbit, while the other node is at the orbit of Venus, a feature shared with Maribo (Fig. S5), perhaps because close encounters with the terrestrial planets can de-couple the orbit from the 3:1 resonance.

Table S1 and Fig. S5 compare the Sutter's Mill entry conditions and preatmospheric orbit to that of other meteorite falls derived previously from video and/or photographic observations of the fireball. Sutter's Mill and Maribo stand out by having a low perihelion distance of 0.45 AU, with most other falls having values in the range 0.78-1.00 AU. The entry velocity is twice that of most other falls. The distribution of semimajor axis has two peaks, roughly corresponding to the 3:1 mean-motion resonance (2.5 AU) and the ν_6 resonance (2.1 AU).

Table S1. Overview of known meteorite falls with atmospheric trajectory and orbit determinations from photographic and video data (Equinox J2000).

Fall Date (UT)	Meteorite name (location)	Mv at 100km (magn.)	Initial Velocity (km/s)	Entry Angle (º)	Start Alt. (km)	Peak Alt. (km)	Final Alt. (km)	Final Vel. (km/s)	D (m)	Ekin (kt)	Ref.
4/22/2012	Sutter's Mill (California)	-18.3	28.6	26.3	90.2	47.6	30.1	19	3.0	4.0	This
4/13/2010	Mason Gully (Australia)	-9.4	14.53	53.9	83.46	35.8	23.84	4.1	0.3	0.001	(*50*)
9/26/2009	Grimsby (Canada)	-14.5	20.91	55.2	100.5	39	19.6	3.1	0.18	0.002	(*51*)
4/9/2009	Jesenice (Slovenia)	-15	13.78	40.6	88	26	15.3	3.0	0.4	0.004	(*52*)
1/17/2009	Maribo (Denmark)	-16.5	28.0	30.2	111.8	58	32	-.-	1.0	0.08	(*53-54*)
11/21/2008	Buzzard Coulee (Canada)	-15	18.0	66.7	86	-.-	<17.6	-.-	1.4	0.32	(*55*)
7/10/2008	Almahata Sitta (Sudan)	-20	12.42	20	65	37.5	32.7	-.-	4.1	1.2	(*56-57*)
7/20/2007	Bunburra Rockhole (Aus.)	-9.6	13.36	-.-	62.8	-.-	29.95	5.8	0.3	0.001	(*58-59*)
1/4/2004	Villalbeto de la Pena (Sp.)	-18	16.9	29.0	47	28	22.20	7.8	0.8	0.02	(*60*)
3/27/2003	Park Forest (Illinois)	-21.7	19.5	29	82	28	<18	-.-	1.3	0.5	(*61*)
4/6/2002	Neuschwanstein (Germ.)	-17.2	20.95	49.5	84.95	21	16.04	2.4	0.45	0.026	(*62*)
5/6/2000	Morávka (Czech Rep.)	-20.0	22.5	20.4	80	33	21.2	3.7	1.0	0.1	(*63*)
1/18/2000	Tagish Lake (Canada)	-22	15.8	17.8	-.-	38	31	9	4	1.7	(*64*)
10/9/1992	Peekskill (New York)	-16	14.72	80	3.4	-.-	33.6	-.-	1.2	0.5	(*65*)
5/7/1991	Benesov (Czech Republic)	-19.5	21.0	-.-	-.-	34	19	5	1.6	0.2	(*66*)
2/6/1977	Innisfree (Alberta)	-12.1	14.54	67.8	>62	36	21	4.7	0.19	0.0005	(*67-68*)
1/4/1970	Lost City (Oklahoma)	-12	14.15	38	86	28	19.5	3.4	0.3	0.004	(*69-70*)
4/7/1959	Pribram (Czech Republic)	-19.2	20.89	43	98	46	13.3	-.-	1.8	0.5	(*62,71*)

Fall Date (UT)	Meteorite name (location)	Type	q (AU)	a (AU)	e	i (º)	ω (º)	Node (º)	CRE (My)	Mrec (kg)
4/22/2012	Sutter's Mill (California)	CM2	0.456	2.59	0.824	2.38	77.8	32.774	0.05	0.94
4/13/2010	Mason Gully (Australia)	H5	0.9824	2.470	0.6023	0.832	18.95	203.211	-.-	0.024
9/26/2009	Grimsby (Canada)	H4-6	0.9817	2.04	0.518	28.07	159.865	182.956	-.-	0.215
4/9/2009	Jesenice (Slovenia)	L6	0.998	1.75	0.43	9.6	190.5	19.2	4	3.6
1/17/2009	Maribo (Denmark)*	CM2	0.481	2.34	0.795	0.72	99.0	117.638	~1	0.026
11/21/2008	Buzzard Coulee (Canada)	H4	0.961	1.225	0.215	25.49	212.02	238.937	-.-	41
7/10/2008	Almahata Sitta (Sudan)	Ur	0.9000	1.3082	0.4536	2.5422	234.450	194.101	20	11
7/20/2007	Bunburra Rockhole (Aust.)	Eu	0.643	0.851	0.245	9.07	209.9	297.595	-.-	0.34
1/4/2004	Villalbeto de la Pena (Sp.)	L6	0.860	2.3	0.63	0.0	132.3	283.671	48	5.2
3/27/2003	Park Forest (Illinois)	L5	0.811	2.53	0.680	3.2	237.5	6.116	-.-	18
4/6/2002	Neuschwanstein (Germ.)	EL6	0.793	2.40	0.670	11.41	241.20	16.827	48	6.2
5/6/2000	Morávka (Czech Rep.)	H5	0.982	1.85	0.47	32.2	203.5	46.258	6.7	1.4
1/18/2000	Tagish Lake (Canada)	C2 ung	0.884	1.98	0.55	2.0	224.4	297.901	7.8	10
10/9/1992	Peekskill (New York)	H6	0.886	1.49	0.41	4.9	308	17.030	32	12.37
5/7/1991	Benešov (Czech Republic)	LL3.5	0.9246	2.427	0.6191	23.70	218.67	47.001	-.-	0.009
2/6/1977	Innisfree (Alberta)	L5	0.986	1.872	0.473	12.28	177.97	317.52	26	4.58
1/4/1970	Lost City (Oklahoma)	H5	0.933	1.66	0.417	11.98	161.00	283.77	8	17.2
4/7/1959	Pribram (Czech Republic)	H5	0.7895	2.401	0.6711	10.482	241.75	17.791	12	5.7

*) Orbit calculated from seven Juliusruh radar head-echo detections: January 17, 2009, 19:08:27.50 UT: altitude calculated from range = 111.80 km, azimuth (anti-clock from E) = 347.56º; 19:08:27.57, 110.0 km, 346.18º; 19:08:27.93, 105.45 km, 344.61º; 19:08:29.01, 90.65 km, 182.70º; 19:08:29.15, 87.97 km, 181.08º; 19:08:29.49, 83.69 km, 178.84º; 19:08:29.79, 79.02 km, 177.64º.

1.2. Infrasound and Seismic Data

Two infrasound stations detected the infrasound signal from the Sutter's Mill fireball. Both recorded an unusually long period (Table S2a) signal, normally associated with very large kiloton (kt) class detonations. The signal period and frequency content of the infrasound signals, given the relatively large range to the fireball, suggest a source energy >> 0.1 kt. Based on the period a best fit source energy is 4.0 (-2.2 +3.4) kt of TNT. The underlying theory (5) relates the observed period to the blast radius, which is a function of speed and diameter of the body. The uncertainty interval is mostly due to the scatter in the empirical period relationship, precise to about a factor of two. The small measured difference in period between the two stations is typical of other falls and usually attributed to the signal coming from different parts of the trail. A signal coming from a point along the trajectory where fragmentation occurs will give a larger blast radius and consequently longer period. Additionally, sources located at higher altitudes tend to produce larger periods for fixed energy release.

The amplitude-based relations do not provide consistent results for Sutter's Mill, perhaps an indication of unusual behavior. In particular, the steep topography in Western North America could lead to caustics and scattering which together with uncertainties in general atmospheric conditions and propagation introduce large error factors in the final energy estimates from amplitude alone. Period measurements are much less affected by these effects.

Table S2a. Summary of Sutter's Mill bolide infrasound signal measurements. The signal measurement methodology is described in (*5*).

Station	Range (km)	Arrival time (hh:mm:ss)	Delay time (s)	Signal Celerity (km/s)	Maximum Amplitude (Pa)	Max Peak to Peak Amplitude (Pa)	Trace Velocity (km/s)
I57US	768	15:30:24	2364	0.325	0.094 ± 0.013	0.144 ± 0.026	0.367
I56US	1077	15:50:40	3580	0.301	0.151 ± 0.030	0.308 ± 0.060	0.353

Station	Period at Maximum Amplitude (s)	Frequency at Maximum PSD (Hz)	Period at Maximum PSD (s)	Total Duration (s)	Total Signal Energy (Pa^2)	Integr. Energy SNR	Observed Back Azimuth (deg)
I57US	8.7 ± 1.3	0.14	7.19	539	0.17	6.79	323.5
I56US	6.4 ± 0.2	0.13	7.52	794	0.79	22.86	196.4

Table 2b. Summary of the arrival times of the impulsive phase at seismic stations. Dist.: Distance from station to source; Az.: Source to station azimuth (surface projection); Ang.: Take off angle, source to station; Res.: Travel time residual in seconds relative to assumed velocity model; Wt.: Travel time weighting factor.

Station	Lat.	Lon.	Elev. (m)	Arrival Time	Dist. (km)	Az. (º)	Ang. (º)	Res. (s)	Wt.
EMB	38º58.48'	120º06.17'	2134	14:54:31.13	30.6	31	149	+1.55	0.99
RUB	39º03.10'	120º09.29'	2045	14:54:38.83	36.5	18	145	-0.97	1.00
EBP	38º34.96'	119º48.44'	2432	14:54:59.15	45.2	112	139	+0.18	1.00
TAH	39º09.09'	120º09.78'	2079	14:55:44.63	47.0	13	138	-1.61	0.98
MPK	39º17.57'	120º02.18'	2599	14:54:57.03	65.2	19	128	+1.33	0.99
EGLV	39º09.47'	119º43.24'	1435	14:55:47.90	67.6	46	127	-1.47	0.99
SLID	39º18.86'	119º53.03'	2929	14:56:18.36	72.8	28	125	+0.90	1.00
CMB	38º02.07'	120º23.19'	697	14:56:03.62	78.7	187	123	-0.05	1.00

The source location of the seismic signals, assumed to be a point source, was developed from first arrivals at 8 seismic stations along the eastern Sierra and in western Nevada (Table 2b). Seven stations are part of the Nevada seismic network (*8*). Travel time residuals from one California station operated by UC Berkeley, station CMB - Columbia College, helped define the location. The location of the source was calculated from the impulsive arrival in the wave train by using a half-space sound velocity of 310 m/s (consistent with -25ºC). Impulsive arrivals from stations to the west and stations to the east did not converge well, possibly due to directivity of the wave front following the explosion. Also, the wave train is fairly complex, possibly from multi-pathing of the surface arrival and because many of the stations are on variable topography. The result is a point source location at +38.7390N, 120.2865W (Fig. S4), with uncertainty of ±5.4 km horizontal error, and an elevation of 54.8 km MSL with ±10.9 km vertical error. The origin time was April 22, 2012, at 14:51:12.80 ± 1.15 s UTC.

1.3. Doppler Weather Radar Return

Figure S6 shows the progression of the falling meteorites in altitude and time. This plot shows all radar data from the three nearest NEXRAD radars. Open squares indicate radar sweeps that do not show evidence of falling meteorites, while solid squares indicate radar sweeps with excess reflectivity over the Lotus and Coloma area. The first radar reflections were detected at 14:52:10

UTC at 16.8 km above ground level by KRGX. These records are shown compared against the calculated fall curves for a range of meteorite masses, using a dark flight model that calculated meteorite fall using ambient winds-aloft measurements made by a weather balloon launched from Reno, NV at 12:00 UTC on the day of the Sutter's Mill fall.

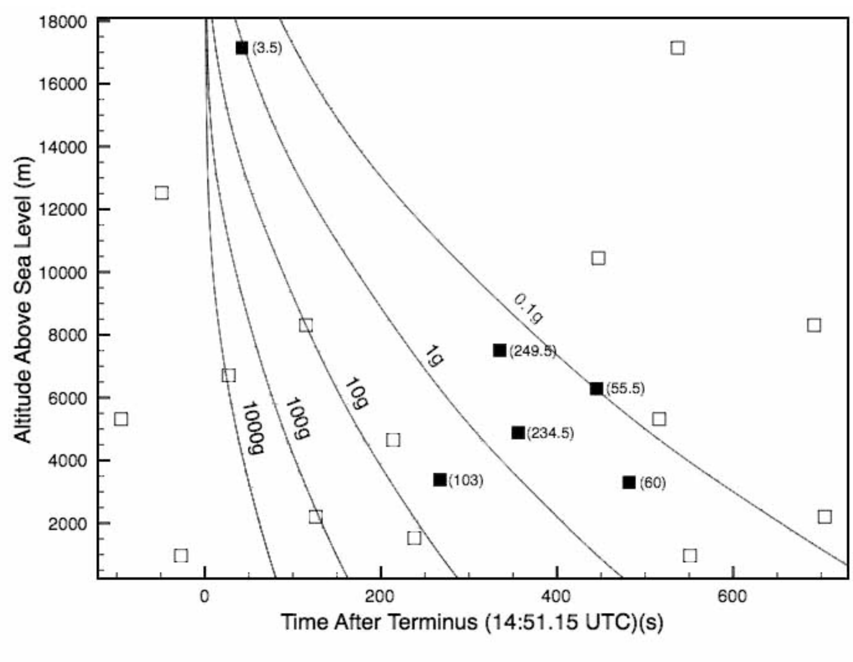

Fig. S6. Time-altitude relation for radar sweeps that did (solid square) and did not (open square) detect the falling meteorites. Solid lines are meteorite trajectories for different masses. The total of the absolute values of all radar reflectivity values bearing meteorite signatures are given in parentheses. Along a given mass trajectory, the higher that value is, the greater the number of meteorites in that radar sweep.

The radar returns originated predominantly from small 0.1 – 5 g fragments (Fig. S6), even in areas where larger meteorites were recovered. The presence of small meteorites among larger ones is confirmed by recovered meteorites (Table S3).

1.4. Recovered Samples

Figure S7 provides images of the various SM stones examined in this study. A complete list of known recovered SM stones found before June 26, 2012, is provided in Table S3.

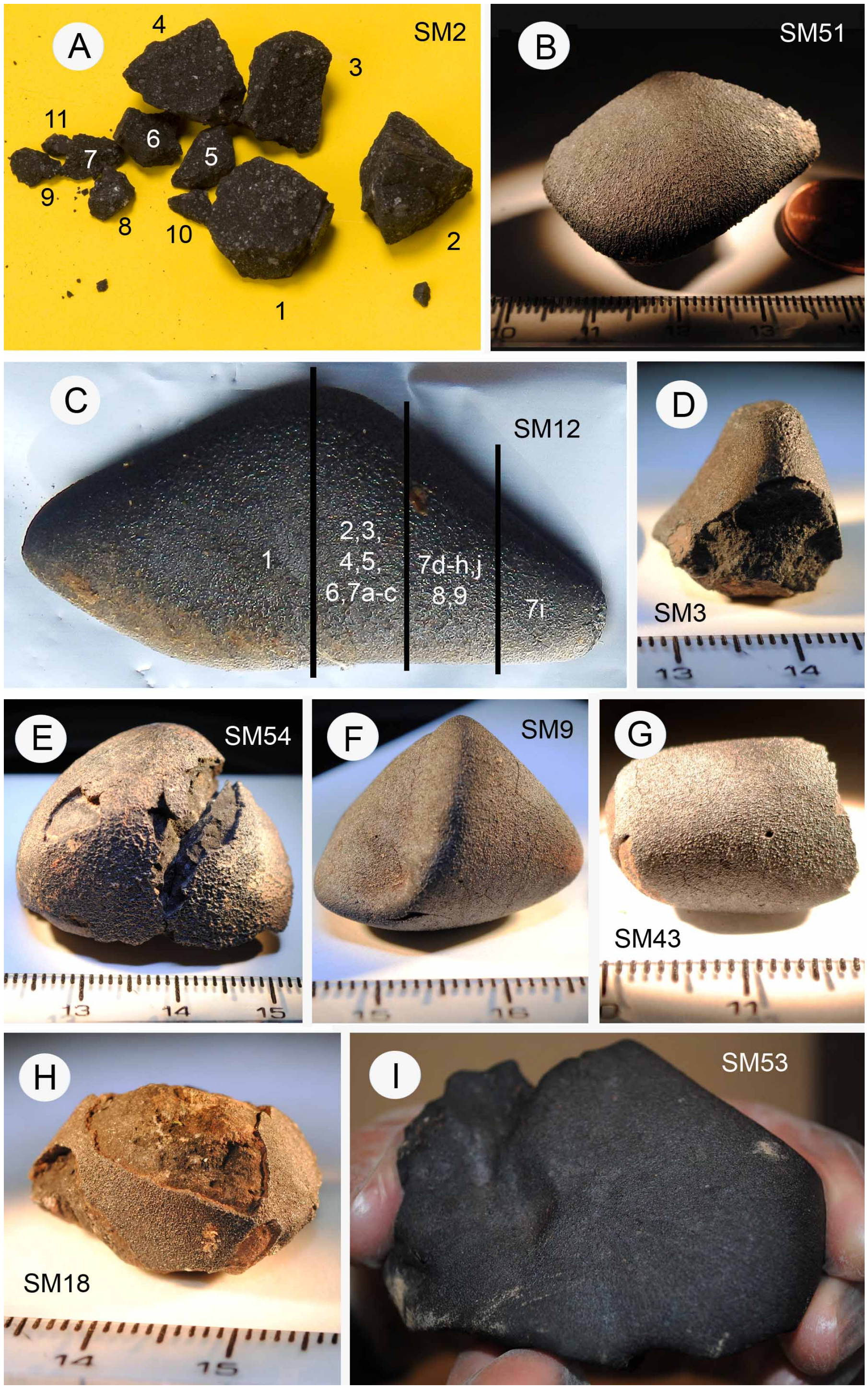

Fig. S7: **(A)** Fragments of Sutter's Mill SM2 with subsample identifications. **(B)** SM51, an oriented specimen. **(C)** SM12, with subsample identifications. **(D)** SM3, subject of X-ray computed tomography (CT) study. **(E)** SM54, subject of X-ray and neutron tomography. **(F)** SM9, subject of X-ray CT. **(G)** SM43, subject of chemical analyses and gamma-ray counting. **(H)** SM18, subject of gamma-ray counting and accelerator mass spectrometry analyses of ^{10}Be, ^{26}Al, and ^{36}Cl. **(I)** SM53 (the main mass thus far).

Table S3. Tally of reported finds prior to June 26, 2012. Meteorites marked with an asterisk (*) were examined for this study. Coordinates between brackets are approximate.

SM#	Mass (g)	Latitude (N)	Longitude (W)	Date find	Finder (Property owner)
1	5.6	38.8033	120.9075	4/24/2012	Robert Ward
2*	4.0	38.8029	120.9086	4/24/2012	Peter Jenniskens
3*	5.0	38.8103	120.9269	4/25/2012	Brien Cook
4	17.0	38.8040	120.9086	4/26/2012	Brenda Salveson
5	-.-	-.-	-.-	-.-	[not a meteorite]
6	2.4	38.8037	120.9049	4/26/2012	Patrick Murphy
7	6.0	38.8065	120.8879	4/27/2012	Jerry Moorman
8	19.0	38.8069	120.9358	4/27/2012	Susan Monroe
9*	6.3	38.8029	120.8928	4/27/2012	Eric Bowker
10	6.2	38.8053	120.9184	4/28/2012	Loraine Logan
11	14.5	38.8071	120.8925	4/28/2012	Tania McAlliser
12*	17.5	38.7857	120.9091	4/29/2012	Moni Waiblinger (Merv de Haas
13	18.9	38.7938	120.9217	4/29/2012	Marcos & Jennifer
14	11.5	38.8027	120.8945	5/1/2012	Suzanne Matin
15	11.3	38.8069	120.9358	4/27/2012	Mike & Julie Steward
16	15.0	38.8016	120.9078	4/30/2012	Jim & Bailey Plimpton
17	7.2	38.8003	120.8910	4/26/2012	Greg & Abriela Jorgensen
18*	5.4	38.8125	120.9056	5/2/2012	Greg Jorgensen
19*	10.0	38.8161	120.9375	5/3/2012	Alice Butler
20	1.1	38.8054	120.8955	4/27/2012	Richard Garcia
21	1.0	38.8014	120.8852	5/4/2012	Bob Pedersen
22	0.6	38.8024	120.8897	4/27/2012	Paul Gessler
23	1.6	38.8065	120.9102	4/27/2012	Vickie Ly
24	2.1	38.8145	120.9156	4/27/2012	Barbara Broide & Ryan Turner
25	7.3	38.8129	120.9246	4/27/2012	Jason Utas
26	3.5	38.8086	120.9041	4/30/2012	Jason Utas & Michelle Myers
27	35.1	(38.8058	120.9624)	5/5/2012	Mitch Carey
28	4.7	38.8059	120.8952	5/5/2012	Madeleine Hogue

29	11.8	-.-	-.-	5/1/2012	Joan Johnson
30*	3.5	38.7989	120.8810	5/1/2012	Joyce Matin & Mark Dayton
31	5.9	38.8132	120.9238	5/4/2012	Mark Dayton
32	9.6	38.8096	120.9263	5/1/2012	Doug Klotz
33	8.5	38.8071	120.8964	4/27/2012	Connie Nelson
34	1.6	38.7942	120.9814	5/3/2012	Adam Hamlin
35	0.1	38.7910	120.9781	5/1/2012	Robert Ward
36	22.6	(38.800	120.917)	4/27/2012	Mike Shaw
37	2.8	38.8142	120.9106	5/6/2012	Mike Miller
38	7.0	38.8142	120.9110	5/6/2012	Stanley Wall
39	2.5	38.8044	120.8941	4/27/2012	Mike Miller
40	17.7	38.8224	120.9598	5/5/2012	Keith Mueller
41*	9.3	38.8127	120.9077	5/4/2012	David Johnson
42	1.6	38.8146	120.9162	4/28/2012	Mendy Ouzillou
43*	4.3	38.8097	120.9283	4/29/2012	Sandy VanderPol & Emily
44*	5.5	38.7966	120.9196	5/9/2012	Dennis & Karen Kelleher
45	2.9	38.8047	120.9077	5/10/2012	Alex Wolfgram
46	2.4	38.8167	120.8638	5/4/2012	Rebecca Stuart-G.
47*	10.1	38.8078	120.8997	5/1/2012	Teal Triolo
48*	5.1	38.8147	120.8997	5/12/2012	Kelly Heavin
49	5.9	38.8116	120.9126	5/11/2012	Mike Miller
50	42.4	(38.8085	120.9603)	5/9/2012	Robert Ward
51*	12.3	38.8117	120.8957	5/2/2012	Rick Patrinellis
52	12.8	38.8150	120.9176	5/22/2012	Peter Utas
53	204.6	38.8136	120.9716	5/11/2012	Jeffrey Grant A.
54*	20.2	38.8054	120.9689	5/2/2012	Shane Skogberg
55	20.6	38.8086	120.9523	5/25/2012	Keith Jenkerson
56	7.6	38.8143	120.9217	5/11/2012	Bob Willis
57*	2.8	38.8212	120.8504	5/24/2012	Rick Nelson
58	1.3	38.8172	120.8550	5/26/2012	Sandy Cox
59	1.5	38.8328	120.8761	5/26/2012	Sandy Cox

60	4.5	38.8187	120.8795	5/26/2012	Rick Nelson
61*	3.4	38.8271	120.8691	5/26/2012	Rick Nelson
62	1.8	38.8151	120.8817	5/27/2012	Sandy Cox
63	8.3	(38.8061	120.9488)	5/26/2012	Dana Jenkerson
64	22.3	(38.8063	120.9483)	5/27/2012	Keith Jenkerson
65	11.6	38.8102	120.9163	5/30/2012	Philipe de Riemer
66	25.2	(38.8060	120.9500)	5/29/2012	Keith Jenkerson
67*	0.3	38.8082	120.9593	6/17/2012	Beverly Girten (Larry Spies)
68	1.0	38.8187	120.8744	6/8/2012	Connie Nelson
69	27.5	38.8034	120.9494	6/23/2012	Dan & Katrina Siders
70	27.0	38.8010	120.9619	6/30/2012	Glenn Arsenault
71	6.2	38.8123	120.9153	6/24/2012	Roy Karen
72	24.3	(38.8065	120.9461)	5/30/2012	Keith Jenkerson
73*	8.1	38.80785	120.91488	6/24/2012	Aidan & Noel Robinson
74	21.6	38.80784	120.95352	6/7/2012	Joel Kaderka
75	6.9	38.80920	120.90670	5/2/2012	Miquel Leon Contreras
76	8.1	38.80581	120.89448	4/27/2012	Sonny Clary
77	13.5	38.80611	120.96903	5/24/2012	several, incl. Jason Utas
78	14.5	38.80597	120.96894	5/26/2012	several, incl. Jason Utas

Notes: SM2, SM12, and SM67 were provided to the consortium, following donation by the property owners after being found by volunteers in the concerted volunteer searches organized by NASA Ames Research Center. Part of SM30 was donated by Joyce Matin. SM36, SM48, SM57 and SM61 were loaned for study by owners. SM18, SM43, SM51, and SM 73 were donated in part or acquired from local finders by the University of California at Davis. SM3 was loaned by Brien Cook. SM9 and SM54 were acquired by the American Museum of Natural History. SM41 was acquired by the Center for Meteorite Studies at Arizona State University. SM47 and part of SM1 were acquired by the Field Museum of Natural History.

2. Meteorite Characterization

2.1. Reflection Spectroscopy

Figure S8 combines the reflection spectra (*72*) measured at Brown University for SM12 over the 0.3 to 5 μm wavelength range. Results are compared to the available astronomical observations of asteroid 1999 JU_3 (*73*), the current Hayabusa 2 mission target. All data are normalized to 1 at 0.55 μm. The near-IR reflectance slope and the details in the 3-μm O-H stretch vibration band are found to vary as a function of the surface properties, comparing a naturally broken surface, a shaved surface, and the reflectance from a powder sample of shavings.

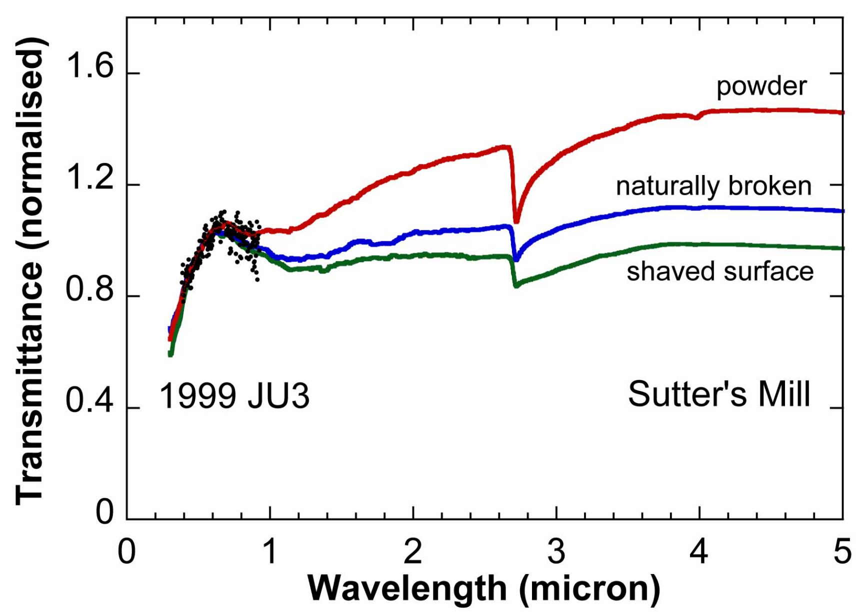

Fig. S8. Reflection spectra measured for SM12 over 0.3 to 5 μm range (solid lines), compared to astronomical observations of 1999 JU_3 shown as black dots (*73*).

Infrared transmission spectra of SM12 confirm the presence of phyllosilicates as evidenced by a characteristic Si-O stretching feature near 1000 cm^{-1}, a broad O-H stretching feature centered near 3400 cm^{-1}, and a narrow structural O-H band at 3680 cm^{-1}.

2.2. Magnetic Characterization

Pure magnetite, in a restricted sub-μm grain size range, is the main magnetic mineral in Sutter's Mill, but pyrrhotite ($(Fe,Ni)_{1-x}S$) contributes substantially to remanence. Sub-μm size magnetite was identified from hysteresis measurements on a Princeton Meas. Corp. Micromag operating in the Vibrating Sample Magnetometer mode (M_{rs}/M_s = 0.30, B_c and B_{cr} of 29 and 52 mT, S ratio of -0.97; with M_{rs} meaning saturation remanent magnetization, M_s saturation magnetization, B_c coercivity, B_{cr} coercivity of remanence, and S the ratio of remanence in a back field of 0.3 T over the remanence previously acquired in 3T), identification of Verwey transition at 118 K (Fig. S9, left), and determination of the maximum unblocking temperature of isothermal remanent magnetization (IRM) near 580°C (Fig. S9, right). Pyrrhotite (likely the hexagonal ferromagnetic form) is evidenced by the enhanced unblocking of saturation IRM (SIRM) below 300°C.

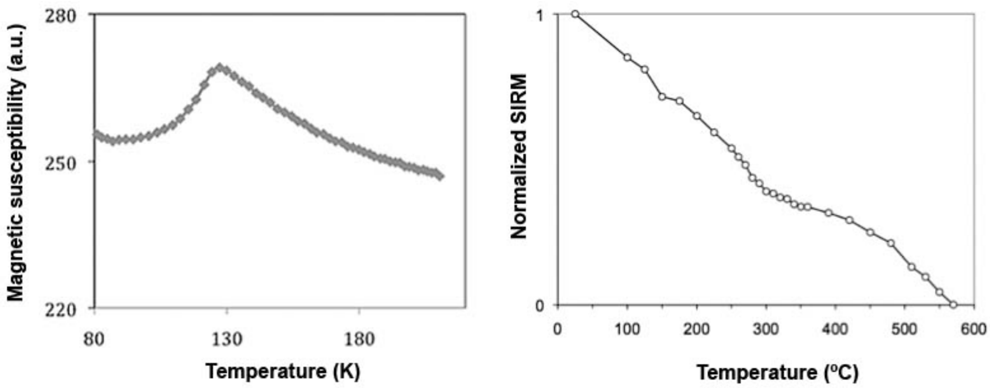

Fig. S9. Left: Magnetic susceptibility (arbitrary unit) of SM12 from liquid nitrogen to room temperature measured using the CSL low temperature cryostat attachment on an Agico Kappabridge MFK1 susceptibility measuring device in Aix-en-Provence. Right: Thermal demagnetization of the saturation isothermal remanent magnetization (SIRM) of a 2 mg fragment of SM12.

Of eight different Sutter's Mill stones measured for paleomagnetism using 2G Enterprises cryogenic magnetometers in Davis and Aix-en-Provence, only two (SM2 and SM73) preserved a low-intensity natural remanent magnetization (NRM) of presumably extraterrestrial origin. The others (SM12, 18, 51, 57, 61 and 67) showed intensities close to artificial saturation IRM, indicative of the application of a high magnetic field (> 100 mT), most likely by contact with rare earth magnets. Both SM2 and SM73 showed unidirectional behavior in the 20-60 mT range under alternating field (AF) demagnetization. SM2 (log χ = 4.26) had an NRM/ARM ratio in this AF range of about 35% whereas for SM73 (log χ = 4.19), this ratio was about 5%. Anhysteretic remanent magnetization (ARM) was acquired in a 100 mT AF field and a 50 μT DC bias field. As ARM/IRM is 0.3%, the corresponding NRM/IRM ratios are 1.0 and 0.2 ‰.

Table S4. Magnetic susceptibility measurements (χ in 10^{-9} m^3/kg) for the different stones, measured with a Bartington Magnetic Susceptibility Bridge in Davis (except for SM12 which was measured with the Agico MFK1 Kappabridge in Aix-en-Provence). The measurements separate into a magnetite-rich and a magnetite-poor group.

Sample	Mass (g)	log χ	s.d.	sample	Mass (g)	log χ	s.d.
high group				**low group**			
SM2	0.50	4.26	0.01	SM51	9.02	4.01	0.01
SM12	0.09	4.18	0.01	SM57	1.71	4.05	0.01
SM18	5.06	4.26	0.01	SM68	0.96	4.04	0.05
SM54-1	15.29	4.32	0.01	-.-	-.-	-.-	-.-
SM54-2	4.12	4.30	0.01	-.-	-.-	-.-	
SM61	1.84	4.27	0.01	-.-	-.-	-.-	
SM67	0.35	4.26	0.01	-.-	-.-	-.-	
SM73	8.17	4.19	0.01	-.-	-.-	-.-	
average		*4.26*	*±0.05*	*average*		*4.03*	*±0.02*

2.3. Petrography and Mineralogy

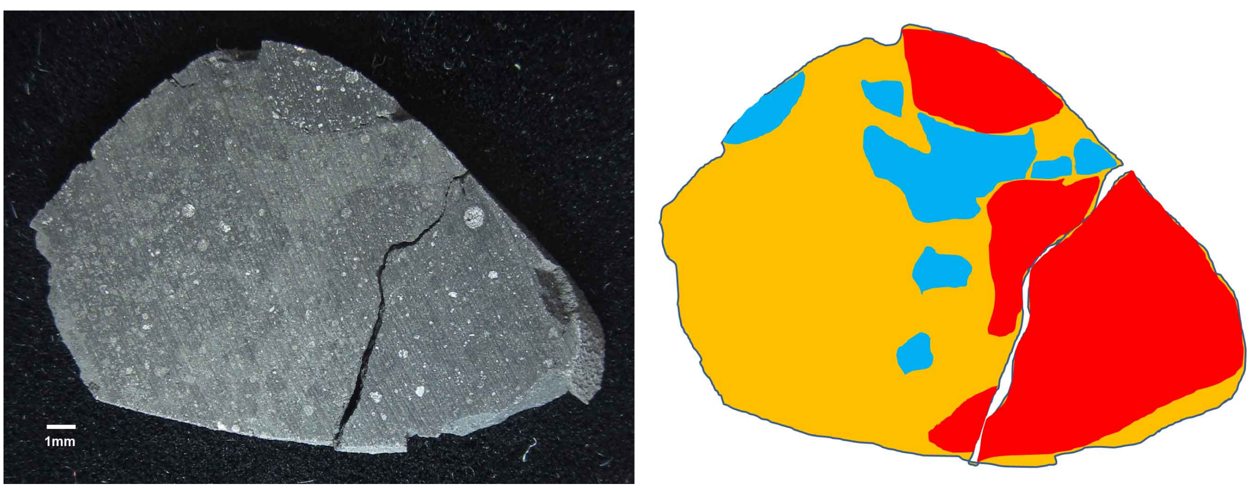

Fig. S10. Slice of SM48, showing both light (blue) and dark (red) clasts. Matrix is identified in orange.

In ordinary chondrite regolith breccias, the clasts are lighter than the matrix (Fig. 2, main text; Fig. S10, blue), where light clasts are normal material and the dark matrix consists of comminuted clasts that acquired solar wind gases, carbon, charged-particle tracks, and xenolithic material (*31*). Sutter's Mill also has clasts darker than the matrix (Fig. S10, red), which we infer to be pieces of mature matrix that have been lithified in the regolith, suggesting the asteroid surface underwent multiple phases of regolith recycling.

A polished thin section of SM51-1 (Figs. S11A,B) was mapped in Mg, Ca, Al, Si, Mn, S, Ni, Fe, P, Cr, and Na X-rays with a resolution of ~5 µm/pixel using the UH JEOL JXA-8500F field-emission electron microprobe and operating at 15 kV accelerating voltage, 50 nA beam current, and ~5 µm beam size. The Mg, Ca, and Al, and Fe, Mn, and Ca, and x-ray maps were combined using a RGB (red : green : blue) color scheme in Adobe Photoshop software. Objects of interest were subsequently studied in backscattered electrons using the JXA-8500F equipped with a energy dispersive spectrometer. Electron microprobe analyses (Tables S5 and S6) of silicates and phyllosilicates were performed with the JXA-8500F operated at 15 kV accelerating voltage, 15 nA beam current, and ~1 µm beam size using five wavelength spectrometers. Carbonates were measured at 15 kV accelerating voltage, 5 nA beam current, and ~2 µm beam size using five wavelength spectrometers. For each element, counting times on both peak and background were 30 sec. Minerals with known chemical compositions were used as standards. Matrix effects were corrected using PAP procedures (*74*).

Table S5. Representative electron microprobe analyses (in wt.%) of carbonates in Sutter's Mill, SM51-1.

mineral	CaO	MgO	FeO	MnO	SiO_2	CO_2	total
calcite	55.1	0.22	0.76	0.02	0.00	43.9	99.9
dolomite	32.1	16.8	2.8	1.6	0.25	46.5	100.0
dolomite	28.9	17.7	4.1	2.0	0.31	46.6	99.6
dolomite	28.5	16.6	5.0	3.2	0.17	46.2	99.6
dolomite	28.9	15.1	5.6	4.1	0.11	45.7	99.6
dolomite	27.8	14.8	5.4	5.7	0.68	45.6	100.1

Table S6. Electron microprobe analyses (in wt.%) of phyllosilicates in Sutter's Mill, SM51-1.

Location		SiO_2	TiO_2	Al_2O_3	Cr_2O_3	FeO	MnO	MgO	CaO	Na_2O	K_2O	total
chondrule phenocryst	avr (n=12)	38.7	0.07	2.5	0.65	15.2	0.18	26.1	0.11	0.37	0.06	84.0
pseudomorphs	*stdev*	*2.6*	*0.03*	*0.5*	*0.29*	*1.4*	*0.04*	*2.8*	*0.06*	*0.11*	*0.02*	*5.5*
chondrule mesostasis	avr (n=7)	32.7	0.15	4.7	0.64	30.9	0.24	20.1	0.04	0.58	0.05	90.1
pseudomorphs	*stdev*	*1.8*	*0.01*	*1.3*	*0.13*	*4.0*	*0.04*	*2.8*	*0.02*	*0.12*	*0.01*	*2.1*
matrix	avr (n=4)	40.0	0.12	2.5	0.45	14.8	0.22	28.6	0.05	0.28	0.04	87.1
	stdev	*0.5*	*0.04*	*0.1*	*0.04*	*0.4*	*0.03*	*0.9*	*0.05*	*0.03*	*0.01*	*0.9*
rims around carbonates	avr (n=15)	39.6	0.09	2.5	0.39	14.7	0.22	26.9	0.69	0.30	0.05	85.4
grains	*stdev*	*1.0*	*0.03*	*0.1*	*0.05*	*2.1*	*0.02*	*1.1*	*1.0*	*0.06*	*0.01*	*2.4*

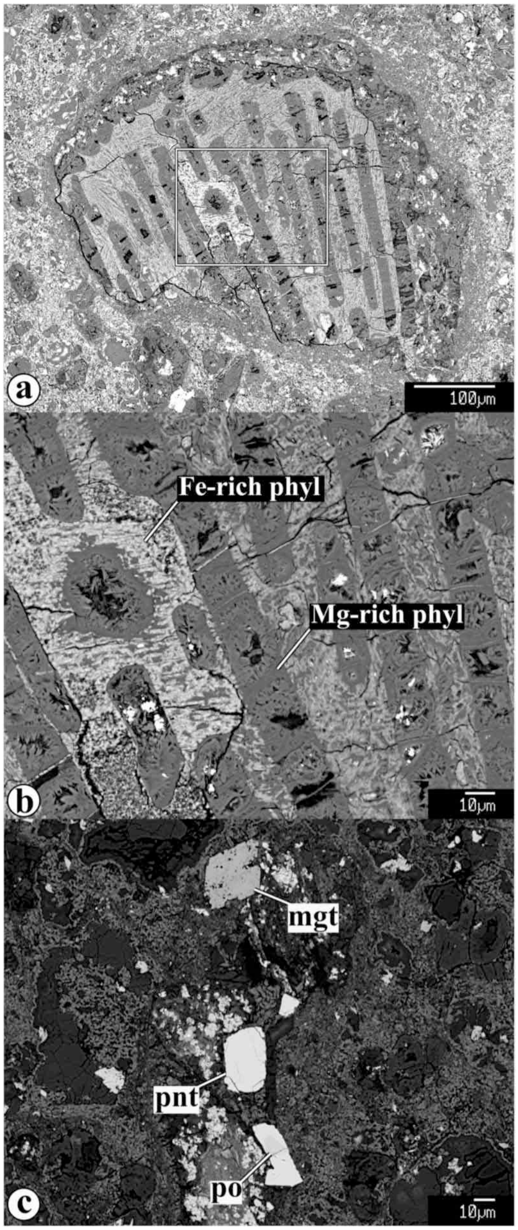

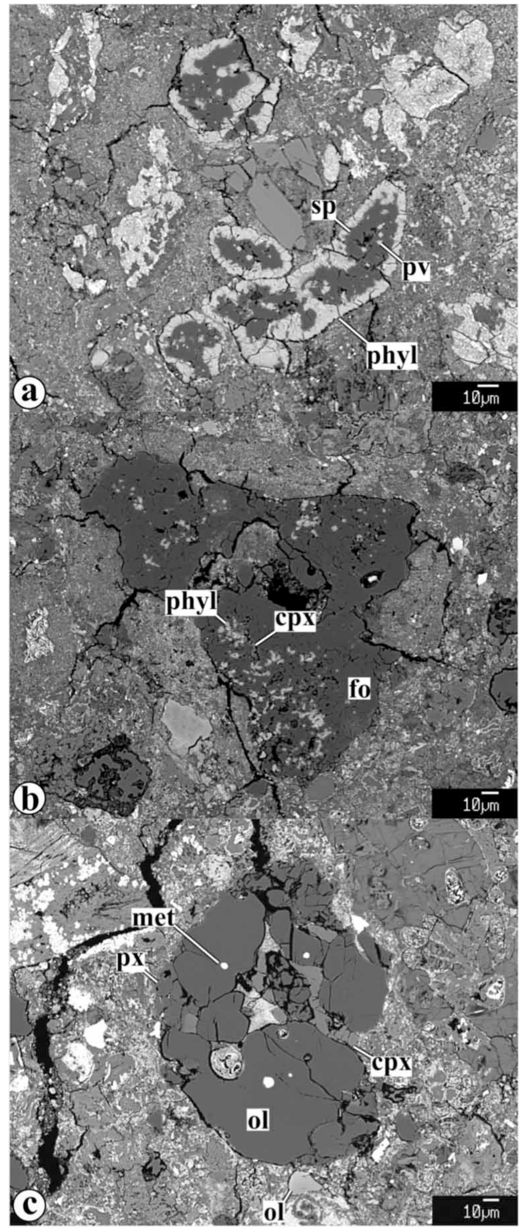

Fig. S11A. Backscattered electron images of **(A, B)** barred olivine chondrule replaced by ferroan and magnesian phyllosilicates (phyl), and **(C)** pyrrhotite (po), pentlandite (pnt), and magnetite (mgt) in matrix of Sutter's Mill, SM51-1.

Fig. S11B. Backscattered electron images of incompletely aqueously altered **(A)** calcium-aluminum-rich inclusion, **(B)** amoeboid olivine aggregate **(C)**, and **(D)** magnesian porphyritic chondrule in the CM2.1 lithology of Sutter's Mill, SM51-1. cpx = high-Ca pyroxene; fo = forsterite; phyl = phyllosilicates; ol = ferromagnesian olivine; pv = perovskite; px = low-Ca pyroxene; sp = spinel.

Subsample SM51-1, consists of two distinct CM2 lithologies, CM2.0 and CM2.1, with a sharp boundary between them (Fig. 2b, main text). The CM2.0 lithology contains completely hydrated pseudomorphs after chondrules and refractory inclusions. In addition, the CM2.1 lithology contains rare relict grains (mostly olivine) of incompletely altered type I ($Fa_{0.5\text{-}2}$) and type II ($Fa_{27\text{-}46}$) chondrules, amoeboid olivine aggregates (AOA), and CAIs. Both lithologies contain coarse dolomite ((Ca,Mg,Fe,Mn)CO_3) and calcite ($CaCO_3$), and hydrated matrix.

Calcite grains are compositionally uniform (Fig. S12) and contain 0.7−1.5 wt.% FeO and <0.6 wt.% MnO and MgO; dolomite grains are often chemically-zoned and contain 2.6−6.7 wt.% FeO and 1.5−5.7 wt.% MnO. Phyllosilicates are close to serpentine solid solution.

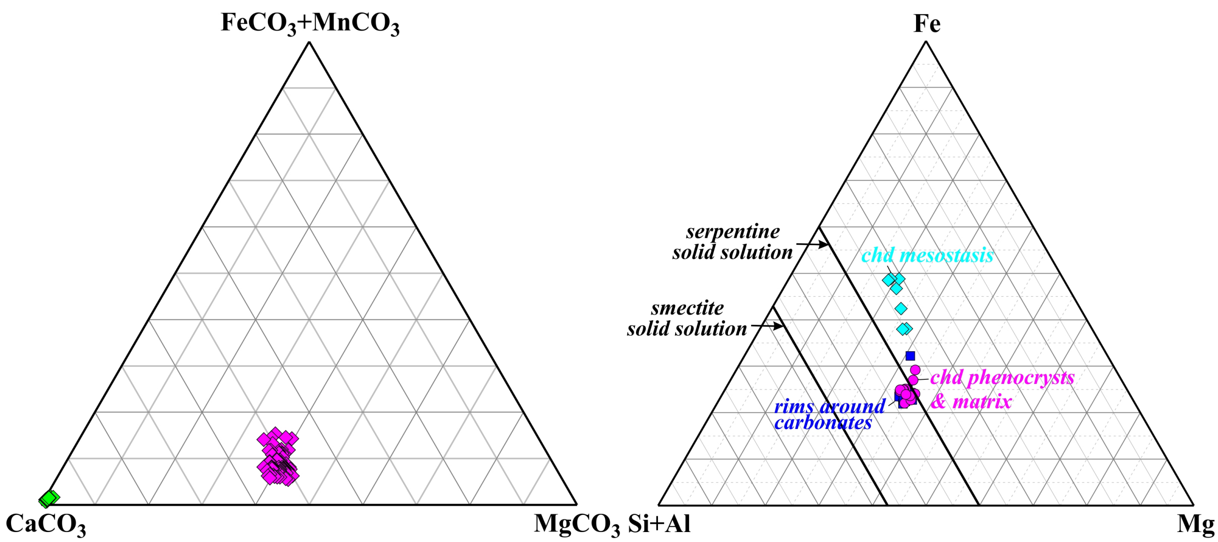

Fig. S12. Chemical compositions of calcite (cal) and dolomite (dol) in Sutter's Mill, SM51-1.

For sample SM47, we collected high-resolution backscattered electron (~1 μm/pixel) and elemental X-ray (~4 μm/pixel) maps (C, O, Mg, Al, Si, S, Ca, Ti, Cr, Fe, Ni) in order to identify the petrologic components of the meteorite. A 6.9×4.6 mm polished section of Sutter's Mill (SM47-1; Field Museum specimen number Me 5799) was analyzed with the University of Chicago JEOL JSM-5800LV scanning electron microscope equipped with an Oxford/Link ISIS-300 X-ray microanalysis system. The specimen was embedded in Buehler UHV-compatible epoxy and polished with diamond lapping film with high purity isopropanol with a nominal water concentration of <0.05% (in order to minimize loss of water soluble minerals).

Fig. S13A. Backscattered electron (BSE) mosaic map of SM47.

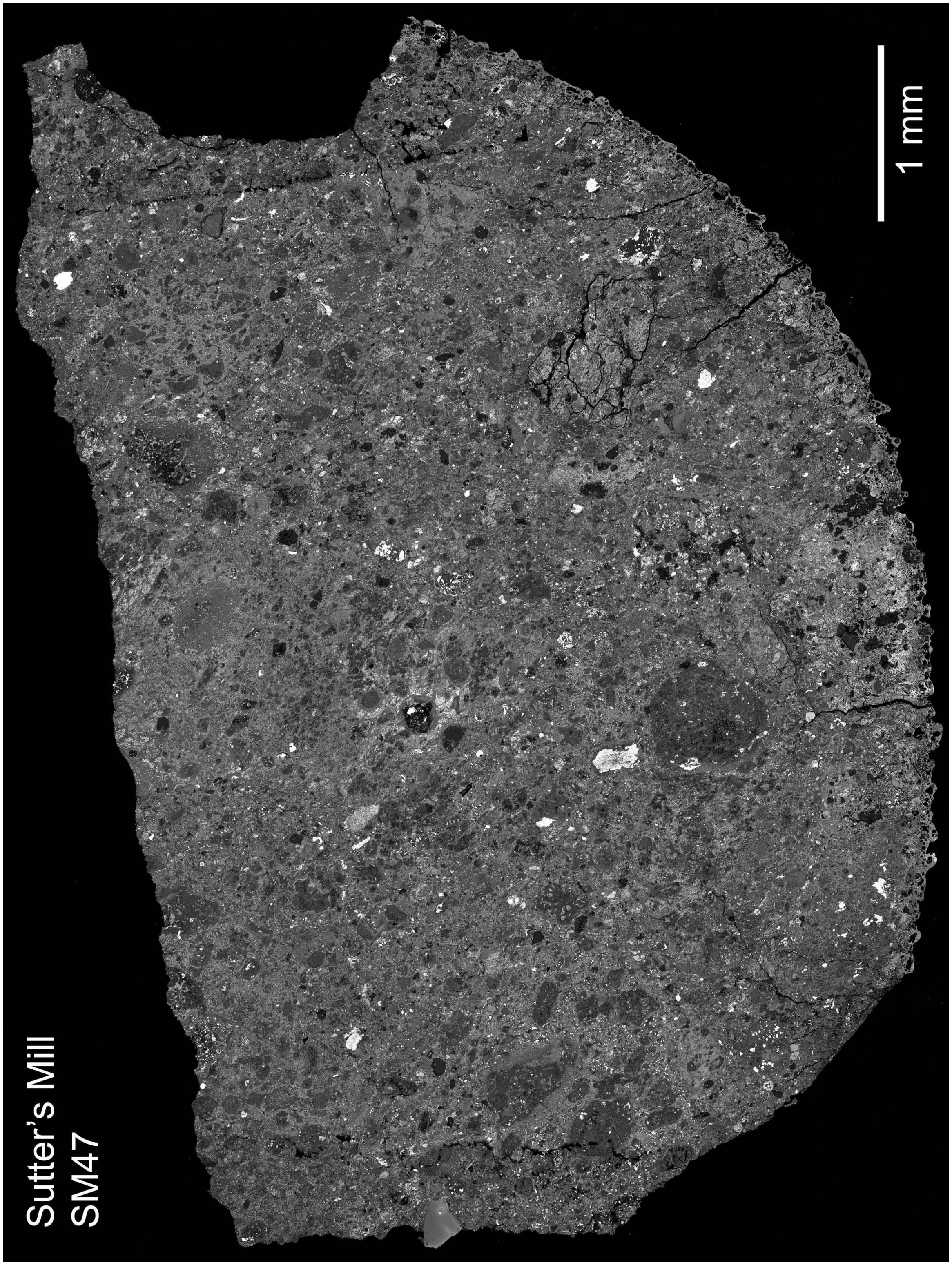

Fig. S13B. Elemental X-ray maps of polished section SM47. The first image combines Magnesium (Mg, red), Calcium (Ca, green), and Aluminum (Al, blue), the second Iron (Fe, red), Nickel (Ni, green), and Sulfur (S, blue). Subsequent maps show individual elements.

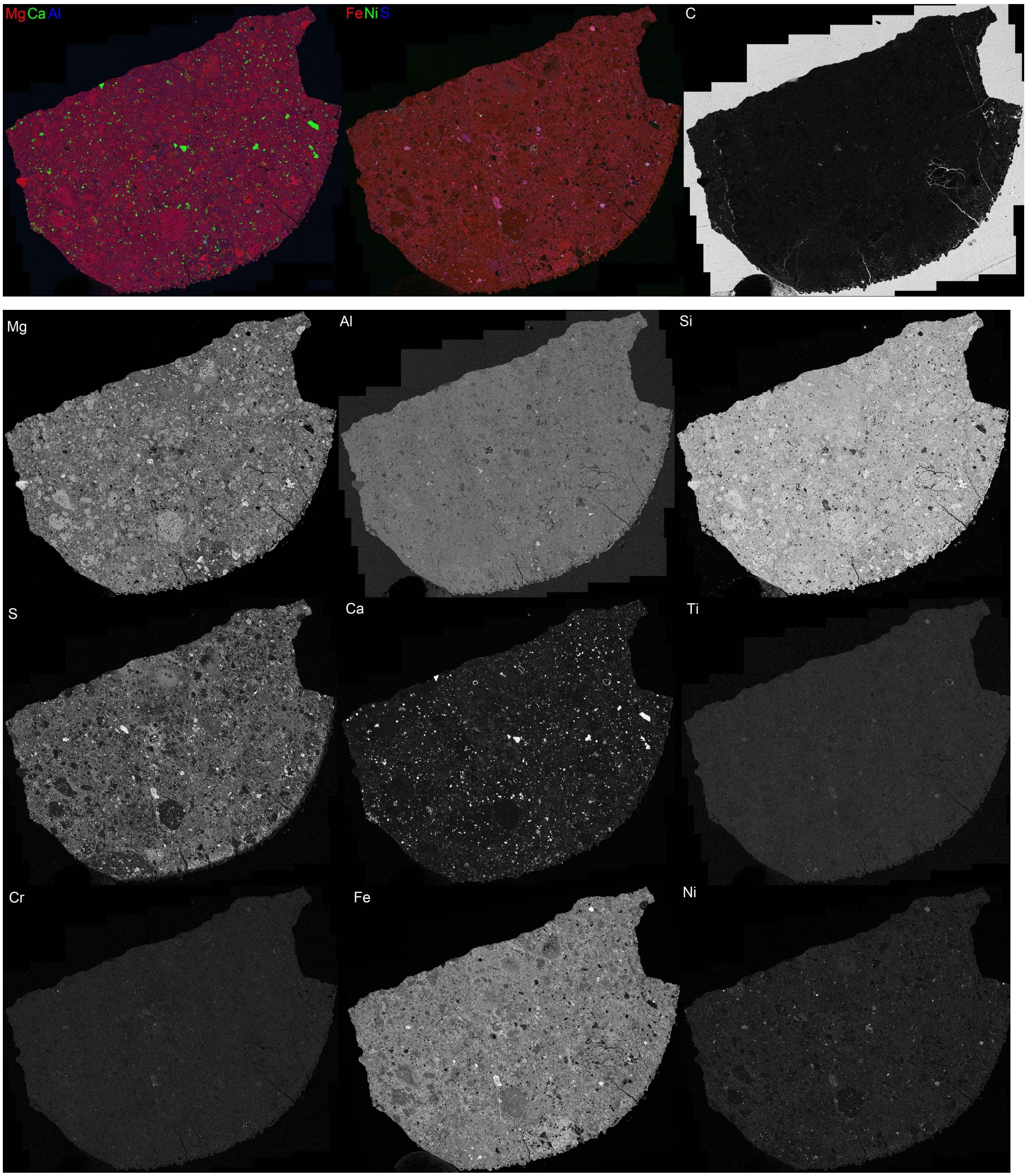

Unprocessed images from the Oxford ISIS software were stitched together using the Grid/Collection Stitching plug-in within the freely available Fiji image-processing program. Fiji automatically stitched and blended the Mg map. The coordinates of each panel within the Mg photomontage were used to construct all the other element photomontages, so all the element maps are correctly registered relative to one another.

In SM47-1, unlike in other sections, no carbonate or sulfide veins are observed, but grains of sulfides and angular calcite are abundant. Single grains of olivine, some of them strongly zoned ($Fa_{14–63}$), pyroxene, troilite and pentlandite are abundant, but chondrules are sparse and are heavily altered (Fig. S13A). Mesostases in three chondrules examined thus far have been converted to Fe-rich phyllosilicate, and this material encloses olivine pseudomorphs – an FeO-, Al_2O_3-, S-bearing material (or intergrowth) that has preserved the shapes of the olivine grains. In contrast, isolated grains of fresh, nearly FeO-free olivine, pyroxene, and spinel can be found in the matrix. Refractory inclusions are sparse and small. We found seven small CAIs that are rich in Mg-Al spinel with minor perovskite±Fe-silicate. They are typically rounded and 20 - 30 μm across, with outer rims of Fe-silicate. Two have lost their cores, possibly during section preparation, and are hollow shells of spinel. Spinel grains are typically ~5 μm across, and perovskite is ~1 μm. An isolated fragment of hibonite ~6 μm across, with ~1.6 wt.% TiO_2, is also present in the section (Fig. S13B).

Synchrotron X-ray Diffraction (S-XRD)

We collected Laue patterns of selected matrix and CaS grains from sample SM2-5 (Fig. S7) by the Laue synchrotron X-ray diffraction (S-XRD) using the intense X-ray source of SPring-8 in Japan. At SPring-8 beam line 37XU an undulator is installed and its radiation is further monochromatized using a Si (111) double-crystal monochromator. The X-ray energy is automatically adjusted by changing the undulator gap and the angle of a monochromator.

Diffraction patterns are collected on the two-dimensional detector (CMOS Flat panel detector, Hamamatsu Photonics K.K.). The samples are attached to a XYZ-stage, and the target micro area in the sample was adjusted on the micro-beam position under an optical microscope. We applied energies from 30.00 to 20.00 keV (λ = 0.4133–0.6199 Å) at increments of 40 eV with each exposure time being 0.5 seconds.

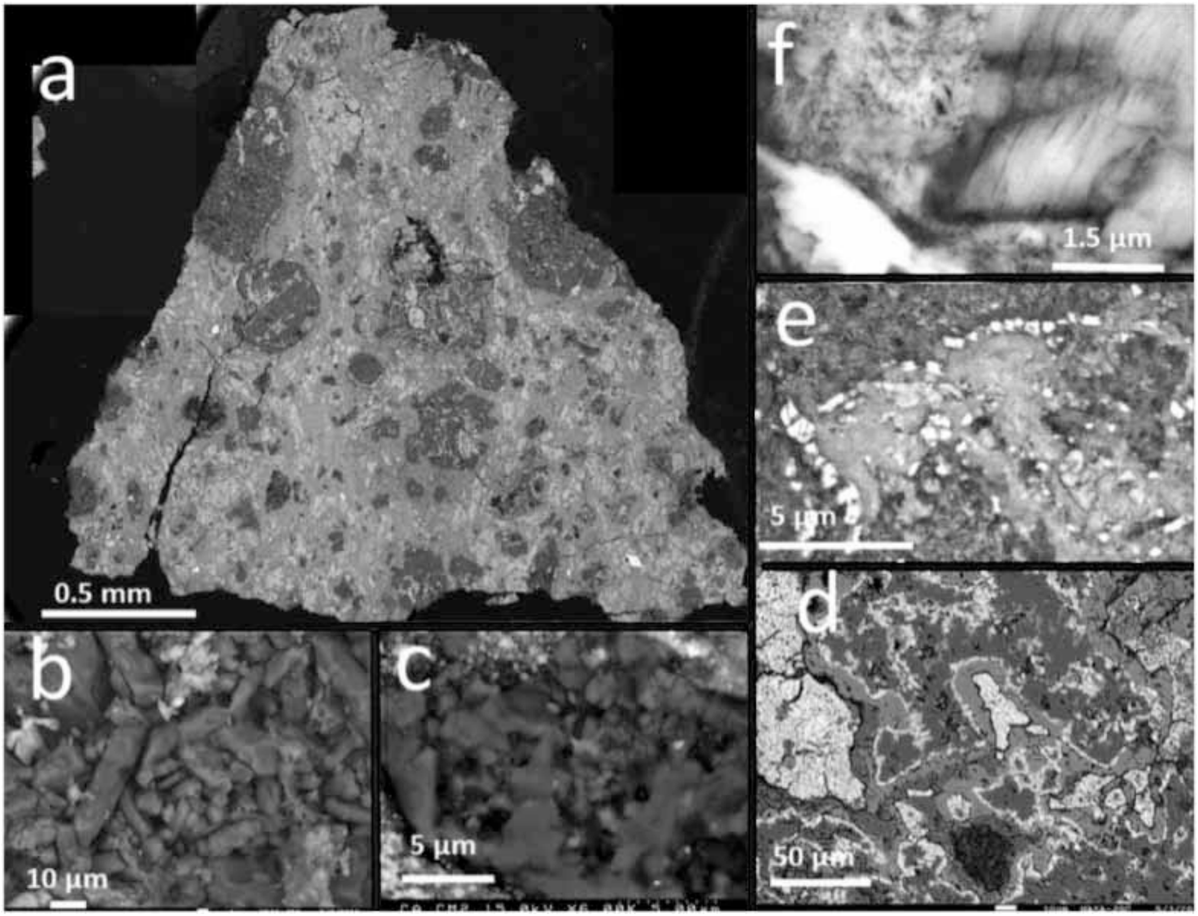

Fig. S14. Electron backscattered (BSE) images of the thermally metamorphosed CM lithology in sample SM2. **A)** A mosaic of an entire section. **B)** An aggregate consisting of platy enstatite crystals. **C)** An extremely embayed forsterite grain. **D)** A layered CAI, which is typical of CM chondrites. **E)** Lithic fragment with a rim of troilite crystals. **F)** a flaky matrix grain which is a pseudomorph of olivine after serpentine.

The instrument parameters were calculated from the coordinates on the Debye-Scherrer rings in the diffraction pattern of Si powder (NIST 640c) taken at 30 keV and the values were used for further analysis. Normally a Laue pattern records diffraction from a single crystal. However, in these instances the samples proved to be polycrystalline to a very fine scale, and so powder patterns were collected. Two patterns of SM2 matrix from the lithology that resembles CM2 chondrites (Fig. S14A) could be successfully indexed as olivine. This was despite the fact that the morphology of these samples was identical to the flaky serpentine characteristic of CM2 chondrites.

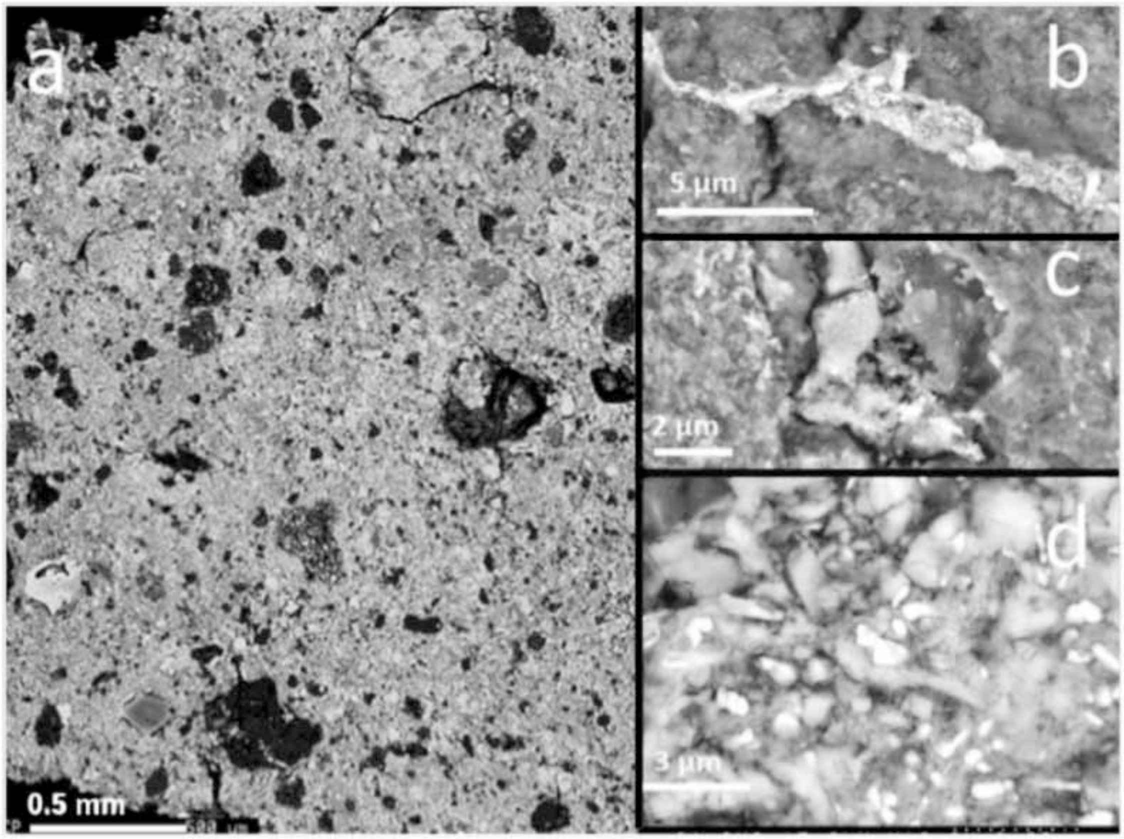

Fig. S15. Electron backscattered (BSE) images of the finely comminuted lithology in sample SM2, which contains minerals typical of reduced meteorites. **A)** A mosaic of an entire section. **B)** A vein of platy Fe-Ni-Ti phosphides and sulfides. **C)** An embayed grain of oldhamite (CaS) shaped like the letter "L". **D)** Troilite (medium grey) contains fine disseminated phosphide crystals.

We conclude that this particular sample has been heated to at least 500°C, the minimum temperature necessary to convert serpentine and cronstedtite to olivine (*30*). This temperature is also sufficient to convert tochilinite to troilite, which we observe in abundance in matrix and rimming chondrules and matrix components (Fig. S14), where one would normally observe tochilinite. A powder Laue pattern of the CaS from the fine-grained SM2 lithology (Fig. S15) proved to index uniquely as oldhamite (Fig. S16).

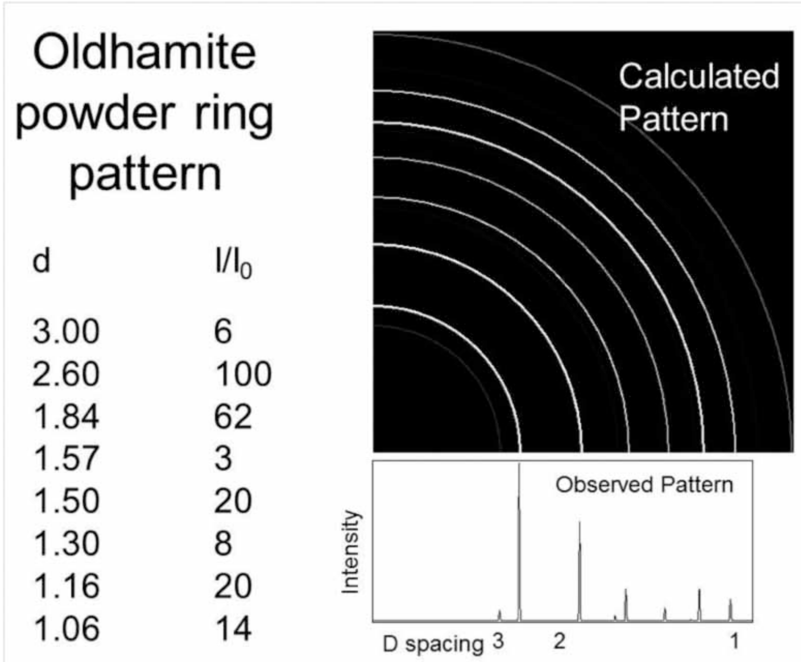

Fig. S16. Laue XRD pattern of the sample SM2 oldhamite, compare to a calculated oldhamite XRD pattern.

2.4. Major, Minor, and Trace Element Analyses

X-ray fluorescence (XRF)

The whole-rock sample SM51 was analyzed for element concentrations using a Bruker S8 WD-XRF at Lawrence Livermore National Laboratory. Analyses were performed on two flat cut surfaces of the sample using the Bruker QuantExpress analytical program. The instrument calibration was performed by measuring standard silicate glass discs (Breitländer GmbH), certified for a suite of major and trace elements, under the same operating conditions as the samples. All elements from sodium to uranium were analyzed, but only elements measured above detection limits are reported in Table S7. Detection limits were typically on the order of 50−200 ppm. Typical analytical sum totals were 92−95%; results were normalized to 100%, after including 2.5% percent concentration of carbon (see Tables S7, S13, S24 and section 2.9). Iron is reported as Fe^{2+}.

Synchotron-induced X-ray Fluorescence (S-XRF)

Sutter's Mill sample SM51 and a portion of the Murchison (CM) meteorite were analyzed by synchrotron-induced X-ray fluorescence (S-XRF) (*75,76*) at the UC Davis DELTA Group X-ray milliprobe at beam line 2.2 of the Stanford Synchrotron Radiation Lightsource, Stanford Linear Accelerator Center. Each sample had been cut to expose a flat surface which was exposed to a 3×2 mm^2 beam of monochromatic 38 keV polarized X-rays. Repeated measurements were first made to establish precision, and then the beam was moved in mm steps, totaling 9 measurements for SM51 and 4 for the Murchison fragment. Mean precision for all measurements was ±8% for SM51, ±4% for Murchison. Data were collected by a high count rate VORTEX Si(Li) X-ray detector using 2040–20 eV steps on the 40 keV scale and were reduced using the program WinAXIL. The spectra were examined for elements from silicon to barium, and then tantalum through bismuth, 52 elements in all, eliminating noble gases and radioactive elements other than thorium and uranium. The published data on the Murchison meteorite (*cf. 43*) were used to establish the yield and self-absorption corrections, which were then applied to the SM51 data to obtain mass fraction data in % or ppm. This was made possible by the very close compositional agreement between the two fragments.

The results for major, minor and trace element compositions of the Sutter's Mill meteorite are summarized below in Table S7; data lacking statistical significance are excluded.

Notes to Table S7:

[#] Concentrations of carbon and nitrogen are measured separately by different technique (see details below in Sections 2.9 and 2.16 and Tables S13, S14, S22);

** Concentration of sulfur is measured separately (see details in section 2.5 on Sulfur).*

Table S7. Major, minor and trace element compositions of the Sutter's Mill meteorite.

Element	Units	S-XRF (SLAC) SM51	XRF (LLNL) SM51	ICP-MS				ID-TIMS /ICP-MS	
				UC Davis (HR ICP-MS)		Fordham (Q-ICP-MS)		UMd	
				Average (SM51)	(n)	Average (SM2)	(n)	Average (SM51)	(n)
H									
He				See Table S15					
Li	ppm			1.66	4	1.70	2		
Be	ppm			0.044	6				
B	ppm								
C	wt.%			2.5 #					
N	ppm			559 #					
O									
F									
Ne				See Table S15					
Na	wt.%		0.47	0.57	4				
Mg	wt.%		13.79	12.67	4				
Al	wt.%		1.34	1.27	4				
Si	wt.%	13.45	13.72						
P	wt.%	0.11	0.13						
S	wt.%	3.14	2.77	3.16*	3				
Cl	ppm	674	700						
Ar				See Table S16					
K	ppm	363							
Ca	wt.%	1.44	2.11	1.41 - 1.82	4				
Sc	ppm			9.23	10	8.39	2		
Ti	wt.%	0.056	0.07	0.07	4	0.07	2		
V	ppm	81		77.15	4	74.00	2		
Cr	wt.%	0.32	0.34	0.31	4				
Mn	wt.%	0.17	0.19	0.18	4	0.19	2		
Fe	wt.%	22.2	22.78	22.37	4				
Co	ppm	585	450	560.90	4	590.00	2		
Ni	wt.%	1.28	1.29	1.24	4				
Cu	ppm	135	200	152.70	10	159.00	2		
Zn	ppm	187	250	212.40	10				
Ga	ppm			9.53	6	9.30	2		
Ge	ppm	37.5		33.40	2				
As	ppm					1.70	2		
Se	ppm	15.2				13.00	2		
Br		1.9							
Kr				See Table S16					
Rb	ppm			1.85	4	2.60	2		
Sr	ppm	10.6		10.82	4	9.40	2		
Y	ppm	2.1		2.42	4	2.60	2		

Table S7 (cont.). Major, minor and trace element compositions of Sutter' Mill meteorites

Zr	ppm	7.6			4	7.90	2		
Nb	ppm			0.494	4	0.480	2		
Mo	ppm							1.107	
Ru	ppm	0.93						0.886	2
Rh	ppm	0.17							
Pd	ppm	0.66		0.860	2	0.650	2	0.652	2
Ag	ppm	0.15							
In	ppm	0.05		0.063	4				
Sn	ppm			1.35	4	0.990	2		
Sb	ppm	0.14		0.120	2	0.170	2		
Te	ppm	1.5		1.42	2	1.55	2		
I	ppm	0.26							
Xe				See Table S17					
Cs	ppm	0.13		0.14	4	0.216	2		
Ba	ppm			3.28	4	3.28	2		
La	ppm			0.373	6	0.408	2		
Ce	ppm			0.859	4	1.05	2		
Pr	ppm			0.129	4	0.156	2		
Nd	ppm			0.677	4	0.714	2		
Sm	ppm			0.223	4	0.237	2		
Eu	ppm			0.071	10	0.084	2		
Gd	ppm			0.172	4	0.314	2		
Tb	ppm			0.045	10	0.061	2		
Dy	ppm			0.410	10	0.318	2		
Ho	ppm			0.083	4	0.080	2		
Er	ppm			0.230	4	0.241	2		
Tm	ppm			0.041	4	0.042	2		
Yb	ppm			0.249	4	0.237	2		
Lu	ppm			0.040	8	0.043	2		
Hf	ppm			0.143	4	0.180	2		
Ta	ppm	0.02		0.021	4				
W	ppm			0.129	4	0.120	2		
Re	ppm					0.054	2	0.0524	2
Os	ppm							0.607	2
Ir	ppm			0.650	2	0.670	2	0.592	2
Pt	ppm			1.30	2	0.915	2	1.142	2
Au	ppm	0.15							
Hg	ppm								
Tl	ppm	0.09		0.096	6				
Pb	ppm	1.88		1.61	4				
Bi	ppm			0.069	4				
Th	ppm			0.047	4	0.050	2		
U	ppm			0.013	4	0.013	2		

HR-ICP-MS and Q-ICP-MS

For wet chemical analyses by ICP-MS techniques, about ~0.4 g and ~1.1 g sample fragments were obtained from SM43 and SM51 respectively. Fusion crusts were carefully removed, ca. ~0.15 g and ~0.46 g of fresh fragments were further crushed to obtain homogeneous sample powders for elemental and isotopic measurements.

About 30 mg aliquots from whole rock powders were dissolved in a concentrated HF-HNO_3 mixture, and heated in the oven using stainless steel bombs at 190°C for >60 hours. Approximately 2% (0.5 mg) of each sample was used for major, minor and trace element abundance measurements, respectively, using the *Element XR* HR-ICP-MS at University of California at Davis, which offers the possibility to run some elements at higher resolution to avoid potential isobaric interferences. Concentrations were calculated by calibrating to a series of known rock standards. Limits of detection (3σ standard deviation of background) vary depending on the element in question; REE's were in the ppq (10^{-15}) level while higher blank elements such as Na, B, Ni, Cu, Zn, Mg, and Ca were ~0.1–0.5 ppb. Accuracy was assessed by running a number of known meteorite samples Murchison (CM2), Allende (CV3), Tagish Lake (ungrouped), Orgueil (CI1), and Lancé (CO3), and comparing our data with published values.

In addition, we used the methods outlined in (*29*) with a Thermo X Series II ICPMS at Fordham University, to quantify 45 trace elements by ICPMS. A 30 mg chip of SM2, free of fusion crust, was split in two, yielding nearly identical results. The results are summarized in Table S7.

2.5. Sulfur

Sulfur concentrations were measured separately by high resolution inductively coupled plasma mass spectrometer at Rice University. Three aliquots of 2 mg each (SM51), weighed to a precision of 0.1% were dissolved in aqua regia for 24 h at 150°C. Resulting solutions were centrifuged and then diluted into 2 wt.% HNO_3, which was then introduced into the mass spectrometer using a 100 microliter Teflon nebulizer coupled to a cyclonic spray chamber. Isobaric interferences were resolved under medium mass resolution mode (3000). Three isotopes were measured (^{32}S, ^{33}S, ^{34}S). Signals were converted to concentrations using two independent gravimetric standards made from pure anhydrite. Accuracy of gravimetric standards is <1%. External standards ranging from 0.1 ppb to 100 ppm in solution were determined in order to bracket sample unknowns. Elemental concentrations determined from ^{32}S, ^{33}S, and ^{34}S agreed to within 1%. External reproducibility was <1%. For meteorite samples, procedural blanks and memory on the ICP-MS were negligible.

2.6. Highly Siderophile Element Concentrations (Re and Platinum Group Elements) and Os Isotopes

Two aliquots of approximately 50 mg each of the meteorite powders (SM51-A and SM51-B), originally prepared from ~0.5 fresh interior piece of SM51, were analyzed at the UMd for highly siderophile element concentrations (HSE: Re, Os, Ir, Pt, Ru, Pd) and $^{187}Os/^{188}Os$ isotopic composition using standard high temperature acid digestion, chemical purification and mass spectrometry techniques (27, *77*). The results are listed in Table S8.

Table S8: Highly siderophile element concentrations and Re-Os isotope systematics.

	Re (ppb)	Os (ppb)	Ir (ppb)	Ru (ppb)	Pt (ppb)	Pd (ppb)	$^{187}Os/^{188}Os$	2σ	$^{187}Re/^{188}Os$	2σ	$^{187}Os/^{188}Os$ initial	Model Age (Ga)
SM 51-A	53.49	600.7	591.0	884.2	1140	651.2	0.12602	0.0001	0.4289	0.0005	0.0921	4.14
SM 51-B	51.31	613.5	593.4	887.0	1143	653.0	0.12613	0.0001	0.4028	0.0005	0.0943	4.41

The Os isotopic compositions of the two aliquots are identical within uncertainties of ±0.1% (Table S8), and the average ratio of 0.1261 is well within the range of other carbonaceous chondrites (Fig. S17). Fig. S18 shows CI (Orgueil)-normalized HSE element abundance patterns for Sutter's Mill (SM51), compared with data for three other CM chondrites. For the two pieces, most HSE concentrations are in agreement within 0.4% of one another, consistent with homogeneity of the finely ground powders. In contrast, Re and Os concentrations differ by 4 and 2%, respectively. These variations are well above the 0.1% analytical reproducibility of these elements for standards, and indicate moderate heterogeneity between the two powder aliquots. Further, the resulting calculated $^{187}Re/^{188}Os$ ratios differ by 6%, and initial $^{187}Os/^{188}Os$ ratios calculated for 4.567 Gy are 0.09211 (SM51-A) and 0.09427 (SM51-B). These calculated initial ratios are significantly lower than current estimates for the initial Solar System $^{187}Os/^{188}Os$ ratio at the time of its formation (0.0953). The differences can't be attributed to nucleosynthetic anomalies in bulk chondrites, as Os isotopic variations are unknown for bulk chondrites, even on a much smaller scale. In addition, there is no evidence of nucleosynthetic anomalies of a similar magnitude for neighboring elements in the bulk meteorite.

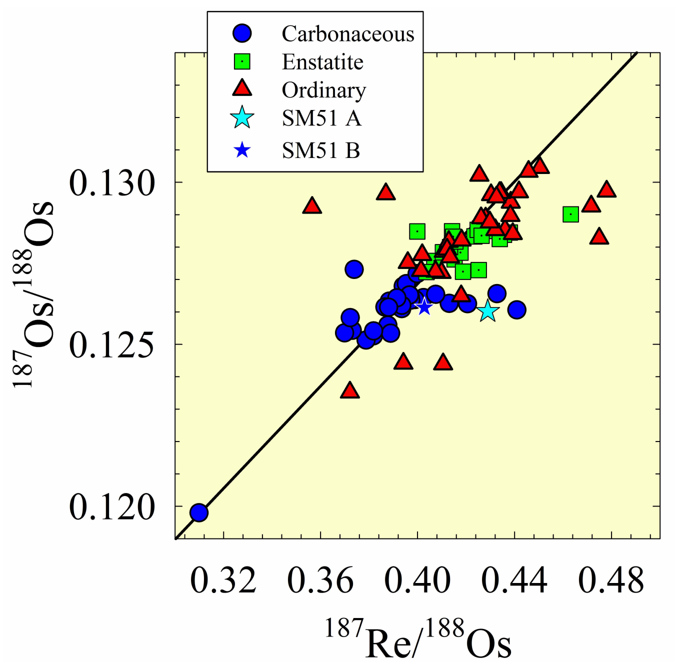

Fig. S17. ^{187}Re-^{188}Os versus ^{187}Os/^{188}Os plot showing the data for the two pieces of Sutter's Mill examined here, compared with data for other carbonaceous, ordinary and enstatite chondrite group. Chondrite data are from (*78*). The offsets of the Sutter's Mill data from the 4.57 Gy reference isochron is observed in numerous other chondritic meteorites.

Thus, given the virtually identical Os isotopic compositions in the two aliquots, the differences in Re and Os concentrations, and especially the ^{187}Re/^{188}Os ratio, must reflect mobility of Re, and to a lesser degree of Os, as a consequence of some post-formation, open-system behavior of these two elements. Model ages of 4.14 Gy (aliquot A) and 4.41 Gy (aliquot B) can be interpreted as reflecting resetting events within the first several hundred million years following formation, as may result from impact related shock. However, these ages are substantially younger than the aqueous alteration ages of ~4.563 Gy, defined by the ^{53}Mn-^{53}Cr ages of calcite and dolomite present in CM chondrites, e.g. (*79,80*). If the differences are the result of shock during the early stage of solar system evolution, the disparity between the two ages requires the open-system behavior to have occurred on a sufficiently small scale, such that powdering the meteorite did not homogenize the isotopic systematics. This seems unlikely.

Alternately, the analytically indistinguishable Os isotopic compositions of the two pieces permit an interpretation of recent, open-system behavior. This could have occurred as a result of the impact event that liberated the meteorite from its parent body. It is even possible that the single rain event on April 25, experienced by the piece of meteorite from which the powders were prepared, resulted in the re-distribution of Re within the meteorite, leading to the open-system behavior. Evaluation of pristine and variably altered samples will be required to assess this possibility. Fig. S-17 illustrates that many chondrites are characterized by open-system Re-Os isotopic systematics to a similar degree. This has been previously attributed primarily to terrestrial weathering (*77*).

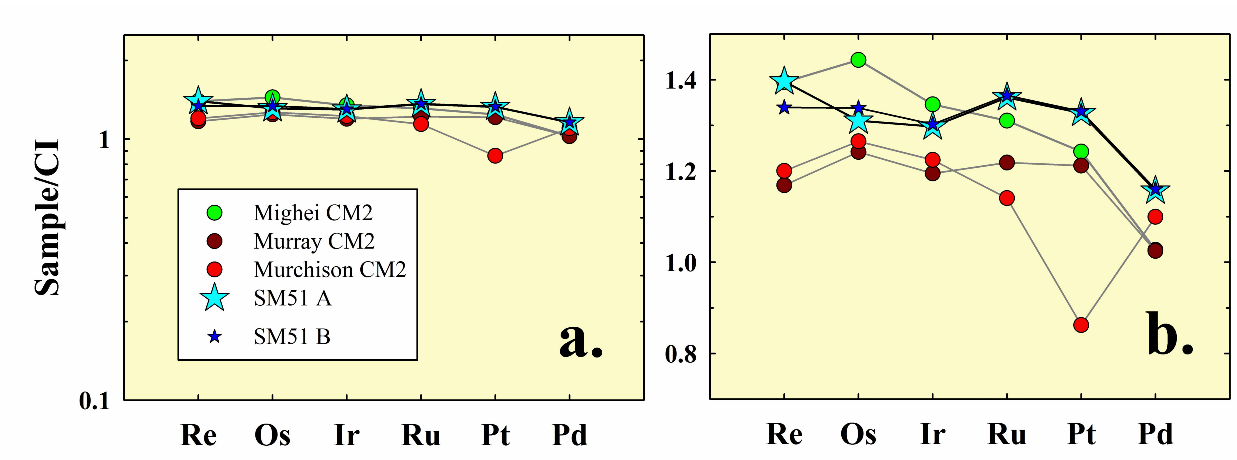

Fig. S18. Highly Siderophile Elemental (HSE) pattern normalized to CI (Orgueil). Note that the y-axis in panel (**a**) is in logarithmic scale, and in panel (**b**) is in linear scale, in which the relative differences between the meteorites are more clearly seen. In addition to Sutter's Mill (SM51A and B), a few additional type specimens of CM chondrites (Mighei, Murray and Murchison) are also shown for comparison. Data for Orgueil and the CM chondrites are from ref. 77.

2.7. Ultrahigh Precision Cr Isotope Analyses

Powdered samples of 30.87 mg (SM43) and 30.12 mg (SM51) were dissolved using concentrated HF-HNO_3 mixture in Teflon capsules sealed in stainless steel bombs and heated in the oven at 190 °C for 60 hours to make clear solutions. The sample solutions were evaporated, dissolved in 6 mol L^{-1} HCl, heated at 90 °C overnight and evaporated again. These samples were re-dissolved in 6 mol L^{-1} HCl and about 30% of the sample aliquots were taken for Cr isotope measurements. Chemical separations were achieved by cation and anion exchange resins to eliminate Cr from other major and minor elements.

Cr isotopes were determined using Thermo *TRITON-plus* thermal ionization mass spectrometer (TIMS) in a static mode at the Department of Geology, University of California, Davis. In order to minimize the effect of residual mass fractionation, a relatively large number of repeated measurements were made for each sample (4 sets of 300 ratios, 8 second integration time). About 3 μg Cr was mixed with 3 μL of silica gel-boric acid-Al type activator, and loaded onto a single W filament. All samples were bracketed by a Cr standard, SRM 979. Four filaments were prepared for each sample and standard, and two filaments for the standard were set before and after the four filaments for each sample. The instrumental mass fractionation effect was corrected according to an exponential law using a $^{50}Cr/^{52}Cr$ ratio = 0.051859 (*81*). Interferences from ^{50}V and ^{54}Fe were also corrected by monitoring ^{51}V and ^{56}Fe. The beam intensity of ^{52}Cr was set at 1×10^{-10} A (± 15%). A gain calibration and 60-s baseline were performed before each analysis and amplifiers were rotated for each block. Analytical procedures for chemical separation and isotope measurement of Cr are discussed more detail in (*82*).

Table S9. Cr isotopic data of Sutter's Mill meteorite (SM43, SM51) and Murchison measured in this study.

	$\mu^{53}Cr$	$\varepsilon^{54}Cr$
Sutter's Mill (SM 43)	14 ± 4	0.95 ± 0.09
Sutter's Mill (SM 51)	12 ± 4	0.88 ± 0.07
Murchison (CM2)	16 ± 4	0.89 ± 0.08
Murchison (*28*)	12 ± 4	0.89 ± 0.09

Notes: Reference values of Murchison are from (*28*). The $\mu^{53}Cr$ and $\varepsilon^{54}Cr$ values of the sample were calculated relative to the average of the standards ($\mu^{53}Cr = [(^{53,54}Cr/^{52}Cr)_{sample} / (^{53,54}Cr/^{52}Cr)_{standard} - 1] \times 10^6$), $\varepsilon^{54}Cr = [(^{53,54}Cr/^{52}Cr)_{sample}/(^{53,54}Cr/^{52}Cr)_{standard} - 1] \times 10^4$).

In this study, Cr isotopic analysis was also processed for Murchison (CM2), the same whole rock powder used in (*28*). The Cr isotopic values of Murchison measured in this study were identical to those of (*28*), suggesting that our Cr isotope measurements are reliable.

As shown in Table S9, both $^{53}Cr/^{52}Cr$ and $^{54}Cr/^{52}Cr$ ratios were reproduced between the two stones of SM43 and SM51, and identical within 4 ppm and 9 ppm uncertainties, respectively, at 95% confidence level to that of Murchison reported by Yin et al. (*28*) and reproduced here. Given the complex and heterogeneous nature of the Sutter's Mill meteorite observed in its petrography and mineralogy, it is surprising that two random subsamples from a regolith breccia would give identical Cr isotopic composition to the 7th decimal point and similarly so for

Murchison. Clearly, Sutter's Mill and Murchison (and other CM chondrites by inference) sample a chemical reservoir in the early solar nebula where the Cr isotope composition was fully homogenized, and subsequently locked into the minerals and stones of Sutter's Mill and other CM chondrites.

A key question is, how and when did these diverse components observed in carbonaceous chondrites, and Sutter's Mill in particular, come together? How can we devise a tool to date the formation of bulk carbonaceous chondrites (and their parent bodies)? Note that manganese (Mn) is a moderately volatile element, and Cr is a relatively refractory element (Fig. 3, main text). Mn is thus concentrated in the low-temperature matrices of the carbonaceous chondrites, whereas Cr is relatively concentrated in the refractory components (chondrules and CAIs). Depletion of moderately volatile elements is a general feature of terrestrial planets and asteroids (*83,84*). It is well established that different carbonaceous chondrite groups show a systematic and progressive depletion pattern for moderately volatile elements, e.g., Mn/Cr (*84,85*); the Mn/Cr ratio is governed by the matrix fraction in each chondrite group. This fact allows us to apply ^{53}Mn-^{53}Cr chronometry, where ^{53}Mn decays to ^{53}Cr with a half-life of 3.7 My, to constrain the timescale of accretion and compaction of the carbonaceous chondrite parent bodies (*28,86*).

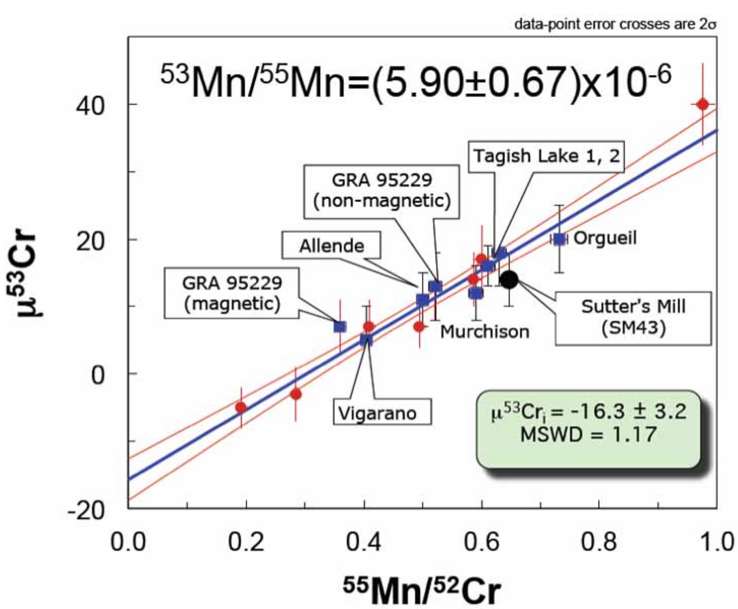

Fig. S19. ^{53}Mn-^{53}Cr fossil isochron diagram. Black solid circle is SM43 from this study. Solid blue squares are bulk carbonaceous chondrites and solid red circles are Allende chondrules *(28)*.

As shown in Fig. S19, Sutter's Mill plots on the systematic trend where the ^{55}Mn/^{52}Cr ratio correlates with μ^{53}Cr for a group of carbonaceous chondrites (blue squares, which include CI, CM, CV, CR, and Tagish Lake) and Allende (CV) chondrules (red solid circles) (*28*). The slope of this "fossil" isochron gives a ^{53}Mn/^{55}Mn ratio of (5.90±0.67) × 10^{-6}.

The precise age of basaltic angrite D'Orbigny allows consistent linking of the ^{53}Mn–^{53}Cr and other extinct nuclide chronometers to the absolute time scale. D'Orbigny has a most precise ^{53}Mn/^{55}Mn ratio = (3.24±0.04) × 10^{-6} (*87,88*). The absolute Pb–Pb age for the D'Orbigny angrite is refined to be 4,563.37±0.25 My based on the new U isotope composition (*89,90*).

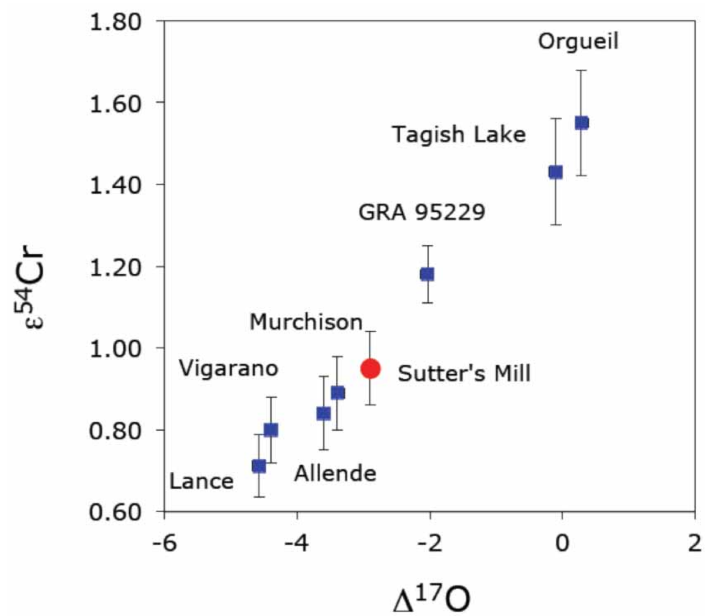

Fig. S20. Diagram of ε^{54}Cr excess versus Δ^{17}O excess (for definition see Eq. S1 below) among different carbonaceous chondrites. Data sources: Solid red circle (this work). Solid blue squares (*28*). See Eq. S1 in section 2.8 for the definition of Δ^{17}O.

Compared to the D'Orbigny age anchor, the slope of ^{53}Mn/^{55}Mn = (5.90±0.67) × 10^{-6} defined by Sutter's Mill and other carbonaceous chondrites (Fig. S20) translates into an absolute age of 4,566.57±0.66 My. This suggests a nebula-wide, moderately volatile element depletion event has occurred within ±0.66 My. It constrains the timescale of accretion and compaction of the carbonaceous chondrite parent bodies, including that of Sutter's Mill (this work), to within ~ 1 Ma (*28*) after CAI formation at 4,567.60±0.36 My (*90,91*). This suggests the first stage of planet formation from dust to planetesimals is completed within ~1 My (*28,86*). The nuclear anomaly of ε^{54}Cr *vs.* Δ^{17}O plot (Fig. S20) places Sutter's Mill squarely in the CM field (*28*). ^{54}Cr, together with few other nuclear anomalies, is becoming a tool on par with Δ^{17}O to classify meteorites (*92*).

2.8. Oxygen Isotope Analyses

Laser Fluorination

The oxygen isotopic compositions of silicates in SM43 were measured using the laser fluorination technique of Farquhar and Thiemens (*93*) at UC San Diego. SM43 was separated into 1-2mg aliquots, which were laser fluorinated in a single session. Data were normalized to the NBS-28 quartz standard, samples of which were analyzed immediately before and after the meteorite analyses. The isotopic compositions of the product O_2 were measured on a Finnigan MAT 253, and average uncertainty in $^{18}O/^{16}O$ is ± 0.03‰ (1σ) and $^{17}O/^{16}O$ is ± 0.06‰ (1σ).

Oxygen isotope analyses at UCLA were performed by infrared laser-assisted fluorination following the general method developed by (*94*) and modified for triple-oxygen isotope ratio analysis by (*95*). Oxygen isotope ratios were measured on oxygen (as O_2 gas) extracted from the meteorite by heating with a 20 Watt CO_2 laser in the presence of purified F_2 gas. The fluorine gas was delivered to the samples by heating $K_2NiF_6 \cdot KF$ powder to a temperature greater than 250 °C. The laser was operated at 5 to 11 W with 10 Hz beam modulation. Liberated O_2 was separated from residual F_2 by reaction of the latter over hot KBr and cryogenic trapping of Br_2 gas, then trapped onto molecular sieve 13X at -196 °C. Ubiquitous trace amounts of NF_3 cause $^{17}O^{16}O$ interferences (at mass/charge = 33) due to NF produced in the source of the mass spectrometer. Trace NF_3 was removed by distilling the oxygen from the 13X molecular sieve at -130 °C to a second molecular sieve at -196 °C for 30 minutes. Analyte oxygen was expanded directly from the second molecular sieve into one side of the dual inlet of the isotope ratio mass spectrometer by heating to > 110°C for 30 minutes. Simultaneous measurements of $^{33}O_2/^{32}O_2$ and $^{34}O_2/^{32}O_2$ (yielding $^{17}O/^{16}O$ and $^{18}O/^{16}O$, respectively) were made on a ThermoFinnigan MAT Delta mass spectrometer. Six blocks of 20 cycles, each cycle consisting of an 8 second integration, comprised each measurement. Quoted uncertainties are 1 standard error (standard deviation about the mean) for the six blocks.

Oxygen isotope data from both UCSD and UCLA are consistently reported in Table S10 as $\delta^{17}O'$ and $\delta^{18}O'$ defined as: $\delta^{xx}O = 1000 \times \ln(1 + \delta^{xx}O/1000)$, where ^{xx}O refers to either ^{17}O or ^{18}O, respectively, and $\delta^{xx}O$ in turn is parts per 1,000 deviations from Standard Mean Ocean Water (SMOW) as the reference, $\delta^{xx}O = [(^{xx}O/^{16}O)_{Sample}/(^{xx}O/^{16}O)_{SMOW} - 1] \times 1000$. The $\Delta^{17}O$

values reported are relative to a mass fractionation curve passing through the origin on the Standard Mean Ocean Water scale with an exponent β which relates the mass fractionation factors for $^{17}O/^{16}O$ and $^{18}O/^{16}O$ according to the relation $\alpha_{17} = \alpha_{18}^{\beta}$ (*96*), where α_{17} = $(^{17}O/^{16}O)_{Sample}/(^{17}O/^{16}O)_{SMOW}$, and α_{18} = $(^{18}O/^{16}O)_{Sample}/(^{18}O/^{16}O)_{SMOW}$. Thus $\Delta^{17}O$ is calculated consistently and accurately as

$$\Delta^{17}O = \delta^{17}O' - \beta \times \delta^{18}O' = 1000[\ln(\alpha_{17}) - \beta \times \ln(\alpha_{18})] \qquad (Eq.\ S1)$$

which is used to assess the deviation from the empirically defined Terrestrial Fractionation Line (TFL) as in (*97*). $\Delta^{17}O$ calculated using β = 0.528 (UCLA) and β = 0.5247 (UCSD) are both shown in Table S10 in two separate columns. The tank O_2 used as an internal standard in this study at UCLA was calibrated against air O_2 ($\delta^{18}O_{SMOW}$ = 23.5 per mil, $\Delta^{17}O$ = -0.35 per mil) and San Carlos olivine ($\delta^{18}O_{SMOW}$ = 5.2 per mil, $\Delta^{17}O$ = 0.00 per mil).

Table S10: Oxygen isotopic composition of Sutter's Mill meteorite: Laser Fluorination using BrF5. Isotopes relative to SMOW, measured isotopic compositions have been corrected for contribution from blank in laser fluorination system and have been compared to measured compositions of laser fluorinated samples of NBS-28 quartz standard (UCSD) and of San Carlos olivine standard (UCLA).

Sample ID	$\delta^{17}O$ (‰)	±1σ (‰)	$\delta^{18}O$ (‰)	±1σ (‰)	$\Delta^{17}O$ (‰) β=0.528	$\Delta^{17}O$ (‰) β=0.5247	±1σ (‰)	Lab
SM43-2	4.034	0.044	11.351	0.028	-1.960	-1.922	0.029	UCSD
SM43-3	3.630	0.073	10.658	0.044	-1.997	-1.962	0.050	UCSD
SM43-4	3.643	0.058	10.436	0.013	-1.867	-1.833	0.051	UCSD
SM43-6	3.757	0.052	10.763	0.037	-1.926	-1.890	0.033	UCSD
SM43-8	4.033	0.053	10.564	0.023	-1.545	-1.510	0.041	UCSD
SM51-1	5.898	0.010	16.657	0.011	-2.898	-2.843	0.007	UCLA
SM51-2	6.167	0.018	16.824	0.003	-2.716	-2.660	0.018	UCLA

Secondary Ion Mass Spectrometry (SIMS)

Oxygen-isotope compositions of olivines and carbonates were measured *in situ* with the UH Cameca ims-1280 SIMS. A ~0.8-1.2 nA Cs^+ primary ion beam was focused to a diameter of ~5 μm and rastered over ~10 × 10 μm^2 area for presputtering (120 seconds). After presputtering, the raster size was reduced to 7 × 7 μm^2 for automated centering of the secondary ion beam followed by data collection. An energy window of 40 eV was used. Normal incident electron flood gun was used for charge compensation with homogeneous electron density over region of ~70 μm in diameter. Three oxygen isotopes ($^{16}O^-$, $^{18}O^-$, and $^{17}O^-$) were measured in multicollection mode using the multicollection Faraday cups L'2 and H1 and the monocollection electron multiplier, respectively. Mass-resolving power for $^{17}O^{-}$ and for $^{16}O^{-}$ and $^{18}O^{-}$ were set to ~5,500 and ~2,000, respectively. $^{16}OH^{-}$ signal was monitored in every spot measured for oxygen isotopes and was typically less than 10^6 cps, while typical $^{17}O^{-}$ count rate was 2×10^5 cps. Contribution of $^{16}OH^{-}$ onto $^{17}O^{-}$ was corrected based on a peak/tail ratio measured in same analytical session. The correction was typically less than 0.1‰ (~0.2‰ at most).

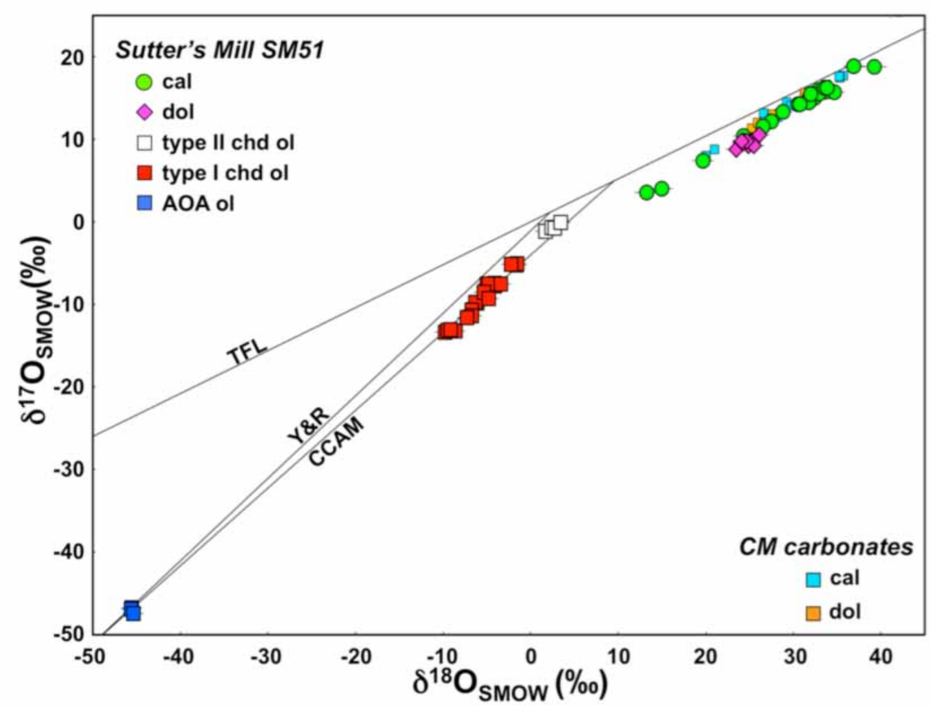

Fig. S21. Oxygen-isotope compositions of calcite, dolomite and olivines in type I and II chondrules, and amoeboid olivine aggregates from SM51 (this study), and bulk calcite and dolomite from other CM chondrites, data from (*34*). TFL: terrestrial fractionation line; CCAM: carbonaceous chondrite anhydrous mineral line (*44*); Y&R: Young and Russell line (*48*).

Instrumental mass fractionation effects for olivine, calcite, and dolomite were corrected by analyzing San Carlos olivine, UWC-1 calcite, and UW6250 dolomite standards, respectively. The standards were analyzed repeatedly before and after each run. Reported errors (2σ) include both the internal measurement precision and the external reproducibility (~0.6-1.2‰ (2SD) in both $\delta^{17}O$ and $\delta^{18}O$) of standard data obtained during a given session. After analysis, the location of each probe spot was re-imaged to check for beam overlap between phases, and to identify large cracks or impurities that may have affected the result. Oxygen-isotope compositions of chondrule and AOA olivines (Fig. S21) plot along the carbonaceous chondrite anhydrous mineral CCAM line; ferroan chondrule olivines ($Fa_{27\text{-}46}$) are ^{16}O-depleted ($\Delta^{17}O = \delta^{17}O - 0.52\times\delta^{18}O \sim -2.0$‰) relative to magnesian ($Fa_{0.5\text{-}2}$) olivines in chondrules ($\Delta^{17}O \sim -4.0$ to -8.7‰, respectively) and AOAs ($\Delta^{17}O \sim -23$‰). Note that $\Delta^{17}O = \delta^{17}O - 0.52\times\delta^{18}O$ is simply the first-order Taylor expansion of the Eq. S1.

Table S11. Oxygen-isotope compositions of olivines in AOAs, type I and type II chondrules in Sutter's Mill, SM51-1.

mineral	$\delta^{18}O$	2σ	$\delta^{17}O$	2σ	$\Delta^{17}O$	2σ
AOA	-45.6	1.2	-46.8	0.8	-23.1	1.0
AOA	-45.7	1.1	-46.9	0.8	-23.1	1.0
AOA	-45.4	1.2	-47.4	0.8	-23.8	1.0
type I chd	-1.6	1.1	-5.2	0.8	-4.4	1.0
type I chd	-1.5	1.1	-5.1	0.8	-4.3	1.0
type I chd	-2.2	1.1	-5.1	0.8	-4.0	1.0
type I chd	3.5	1.1	-0.1	0.7	-1.9	0.9
type I chd	-4.1	1.2	-7.4	0.7	-5.3	0.9
type I chd	-4.1	1.1	-7.8	0.8	-5.6	1.0
type I chd	-5.0	1.1	-7.5	0.7	-4.9	0.9
type I chd	-4.8	1.1	-7.5	0.8	-5.1	1.0
type I chd	-3.4	1.1	-7.5	0.8	-5.7	1.0
type I chd	-9.7	1.2	-13.4	0.8	-8.3	1.0
type I chd	-9.5	1.1	-13.1	0.8	-8.2	1.0
type I chd	-8.6	1.1	-13.2	0.7	-8.7	1.0
type I chd	-9.1	1.1	-13.1	0.8	-8.3	0.9
type I chd	-6.1	1.2	-9.8	0.8	-6.6	1.0
type I chd	-6.3	1.1	-9.8	0.8	-6.5	1.0
type I chd	-6.8	1.1	-10.7	0.8	-7.2	1.0
type I chd	-6.7	1.1	-11.4	0.8	-7.9	1.0
type I chd	-7.3	1.1	-11.6	0.8	-7.8	1.0
type I chd	-5.4	1.2	-8.5	0.8	-5.7	1.0
type I chd	-4.8	1.1	-9.3	0.8	-6.8	1.0
type II chd	1.7	1.1	-1.1	0.8	-2.0	1.0
type II chd	2.4	1.1	-0.7	0.7	-1.9	0.9
type II chd	2.7	1.2	-0.7	0.7	-2.2	0.9
type II chd	3.5	1.1	-0.1	0.7	-1.9	0.9

Aqueous alteration resulted in replacement of primary anhydrous minerals by phyllosilicates, magnetite, Fe,Ni-sulfides, and carbonates – calcite ($CaCO_3$) and dolomite ($(Ca,Mg,Mn)CO_3$) (Figs. 2b−d, main text). On a three-isotope oxygen diagram ($\delta^{17}O$ *vs.* $\delta^{18}O$), calcites show a large range of $\delta^{18}O$ (+13‰ to +39‰) with $\Delta^{17}O$ (= $\delta^{17}O - 0.52\times\delta^{18}O$) decreasing from −0.3‰ to

−3.8‰ with most values near the lower value that is similar to primary silicates (Fig. S21). Overall the trend is one of highly variable $\delta^{18}O$ at a largely invariant $\Delta^{17}O$ that encompasses the range in both parameters exhibited by both CM and CI carbonates (Fig. 4, main text). Such a trend requires a buffering of the fluid by exchange with rock over a large range of temperatures (*33*).

Table S12. Oxygen-isotope compositions of carbonates in Sutter's Mill, SM51-1.

mineral	$\delta^{18}O$	2σ	$\delta^{17}O$	2σ	$\Delta^{17}O$	2σ
dolomite	24.8	1.1	9.3	1.1	-3.6	1.2
dolomite	25.2	1.2	9.8	1.1	-3.3	1.2
dolomite	25.1	1.2	9.7	1.1	-3.4	1.3
dolomite	24.1	1.1	9.7	1.1	-2.9	1.2
dolomite	26.1	1.2	10.6	1.1	-3.0	1.2
dolomite	25.5	1.2	9.3	1.1	-4.0	1.3
dolomite	24.3	1.1	9.8	1.1	-2.8	1.3
dolomite	23.5	1.1	8.8	1.1	-3.4	1.2
dolomite	24.2	1.2	9.5	1.1	-3.1	1.2
dolomite	24.6	1.2	9.8	1.1	-3.0	1.2
dolomite	24.1	1.1	9.8	1.1	-2.8	1.2
calcite	32.5	1.4	15.3	0.9	-1.7	1.2
calcite	33.7	1.3	15.8	0.9	-1.7	1.1
calcite	30.5	1.3	14.3	0.9	-1.6	1.1
calcite	31.8	1.2	15.1	0.9	-1.5	1.1
calcite	24.3	1.2	10.4	0.9	-2.2	1.1
calcite	19.7	1.2	7.4	0.9	-2.8	1.1
calcite	32.9	1.2	15.9	0.9	-1.1	1.1
calcite	32.4	1.3	15.0	1.0	-1.8	1.2
calcite	31.8	1.2	14.5	0.9	-2.1	1.1
calcite	34.6	1.2	15.7	0.9	-2.3	1.1
calcite	13.2	1.3	3.5	1.0	-3.3	1.2
calcite	28.8	1.1	13.3	0.9	-1.7	1.0
calcite	30.8	1.6	14.2	1.0	-1.8	1.3
calcite	27.5	1.4	12.2	0.9	-2.1	1.1
calcite	33.0	1.3	15.5	0.9	-1.6	1.1
calcite	33.6	1.2	16.2	1.0	-1.2	1.2
calcite	39.2	1.5	18.8	0.9	-1.6	1.2
calcite	36.9	1.2	18.8	0.9	-0.3	1.1
calcite	33.9	1.3	16.3	0.8	-1.3	1.1
calcite	32.0	1.3	15.4	1.0	-1.2	1.2
calcite	26.5	1.1	11.6	0.8	-2.2	1.0
calcite	15.0	1.2	4.0	0.9	-3.8	1.1

Calcites show a large spread of $\delta^{18}O$ value (+13‰ to +39‰) with $\Delta^{17}O = -1.9 \pm 1.5$‰. A trend line regressed through the calcite data (Fig. S21), $\delta^{17}O = 0.62 \times \delta^{18}O - 4.88$, is nearly identical to that reported for CM calcites by Benedix *et al.* (*34*), and tracks evolution of fluid composition from higher to lower $\Delta^{17}O$ values with increasing degree of alteration of the CM parent body.

Dolomites from both lithologies are tightly clustered around $\delta^{18}O \sim +25$‰ with $\Delta^{17}O = -3.2 \pm 0.7$‰ (average ±2 standard deviations), suggesting late-stage precipitation of dolomite under stringent physico-chemical conditions. Bulk oxygen-isotope composition of SM43 plots in the field of the extensively aqueously altered CMs, whereas that of SM51 extends the currently known CM field (Fig. 4, main text), possibly due to higher abundance of $\delta^{18}O$-rich carbonates.

2.9. C, N, and Ar Isotope Analyses

The abundance and isotopic composition of carbon, nitrogen and argon were determined by stepped combustion-mass spectrometry (Finesse instrument) at the Open University (*98,99*) in two separate analytical sessions using 3.565 mg and 6.34 mg chips of whole-rock meteorite from

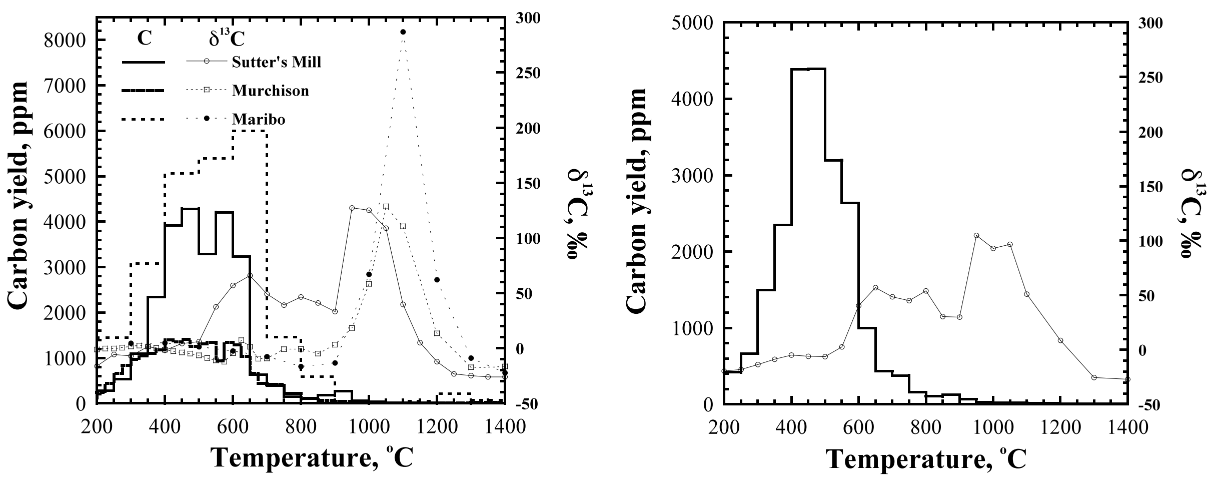

Fig. S22. Stepwise combustion yield of C content and $\delta^{13}C$ for Sutter's Mill meteorite (SM43), Murchison (CM), and Maribo (CM). The repeat measurement (right) is also for sample of SM43. The carbon isotope profile in a duplicate sample (left panel Fig. S22) is well reproduced, though the total $\delta^{13}C$ is lower (6.4 compared to 28.5). This could occur if less carbonate was present in the second aliquot (Table S14). Carbon release is also a bit different and may indicate a smaller amount of carbonate as well.

SM43. The chip was wrapped in platinum foil, then heated under excess oxygen in increments from room temperature to 1400 °C. Data were corrected for system blank. The results are shown below in Table S13 and S14.

Table S13. The abundance and isotopic composition of carbon and argon in stepwise combustion.

Temp °C	C ppm	$\delta^{13}C$	^{40}Ar cc	$^{40}Ar/^{36}Ar$	^{36}Ar corr cc/g
200	158.3	-16.3	3.92E-08	253.3	6.12E-09
250	284	-5.6	2.97E-08	198.1	1.38E-08
300	535.4	-7	2.89E-08	124.5	3.77E-08
350	1090.6	1.6	1.44E-08	51.6	6.45E-08
400	2332.8	-1.9	1.17E-08	27.8	1.07E-07
450	3908.4	4.2	8.17E-09	13.2	1.65E-07
500	4281.1	5.9	6.02E-09	8.5	1.93E-07
550	3290.5	37.6	6.21E-09	18.7	8.71E-08
600	4205.9	57	5.24E-09	72.2	1.54E-08
650	3233.4	65.8	5.27E-09	205.1	2.20E-09
700	631	49	4.23E-09	214	1.52E-09
750	390.4	39.1	9.33E-09	222.2	2.91E-09
800	155	46.5	4.42E-09	187.7	2.40E-09
850	100.3	41.2	3.70E-09	260.6	4.64E-10
900	177.6	33.3	4.94E-09	203	2.13E-09
950	268	127.2	3.65E-09	240.4	7.88E-10
1000	60.9	125.1	3.84E-09	241	8.20E-10
1050	36.2	108.7	3.63E-09	284.7	1.25E-10
1100	20.5	39.6	4.25E-09	249.7	7.33E-10
1150	13.4	5	4.48E-09	291.3	5.45E-11
1200	7.5	-12.1	4.54E-09	256.9	6.40E-10
1250	4.6	-23.3	5.61E-09	231.7	1.46E-09
1300	4.4	-24.8	6.22E-09	248.1	1.12E-09
1350	4.8	-25.8	7.20E-09	275.3	4.91E-10
1400	6.1	-25.8	6.39E-09	288.7	1.33E-10
	25201.1	28.5			7.07E-07

Table S14. The abundance and isotopic composition of carbon, nitrogen, helium, argon and xenon stepwise combustion.

Temp ºC	C ppm	$\delta^{13}C$	1σ	N ppm	$\delta^{15}N$	1σ	^{4}He cc/g	^{36}Ar cc/g	^{132}Xe cc/g
200	128.1	-19.5	0.51	4.2	13.5	0.5	4.07E-08	3.71E-09	2.87E-10
250	422.7	-18.1	0.31	11.1	-5.3	0.2	4.32E-07	1.29E-08	2.50E-10
300	664.8	-13.5	0.64	10.6	-1.7	0.2	4.97E-07	3.54E-08	2.37E-11
350	1492.6	-8.7	0.5	18.2	-3.6	0.2	8.20E-07	4.73E-08	7.28E-11
400	2345.1	-5	0.78	34.7	-8	0.2	1.16E-06	7.89E-08	1.75E-10
450	4381.6	-6.1	0.52	136.7	-17.3	0.1	3.26E-06	1.78E-07	3.33E-10
500	4394.4	-6.3	0.44	165.7	-11	0.1	6.59E-06	2.24E-07	2.04E-10
550	3194.3	2.7	0.95	107.3	18	0.1	7.06E-06	1.40E-07	9.50E-11
600	2635.3	40.5	1.13	26.4	42.7	0.2	6.32E-07	3.94E-08	2.61E-11
650	994.8	56.9	0.77	7.7	25.9	0.3	2.28E-07	3.14E-09	3.42E-11
700	435.8	48.6	1.05	8.6	13	0.2	2.12E-07	2.62E-09	4.94E-11
750	377.9	45.2	0.4	10.9	23.6	0.2	8.45E-08	3.85E-09	5.50E-11
800	158.8	54.2	0.44	2.8	14.3	0.6	6.10E-08	1.56E-09	3.49E-12
850	103	30.5	0.32	4.3	38.7	0.4		2.37E-09	4.53E-12
900	125.3	30.1	0.53	6.2	52.2	0.3		3.43E-09	4.37E-12
950	65.5	104.8	0.55	1.6	7.8	1		4.54E-09	8.03E-12
1000	31.8	93	0.48	0.3	3.5	5.1			
1050	24	96.7	0.49	0.4	7.2	3.7			
1100	18.8	51.1	0.56	0.5	16	3.4			
1200	14.9	8.7	0.54	0.3	24.9	4.6			
1300	10.6	-25.5	0.45	0.2	37.5	7.2			
1400	7.3	-27	0.23	0.3	42.9	4.9			
	22027	6.4		559.1	-0.6		2.11E-05	7.81E-07	1.63E-09

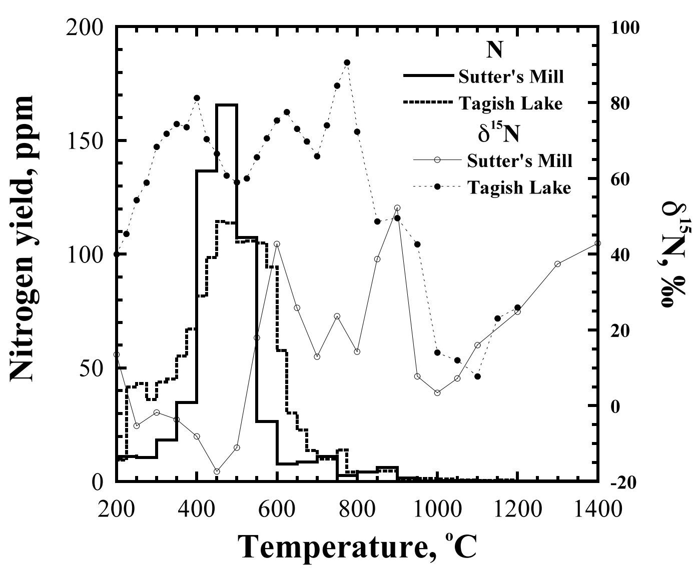

Fig. S23. Organic nitrogen associated with carbon is significantly lighter than in Tagish Lake (and Murchison). The similarity in the N isotope profiles for the meteorites at high T can be explained by the light N signature of SiC.

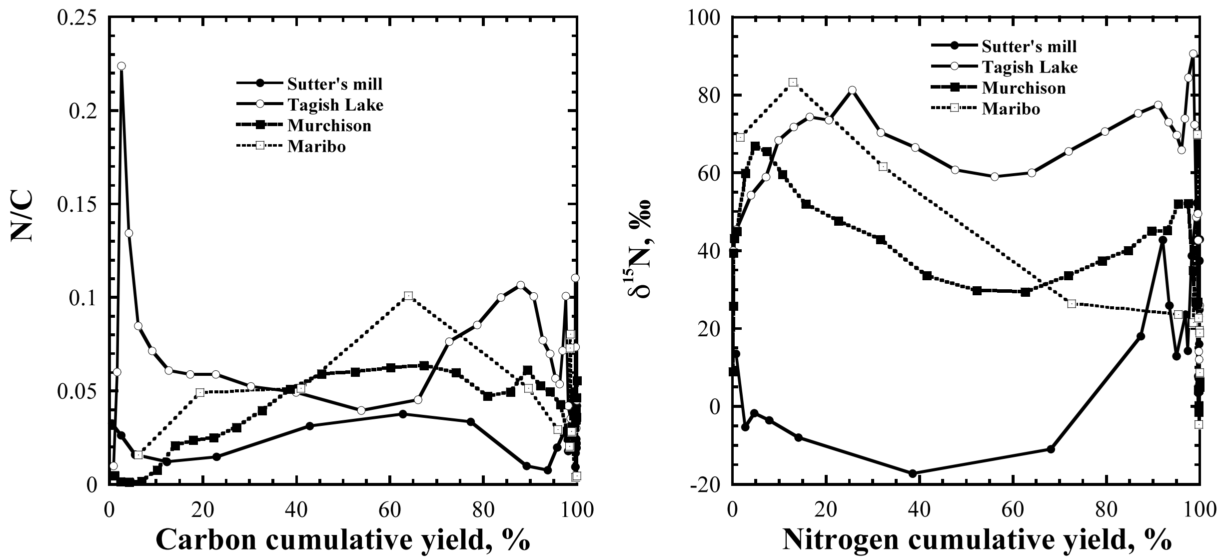

Fig. S24. Sutter's Mill has the lowest N/C ratio $\delta^{15}N$, compared to other CM meteorites, suggesting Sutter's Mill contains different organic nitrogen components.

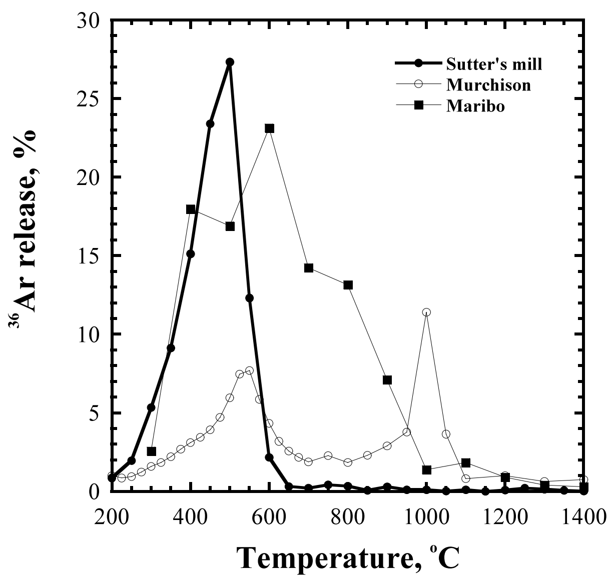

Fig. S25. Stepwise release pattern of ^{36}Ar for Sutter's Mill (SM43), Murchison, and Maribo. All noble gases are released at the same time with carbon indicating that their carrier is carbonaceous.

Almost 95% of the carbon in SM43 combusted below 650ºC; the $\delta^{13}C$ increased with temperature from -16 to +65‰. Carbon and nitrogen isotopic compositions vary widely between fragments, with $\delta^{13}C$ and $\delta^{15}N$ values ranging between −13‰ and +28.5‰ and between −0.6‰ and +16.7‰, respectively.

2.10. Noble Gases (He, Ne, Ar, Kr and Xe)

Chips weighing 2.346 and 3.169 mg separated from SM43, and 1.638 and 4.029 mg from SM51 were used for noble gas analysis with a modified-MM5400 noble gas mass spectrometer at the Department of Earth and Planetary Sciences, Kyushu University. The mass spectrometer is equipped with noble gas extraction furnace and noble gas purification line with two Ti-Zr getters and two charcoal traps. Each sample was wrapped in thin Al-foil and all the samples were installed in a sample holder attached to the furnace. Whole extraction furnace and purification line for noble gases were heated at about 250 ºC for a day under ultra-high vacuum condition to remove atmospheric contamination. During the heating procedure, the meteorite samples were kept at ca. 130 ºC to remove atmospheric noble gas contamination. Prior to noble gas extraction from the samples in a Mo-crucible of the extraction furnace, the crucible was degassed at the temperature of ca. 1900 ºC repeatedly to lower the blank level.

Noble gases were extracted by totally melt the samples, SM43-1 (the 2.346 mg fragment) and SM51-2 (the 1.638 mg fragment) at 1800 ºC in the Mo-crucible. Remaining two samples, the 3.169 mg fragment of SM43-2 and the 4.029 mg fragment of SM51-1 were heated stepwise at the temperatures of 600, 900, 1400, and 1800 ºC to extract noble gases of different origins separately.

Sensitivities and mass discrimination correction factors for noble gases were determined by measuring a known amount of atmosphere. Mass discrimination for $^{3}He/^{4}He$ ratio was determined using a ^{3}He and ^{4}He mixture with $^{3}He/^{4}He = 1.71 \times 10^{-4}$. Blank levels were 2×10^{-11}, 2×10^{-12}, 7×10^{-10}, 4×10^{-14}, and 1×10^{-14} $cm^{3}STP$ for ^{4}He, ^{20}Ne, ^{40}Ar, ^{84}Kr, and ^{132}Xe, respectively. The blank correction was applied to all the noble gas data. Experimental errors for isotopic ratios are given in terms 1σ, and the uncertainties for concentration determination are estimated to be about 10 % of a given value.

The elemental and isotopic compositions of noble gases determined for 4 fragments from the Sutter's Mill meteorite, SM43 and SM51, are presented in Tables S15 through S17. Elemental ratios among Ar, Kr, and Xe show that heavy noble gases in this meteorite are dominated by Q-gas (Fig. S26), which is a main noble gas component trapped in Q-phases in chondrites. The concentrations are as high as those observed in CM2 chondrites, consistent with the classification of this meteorite. A datum point for 600 ºC of SM43 sample apart from Q-component indicates desorption of terrestrial atmospheric contamination (Fig. S26 and Table S15). The terrestrial contamination is supported by the $^{40}Ar/^{36}Ar$ ratio of 273 in this fraction, which is close to atmospheric value of 296. In contrast to the SM43, degree of atmospheric contamination for SM51 is insignificant (Fig. S26).

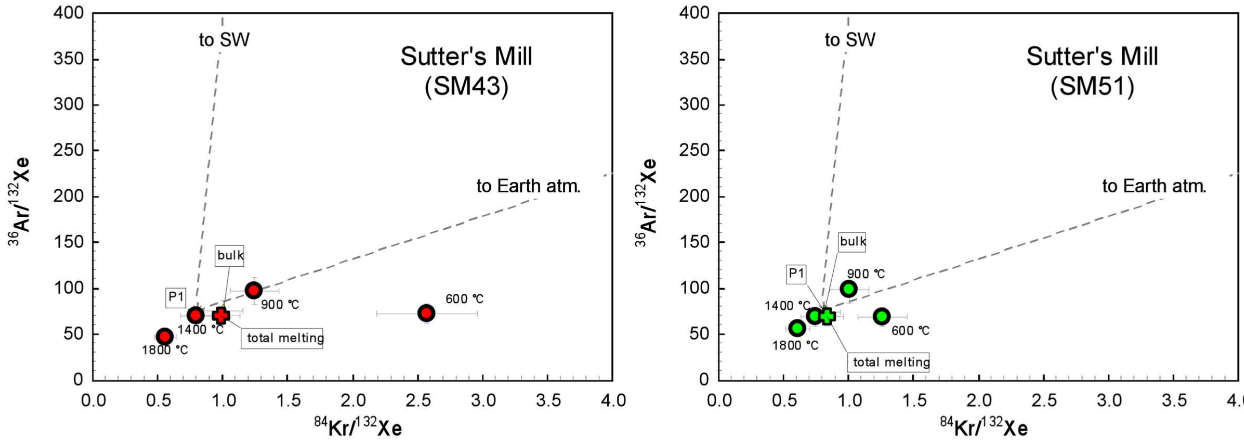

Fig. S26. Elemental compositions of Ar, Kr, and Xe for SM43 (left) and SM51 (right).

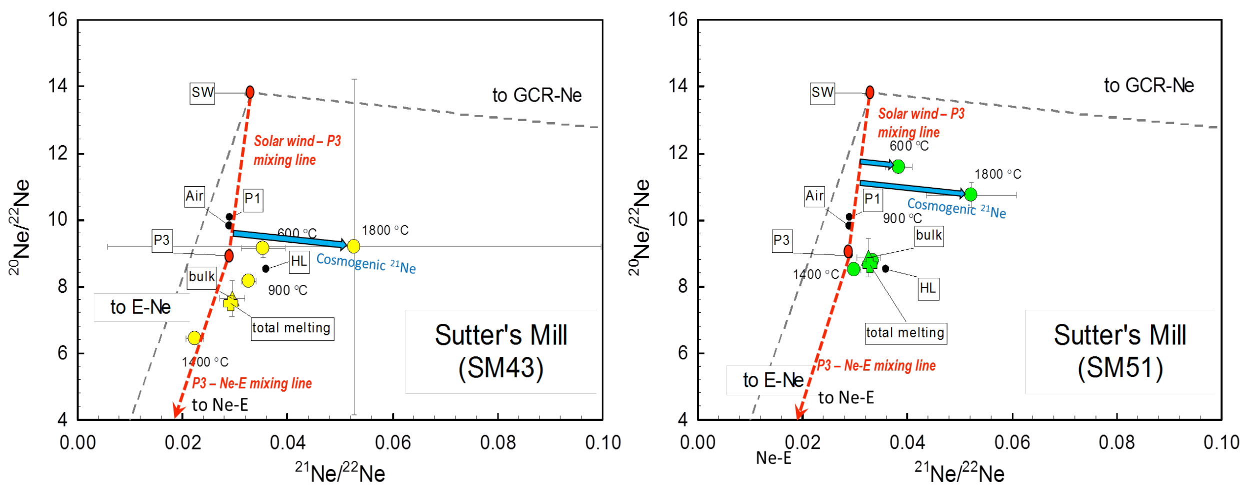

Fig. S27. Ne three isotope plot for SM43 (left) and SM51 (right).

The $^3He/^4He$ ratios (Table S15) are as low as (1.6-1.9) × 10^{-4}, which are similar to or slightly higher than those of primitive trapped components, Q (1.23 × 10^{-4}), P3 (≤1.35 × 10^{-4}), and HL (≤1.7 × 10^{-4}), but distinctly lower than the present-day solar wind value (4.64 × 10^{-4}). Hence, it is difficult to estimate concentrations of cosmic-ray produced ^3He for this meteorite, because in most cases $^3He/^4He$ ratios are much higher than the solar value by production of cosmogenic He isotopes with $^3He/^4He$ ratio of ~0.2. The U, Th-He age is also difficult to estimate because of abundant primordial He as shown by the $^3He/^4He$ ratios and elemental compositions.

Table S15. Noble gas concentrations and isotopic ratios of He, Ne, and Ar of Sutter's Mill SM43 and SM51. Concentrations are in the unit of 10^{-9} cm^3-STP/g.

SM43-2	**^{4}He**	**^{3}He/^{4}He**	**^{22}Ne**	**^{20}Ne/^{22}Ne**	**^{21}Ne/^{22}Ne**
600 °C	603	0.000157 ± 0.000011	1.01	9.13 ± 0.26	0.0354 ± 0.0042
900 °C	21600	0.000158 ± 0.000009	12.0	8.138 ± 0.049	0.0327 ± 0.0014
1400 °C	4830	0.000185 ± 0.000059	6.34	6.421 ± 0.054	0.0224 ± 0.0017
1800 °C	6.80	0.00061 ± 0.00036	0.0301	9.2 ± 5.0	0.053 ± 0.047
Total	27040	0.000163	19.4	7.630	0.0295

SM43-1	**^{4}He**	**^{3}He/^{4}He**	**^{22}Ne**	**^{20}Ne/^{22}Ne**	**^{21}Ne/^{22}Ne**
1800 °C	28200	0.0001855 ± 0.0000072	20.6	7.487 ± 0.077	0.02921 ± 0.00094

SM51-1	**^{4}He**	**^{3}He/^{4}He**	**^{22}Ne**	**^{20}Ne/^{22}Ne**	**^{21}Ne/^{22}Ne**
600 °C	446	0.000269 ± 0.000020	1.85	11.57 ± 0.17	0.0384 ± 0.0026
900 °C	28600	0.0001949 ± 0.0000084	15.5	8.754 ± 0.033	0.03347 ± 0.00093
1400 °C	7450	0.000187 ± 0.000015	12.2	8.486 ± 0.063	0.0300 ± 0.0012
1800 °C	7.92	0.00038 ± 0.00040	0.474	10.72 ± 0.37	0.0523 ± 0.0086
Total	36504	0.000194	30.0	8.85	0.0326

SM51-2	**^{4}He**	**^{3}He/^{4}He**	**^{22}Ne**	**^{20}Ne/^{22}Ne**	**^{21}Ne/^{22}Ne**
1800 °C	32600	0.000175 ± 0.000014	24.6	8.628 ± 0.061	0.0329 ± 0.0011

Neon isotopic ratios (Fig. S27) show interesting features for two different specimens. The main component of Ne in the SM43 sample is HL or P3, and a small amount of Ne-E(H) is observed in 1400 ºC fraction (Fig. S27). The carrier phases of the HL and P3 components are presolar diamonds, while Ne-E(H) is known to be trapped in presolar SiC grains. In the case of the SM51, on the other hand, Ne in 900 and 1400 ºC fractions plots close to HL and P3, but the datum point of 600 ºC fraction plots in a region related with noble gas component of solar origin (Fig. S27). No indication of Ne-E(H) in this sample was observed. The presence of Ne component related to solar Ne might have resulted from an implantation of solar gases to surface materials of the parent asteroid (*26*).

Table S15 (cont.).

SM43-2	**^{36}Ar**	**^{38}Ar/^{36}Ar**	**^{40}Ar/^{36}Ar**	**^{84}Kr**	**^{132}Xe**
600 °C	44.4	0.1899 ± 0.0030	272.6 ± 4.1	1.59	0.617
900 °C	197	0.1862 ± 0.0015	24.04 ± 0.50	2.55	2.04
1400 °C	442	0.1866 ± 0.0015	2.98 ± 0.17	5.11	6.38
1800 °C	12.0	0.1835 ± 0.0040	6.6 ± 5.9	0.147	0.261
Total	695	0.1866	26.23	9.4	9.3

Sm43-1	**^{36}Ar**	**^{38}Ar/^{36}Ar**	**^{40}Ar/^{36}Ar**	**^{84}Kr**	**^{132}Xe**
1800 °C	705	0.1880 ± 0.0014	27.78 ± 0.34	10.0	10.1

SM51-1	**^{36}Ar**	**^{38}Ar/^{36}Ar**	**^{40}Ar/^{36}Ar**	**^{84}Kr**	**^{132}Xe**
600 °C	25.9	0.1870 ± 0.0026	163.7 ± 2.9	0.481	0.380
900 °C	190	0.1870 ± 0.0016	10.41 ± 0.38	1.96	1.94
1400 °C	512	0.1867 ± 0.0013	1.43 ± 0.11	5.65	7.51
1800 °C	13.9	0.1887 ± 0.0029	5.4 ± 4.0	0.155	0.252
Total	742	0.1868	9.47	8.25	10.1

SM51-2	**^{36}Ar**	**^{38}Ar/^{36}Ar**	**^{40}Ar/^{36}Ar**	**^{84}Kr**	**^{132}Xe**
1800 °C	656	0.1856 ± 0.0013	13.30 ± 0.29	8.03	9.57

Table S16: Isotope ratios of Kr in the Sutter's Mill CM chondrite. Concentrations are in the unit of 10^{-9} cm^3-STP/g.

SM43-2	^{84}Kr	$^{78}Kr/^{84}Kr$	$^{80}Kr/^{84}Kr$	$^{82}Kr/^{84}Kr$	$^{83}Kr/^{84}Kr$	$^{86}Kr/^{84}Kr$
600 °C	1.59	0.00629	0.03770	0.1923	0.1948	0.3062
		± 0.00057	± 0.00108	± 0.0028	± 0.0041	± 0.0059
900 °C	2.55	0.00561	0.03886	0.1938	0.1996	0.3130
		± 0.00050	± 0.00131	± 0.0029	± 0.0040	± 0.0048
1400 °C	5.11	0.00588	0.03765	0.1948	0.2006	0.3098
		± 0.00013	± 0.00094	± 0.0037	± 0.0029	± 0.0044
1800 °C	0.15	0.0063	0.0408	0.198	0.199	0.320
		± 0.0014	± 0.0047	± 0.011	± 0.013	± 0.014
Total	9.40	0.00588	0.0380	0.1942	0.1993	0.3102

SM43-1	^{84}Kr	$^{78}Kr/^{84}Kr$	$^{80}Kr/^{84}Kr$	$^{82}Kr/^{84}Kr$	$^{83}Kr/^{84}Kr$	$^{86}Kr/^{84}Kr$
1800 °C	10.0	0.00593	0.03927	0.1985	0.2030	0.3127
		± 0.00023	± 0.00064	± 0.0022	± 0.0030	± 0.0023

SM 51-1	^{84}Kr	$^{78}Kr/^{84}Kr$	$^{80}Kr/^{84}Kr$	$^{82}Kr/^{84}Kr$	$^{83}Kr/^{84}Kr$	$^{86}Kr/^{84}Kr$
600 °C		0.00618	0.04029	0.1899	0.1961	0.3083
	0.481	± 0.00081	± 0.00475	± 0.0063	± 0.0058	± 0.0099
900 °C	1.96	0.00608	0.03882	0.1909	0.1970	0.3100
		± 0.00042	± 0.00088	± 0.0044	± 0.0032	± 0.0065
1400 °C	5.65	0.00597	0.03841	0.1971	0.2001	0.3081
		± 0.00028	± 0.00101	± 0.0032	± 0.0018	± 0.0026
1800 °C		0.0066	0.0405	0.202	0.202	0.308
	0.155	± 0.0014	± 0.0046	± 0.011	± 0.012	± 0.013
Total	8.2	0.00602	0.0387	0.1953	0.1991	0.3085

SM 51-2	^{84}Kr	$^{78}Kr/^{84}Kr$	$^{80}Kr/^{84}Kr$	$^{82}Kr/^{84}Kr$	$^{83}Kr/^{84}Kr$	$^{86}Kr/^{84}Kr$
1800 °C	8.03	0.00607	0.03883	0.1910	0.1958	0.3067
		± 0.00038	± 0.00146	± 0.0043	± 0.0044	± 0.0042

Table S17. Isotopic ratios of Xe in the Sutter's Mill CM Chondrite. Concentrations are in the unit of 10^{-9} cm^3-STP/g.

SM 43-2	^{132}Xe	$^{124}Xe/^{132}Xe$	$^{126}Xe/^{132}Xe$	$^{128}Xe/^{132}Xe$	$^{129}Xe/^{132}Xe$
600 °C	0.617	0.00350 ± 0.00017	0.00329 ± 0.00024	0.0753 ± 0.0022	1.080 ± 0.013
900 °C	2.04	0.00440 ± 0.00028	0.00383 ± 0.00013	0.0813 ± 0.0013	1.066 ± 0.008
1400 °C	6.38	0.004243 ± 0.000076	0.00396 ± 0.00011	0.0813 ± 0.0010	1.0461 ± 0.0030
1800 °C	0.261	0.00407 ± 0.00033	0.00405 ± 0.00057	0.0847 ± 0.0029	1.066 ± 0.024
Total	9.30	0.00422	0.00389	0.0810	1.053

SM 43-1	^{132}Xe	$^{124}Xe/^{132}Xe$	$^{126}Xe/^{132}Xe$	$^{128}Xe/^{132}Xe$	$^{129}Xe/^{132}Xe$
1800 °C	10.1	0.00415 ± 0.00019	0.003835 ± 0.000057	0.07945 ± 0.00079	1.0460 ± 0.0014

SM 51-1	^{132}Xe	$^{124}Xe/^{132}Xe$	$^{126}Xe/^{132}Xe$	$^{128}Xe/^{132}Xe$	$^{129}Xe/^{132}Xe$
600 °C	0.380	0.00407 ± 0.00053	0.00345 ± 0.00027	0.0760 ± 0.0029	1.036 ± 0.012
900 °C	1.94	0.00439 ± 0.00026	0.00400 ± 0.00027	0.0810 ± 0.0009	1.064 ± 0.006
1400 °C	7.51	0.00423 ± 0.00019	0.00393 ± 0.00008	0.0804 ± 0.0007	1.048 ± 0.004
1800 °C	0.252	0.00445 ± 0.00076	0.00397 ± 0.00071	0.0818 ± 0.0019	1.048 ± 0.013
Total	10.1	0.00426	0.00393	0.0804	1.051

SM 51-2	^{132}Xe	$^{124}Xe/^{132}Xe$	$^{126}Xe/^{132}Xe$	$^{128}Xe/^{132}Xe$	$^{129}Xe/^{132}Xe$
1800 °C	9.57	0.00423 ± 0.00013	0.00387 ± 0.00016	0.0798 ± 0.0006	1.041 ± 0.004

Cosmogenic ^{21}Ne concentrations are very low and not easy to estimate for this meteorite. We assume that Ne isotopic ratios initially trapped in the meteorite were those plotted on mixing lines; one is connecting Solar-Ne and P3-Ne and another P3-Ne and Ne-E, then isotopic ratios of trapped Ne for each fraction can be calculate as the coordinates of the intersection between the mixing line and a line connecting cosmogenic Ne and measured isotopic ratios for each fraction as shown in Fig. S27. Concentrations of cosmogenic ^{21}Ne and cosmic-ray exposure ages obtained for each fraction are summarized in Table S18. An average exposure age of 0.051 ± 0.006 My is obtained for this meteorite using a production rate of 2×10^{-9} cm^3-STP/g/My (*14*). The production rate is proposed for an object smaller than ~10 cm in radius or near surface of larger object. The production rate increases up to ~50% in large object (R > ca. 25 cm). The short exposure age is an important characteristic of the Sutter's Mill meteorite.

Table S17 (cont.).

SM 43-2	^{132}Xe	$^{130}Xe/^{132}Xe$	$^{131}Xe/^{132}Xe$	$^{134}Xe/^{132}Xe$	$^{136}Xe/^{132}Xe$
600 °C	0.617	0.1551 ±0.0045	0.811 ± 0.011	0.387 ± 0.011	0.3252 ± 0.0085
900 °C	2.04	0.1612 ±0.0026	0.8280 ± 0.0063	0.3915 ± 0.0019	0.3359 ± 0.0047
1400 °C	6.38	0.1628 ±0.0016	0.8226 ± 0.0043	0.3812 ± 0.0033	0.3172 ± 0.0024
1800 °C	0.261	0.1654 ±0.0040	0.833 ± 0.017	0.387 ± 0.010	0.3225 ± 0.0059
Total	9.30	0.1620	0.8233	0.3840	0.3220

SM 43-1	^{132}Xe	$^{130}Xe/^{132}Xe$	$^{131}Xe/^{132}Xe$	$^{134}Xe/^{132}Xe$	$^{136}Xe/^{132}Xe$
1800 °C	10.1	0.16126 ±0.00088	0.8188 ± 0.0053	0.3859 ± 0.0024	0.3164 ± 0.0017

SM 51-1	^{132}Xe	$^{130}Xe/^{132}Xe$	$^{131}Xe/^{132}Xe$	$^{134}Xe/^{132}Xe$	$^{136}Xe/^{132}Xe$
600 °C	0.380	0.1610 ±0.0035	0.8111 ± 0.0151	0.3827 ± 0.0040	0.3149 ± 0.0050
900 °C	1.94	0.1609 ±0.0029	0.8175 ± 0.0078	0.3923 ± 0.0036	0.3344 ± 0.0042
1400 °C	7.51	0.1630 ±0.0008	0.8249 ± 0.0032	0.3824 ± 0.0011	0.3186 ± 0.0012
1800 °C	0.252	0.1628 ±0.0036	0.8211 ± 0.0087	0.3791 ± 0.0075	0.3149 ± 0.0060
Total	10.1	0.1625	0.8228	0.3842	0.3214

SM 51-2	^{132}Xe	$^{130}Xe/^{132}Xe$	$^{131}Xe/^{132}Xe$	$^{134}Xe/^{132}Xe$	$^{136}Xe/^{132}Xe$
1800 °C	9.57	0.1618 ±0.0014	0.8243 ± 0.0036	0.3845 ± 0.0030	0.3231 ± 0.0026

Argon isotopic ratios also show that Ar in these samples are mostly primitive trapped components as indicated by $^{38}Ar/^{36}Ar$ ratios of ca. 0.188 and low $^{40}Ar/^{36}Ar$ ratios less than 25 except for 600 ºC fractions, to which atmospheric contamination is observed (Table S15).

Isotopic ratios of Kr and Xe (Table S16 and S17) are almost identical with those of Q-Kr and Xe. Isotopic ratios of Xe in 600 ºC fractions are affected by terrestrial atmospheric Xe. A small excess in ^{136}Xe in 900 ºC fractions indicates a presence of HL-Xe component trapped in presolar diamonds.

The $^{40}Ar/^{36}Ar$ ratios for the meteorite samples are higher than the primitive value of 10^{-4}. The increase in $^{40}Ar/^{36}Ar$ ratios was caused by in-situ produced ^{40}Ar from ^{40}K in the meteorite, or addition of contaminating terrestrial atmospheric Ar with high value of 296 after fall to the earth. Upper limit of K-Ar age for these samples can be estimated using the total ^{40}Ar concentrations and K concentrations. For the measured K concentration of 363 ppm (Table S7), K-Ar ages become as young as 2.4-3.9 Gy, while ca. 4.5 Gy is obtained when the abundance of K is100-200 ppm K in the sample studied here. The calculation suggests a low K concentration for this particular sample, or the K-Ar system is disturbed due to a recent heating event(s).

Table S18. Overview of Cosmic Ray Exposure Age measurements for noble gases.

Sample	Temp. °C	^{21}Ne-cosm 10^{-9} cm^3-STP/g	±	T_{21} My	± My
SM43-2	600	0.0065	0.0044		
	900	0.0747	0.0173		
	1400	0.0092	0.0113		
	1800	0.0007	0.0028		
	Total	0.0912	0.0213	0.046	0.011
SM43-1	1800	0.0991	0.0200	0.050	0.010
SM51-1	600	0.0138	0.0050		
	900	0.0731	0.0149		
	1400	0.0163	0.0145		
	1800	0.0106	0.0048		
	Total	0.1139	0.0220	0.057	0.011
SM51-2	1800	0.1039	0.0285	0.052	0.014
			Average	0.051	0.006

2.11. X-ray Tomography

SM3, 9, 18, 51, and 54 were shipped to AMNH in Al foil in Ziploc bags, handled with latex gloves, and mounted in cylinders of Scotch transparent tape. X-ray computed tomography (CT) scanning (*20*) was performed on the entirety of each stone (Table S19) on the GE Phoenix VtomexS scanner at AMNH, at 1000 ms exposure, with voltages 110-130 kV, and currents 120-150 nA, in horizontal and vertical tiles, usually with a 0.1mm Cu beam filter Reconstructed density maps were output as stacks of TIF format files with 16-bit values describing the x-ray attenuation of each cubic volume element (voxel) in the field of view. Volumes were computed from scans using ImageJ and Volume Graphics software.

Table S19. CT imaging studies. Sample mass, CT resolution (μm per voxel edge), number of image stacks, measured volume (mm^3), and computed density (g/cm^3) are listed.

Scan label	Mass (g)	Resolution (μm/vxl)	Tiles	Volume (mm^3)	Density (g/cm^3)	Lab
SM3_22A	4.950	22.189	1	2200.0	2.250	AMNH
SM9_24A	6.235	24.543	1	2685.7	2.322	AMNH
SM18_14A	5.317	13.975	4	2466.5	2.156	AMNH
SM51_30A	8.990	30.765	1	3860.2	2.329	AMNH
SM51_14A	8.990	14.348	6	4004.6	2.245	AMNH
SM51*	8.990	16.670	1	3812.0	2.358	UCD
SM54_12B	4.140	12.175	4	1855.1	2.232	AMNH
SM73*	8.170	22.57	1	3452.0	2.367	UCD

SM 51 and SM73 were also imaged at the Center for Molecular and Genomic Imaging at UC Davis. X-ray tomographic images were obtained with a MicroXCT-200 specimen CT scanner (Xradia Inc.). The CT scanner has a variable x-ray source capable of a voltage range of 20-90kV with 1-8W of power. The samples were secured in place using custom-built holders such that the samples did not come in contact with any adhesive material. Samples were mounted on the scanners sample stage, which has submicron level of position adjustments. Scan parameters were adjusted as needed. First the source and detector distances were adjusted based on sample size and the optimal field of view for the given region of interest. Once the source and detector settings were established, the optimal x-ray filtration was determined for selecting among one of 12 filters. Following this procedure, the optimal voltage and power settings were determined. Series of images were reconstructed varying the center shift and beam hardening parameters to obtain optimized images. Images were reconstructed into 16-bit values.

Samples SM3 and SM9 appear to contain a dominant lithology characterized by abundant 200 to 400 μm diameter clasts (chondrules or CAIs), and 0.05 - 0.15 μm metal oxide or sulfide grains. A second lithology, with higher average atomic mass (Z) matrix and more abundant clasts, appears as irregular, angular lithic fragments many mm in size. At least one metal grain ~250 μm across, was observed, surrounded by a halo ~750 μm wide, of oxidized or sulfidized metal. It is unlikely that such a grain would be sampled by random cutting. Several clasts larger than 1 mm include a low-Z spherical object that appears to be concentrically zoned, and a similar object with zoned high-Z (metal) and low-Z (silicate) layers. Other large clasts are irregular, blocky objects. While the samples are fractured, and metal grains appear to be altered, no high-Z veins (e.g., FeO-rich) are observed.

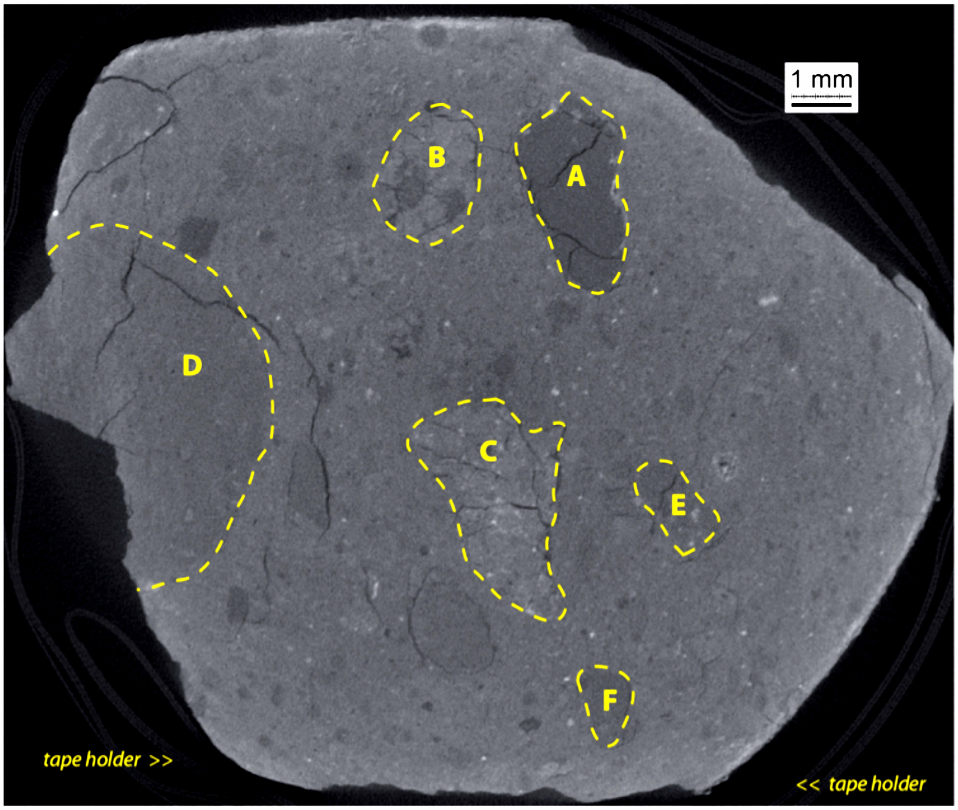

Fig. S28. Fractures surround multiple clasts in SM18 (slice SM18_14A_Z_s1_165, image contrast enhanced). Six clasts are outlined as recognized by scrolling through the slices above and below this slice. Contrasts in average atomic mass (brighter is heavier) and texture are evident. Note that fractures in 'C' do not extend beyond clast boundaries; fractures in 'B' extend from low-Z spherical objects, probably chondrules; some lithic fragments appear to contain chondrules, while others do not.

The meteorites studied so far exhibit a dominant, primary lithology that is the host for multiple types of exotic lithic clasts (Fig. S28). With more samples examined with CT, a more clear description may emerge. The image shown here is 8-bit, with severely compromised dynamic range due to file size constraint. Further X-ray tomography data are available from the American Museum of Natural History at http://dx.doi.org/10.5531/sd.eps.1 as well as from UC Davis at http://www.youtube.com/user/YinLabatUCDavis and
at http://www.youtube.com/user/spelunkerucd/videos .

2.12. Neutron Tomography

Neutron imaging is a nondestructive technique that is complementary to X-ray imaging. Unlike X-rays, neutrons do not interact (or negligibly so at most) with electrons. The interaction cross-section for X-rays monotonically increases with the number of electrons, i.e. with atomic number (Fig. S29). For neutrons, however, no direct correlation between neutron cross-section and atomic number exists. Neutrons directly probe nuclei, giving strong contrast for some elements that are close to one another in the periodic table, and are even able to distinguish between different isotopes. Several light elements (notably hydrogen) attenuate neutrons strongly, while even thick layers of many metals can be penetrated; lead, for example, is used for shielding X-rays, but is almost transparent for neutrons.

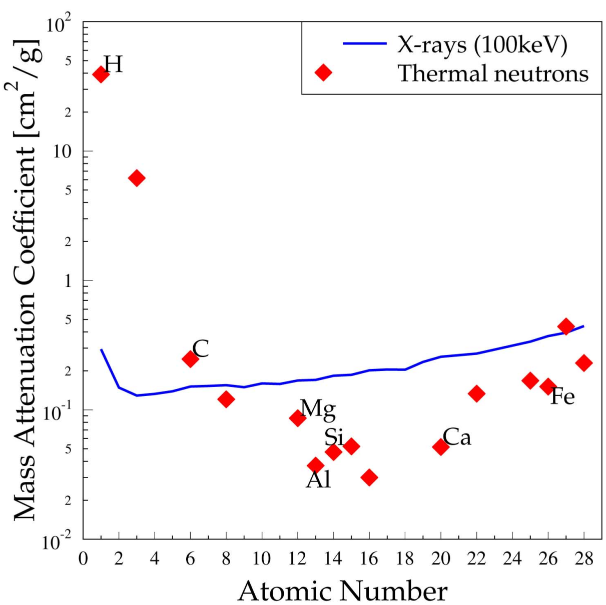

Fig. S29. Mass attenuation coefficient as a function of atomic number, adapted from (*100*).

Traditional neutron radiography provides information on the total attenuation integrated over the path of the neutrons through the material. The actual distribution of materials across that path cannot be extracted in detail. Neutron computed tomography (NCT) is based on radiography but provides a three-dimensional picture of the sample including the actual distribution of materials throughout the whole sample.

The tomography data was obtained at the University of California, Davis McClellan Nuclear Research Center (MNRC). The sample was mounted on a turntable where it was exposed to neutrons. The tomography system utilizes a Li_6F-ZnS-Cu scintillation screen to convert the neutrons into visible light. The green light produced by the scintillator is focused onto a 4 Megapixel CCD camera. In order to obtain the tomography data, 190 radiographs were taken after every 1° rotation. The exposure time was 45 s for each radiograph at a neutron fluence of 5×10^6 n/cm^{2}s. The radiographs are corrected for dark current and the flat field before reconstruction using the Imgrec software package developed at Lawrence Livermore National Laboratory. The resulting voxel size was 116.3 μm. More details can be found in (*101,102*).

Fig. S30. Reconstructed neutron tomography images of SM54, left: horizontal cut (slice 250), right: vertical cut (slice 293).

Figure S30 (left, slice 250) shows a reconstructed horizontal cut through the SM54 specimen, with two broken parts seen as well as the aluminum cup that served as sample holder. Figure S30 (right, slice 293) is a reconstructed image showing a vertical cut through the larger of the two parts, the ring around the sample is the aluminum wall of the sample holder. In both images dark inclusions can be seen, these inclusions are quite transparent to neutrons and could be rich in iron, calcium, aluminum or other elements with low neutron cross-sections. The light inclusions that can be seen on the lower left part of Fig. S30 (left) and in the right of Fig. S30 (right) are rich in elements that highly absorbent to neutrons such as hydrogen and carbon. Neutron tomography results are available for download from the UC Davis website http://mnrc.ucdavis.edu/data/SuttersMill/index.html as well as for viewing on the YouTube site at http://www.youtube.com/user/YinLabatUCDavis .

2.13. Cosmogenic Radionuclides

The concentrations of short-lived cosmogenic radionuclides, as well as long-lived cosmogenic ^{26}Al and natural radioactivity, were measured using non-destructive gamma-ray spectroscopy. One fragment of Sutter's Mill (SM36) was measured in the ultra low background counting facility STELLA (SubTerranean Low Level Assay) in the underground laboratories at the Laboratori Nazionali del Gran Sasso (LNGS) in Italy, using a high-purity germanium (HPGe) detectors of 414 cm^3 (*103*). The specimen was measured at the LNGS only 32 days after the fall, so that also very short-lived radionuclides such as ^{48}V (half life = 16 d) and ^{51}Cr (27.7d) could still be detected. The counting time was about two weeks. The counting efficiencies were calculated using a Monte Carlo code. This code is validated through measurements and analyses of samples of well-known radionuclide activities and geometries. The uncertainties in the radionuclide activities are dominated by the uncertainty in the counting efficiency, which is conservatively estimated at 10%. Tables 20a and 20b summarize the cosmogenic radionuclide concentrations and the content of natural radioactivity in the sample.

Table S20a. Massic activity (corrected to the time of fall) of cosmogenic radionuclides (in dpm kg^{-1}) in the 22.3 g specimen SM36 of the Sutter's Mill SM36 meteorite measured by non-destructive gamma-ray spectroscopy (*103*). Errors include a 1 sigma uncertainty of ~10% in the detector efficiency calibration.

Nuclide	Half-life	Energy (keV)	Massic activity (dpm/kg)
^{48}V	16.0 d	983.5/1311.6	17 ± 6
^{51}Cr	27.7 d	320.07	82 ± 24
^{59}Fe	44.5 d	1099/1291	6 ± 3
^{7}Be	53.1 d	477.6	243 ± 29
^{58}Co	70.9 d	810.8	24 ± 3
^{56}Co	77.3 d	846.8/1238/2599	11 ± 2
^{46}Sc	83.8 d	889.3/1120	12 ± 2
^{57}Co	271.8 d	122.1/136	22 ± 2
^{54}Mn	312.3 d	834.8	189 ± 19
^{22}Na	2.60 y	1274.5/1785	122 ± 11
^{60}Co	5.27 y	1173.2/1332.5/2506	34.1 ± 2.7
^{26}Al	$7.05x10^5$ y	1808.7/2319	3.8 ± 0.8

Table S20b. Concentrations of primordial radionuclides in the 22.3 g specimen of the Sutter's Mill meteorite SM36 measured by nondestructive gamma-ray spectroscopy. Errors include a 1σ uncertainty of ~10% in the detector efficiency calibration.

Nuclide	Energy (keV)	Concentrations
U	242/295/352/609/1764/2204	15 ± 2 ng g^{-1}
Th	238/338/583/727/911/968/2614.5	40 ± 6 ng g^{-1}
K	1460.8	594 ± 62 μg g^{-1}

2.14. Ultra-high Resolution Mass Spectroscopy and Nuclear Magnetic Resonance Spectroscopy

Flow injection negative electrospray [ESI(-)] ultra high resolution 12 T FTICR mass spectrometry (*36*) was performed on 25 mg samples of SM2 and SM12, following extraction with LC/MS grade methanol (Fig. S31). Thousands of mass signals with good coverage of isotopologues could be converted into a few hundreds of C, H, O, N, S, P, Na bearing compositions, indicating less compositional and structural diversity than found in other carbonaceous chondrites, among which are several fresh carbonaceous chondrites such as CM2 Murchison (*36*), CM2 Maribo (*9*) and other carbonaceous chondrite types such as CV, CK, CO, CI and C-ungrouped.

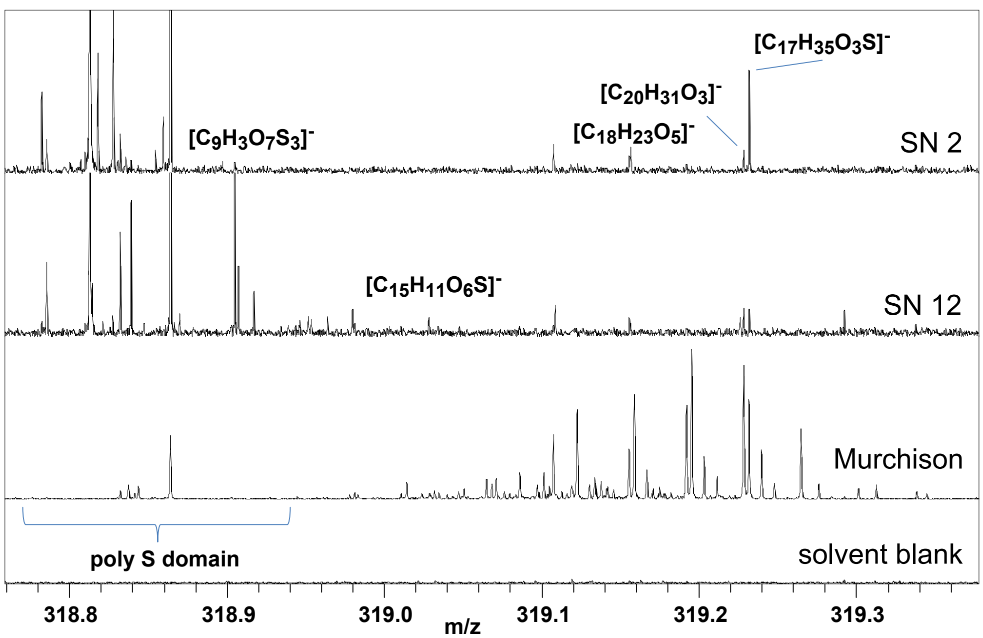

Fig. S31. FTICR/MS detail on nominal mass 319 of Sutter´s Mill samples SM2 and SM12 compared with CM2 Murchison and the methanol blank.

While Murchison methanolic extract shows more than hundred m/z signals and elemental compositions in the mass range 319.0 to 319.4 alone, SM2 and SM12 only show few signals corresponding to C, H, O, S type of molecules. SM2 and SM12 specifically exhibit many signals in the mass range 318.75 to 319.0 corresponding to oxygen rich and multiple sulphur containing compounds (poly-S domain). The characteristics found in nominal mass 319 as depicted here are repeated all over the mass spectra.

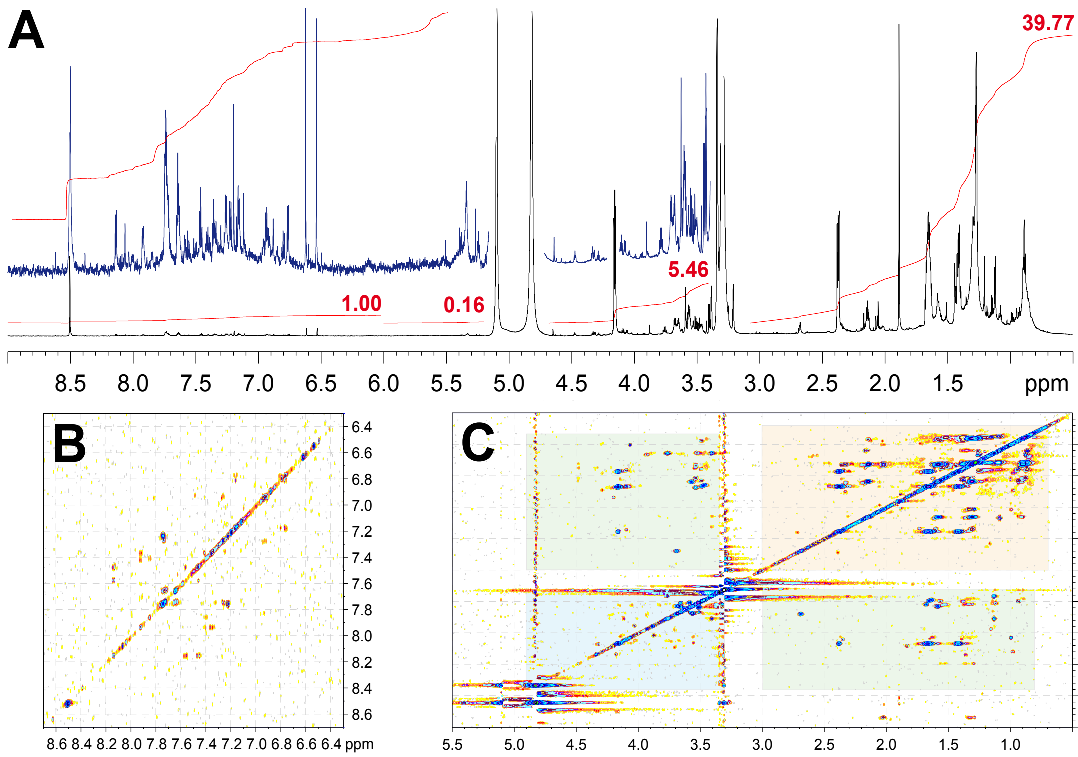

Fig. S32. 800 MHz ^{1}H NMR spectra of Sutter´s Mill methanolic extract. **(A)** one dimensional NMR spectrum, with vertical expansions (dark blue); red numbers: ^{1}H NMR section integrals. ^{1}H, ^{1}H TOCSY NMR spectra (mixing time: 70 ms) of **(B)** unsaturated and **(C)** saturated chemical environments with major connectivities indicated: C-CH-CH-C (orange), C-CH-CH-O (green), O-CH-CH-O (blue).

800 MHz ^{1}H NMR spectroscopy of methanolic SM12 Sutter´s Mill extract provided the highest proportion of branched aliphatics of any of the 20+ meteorites investigated so far using the same experimental procedure (Fig. S32). Polymethylene contributed for about ten percent to the purely aliphatic NMR resonances at $\delta_H < 1.9$ ppm. The ratio of hydrogen bound to sp^2 (unsaturated) and those bound to sp^3 carbons (saturated) was about 1:50; the OCH to CCH ratio was close to 1:8. Unsaturated protons fell in the δ_H range of 6.5 - 9 ppm, indicating the presence of olefins, oxygenated and carboxylated aromatics, nitrogen heterocycles and PAHs. Typical ^{1}H, ^{1}H spin systems encompassed C_{3-5} units. OCH-groups with δ_H: 3.3 - 4.5 ppm were bound to

aliphatic units rather than to other oxygenated aliphatics. In TOCSY NMR spectra, C-HC-CH-O units were commonly connected to intra aliphatic linkages (C-HC-CH-C) which were prevalent, whereas the ratio of C-HC-CH-O / O-HC-CH-O units was close to 12:1.

2.15. Raman Spectroscopy

Individual measurements of matrix macromolecular carbon (MMC) in Sutter's Mill SM12 and SM2 at the Carnegie Institution of Washington are plotted as a function of Raman G-band center and width in Fig. S33. The G band position is a function of mean crystallite size within the MMC, and the full width at half maximum (FWHM) is a function of the distribution of crystallite sizes within the material. When plotted together, these features define a thermal metamorphism trend proceeding with poorly crystalline, lightly heated material at upper right to polycrystalline, relatively annealed material at lower right.

The fragment of SM12 examined here (blue squares) shows evidence of heating to an intermediate degree between CO3 and CV3 chondrites. CM2 (green diamonds) has not experienced the same degree of annealing, but has been heated in excess of other CM2 chondrites. Error bars represent peak fitting uncertainties for each individual Raman spectrum.

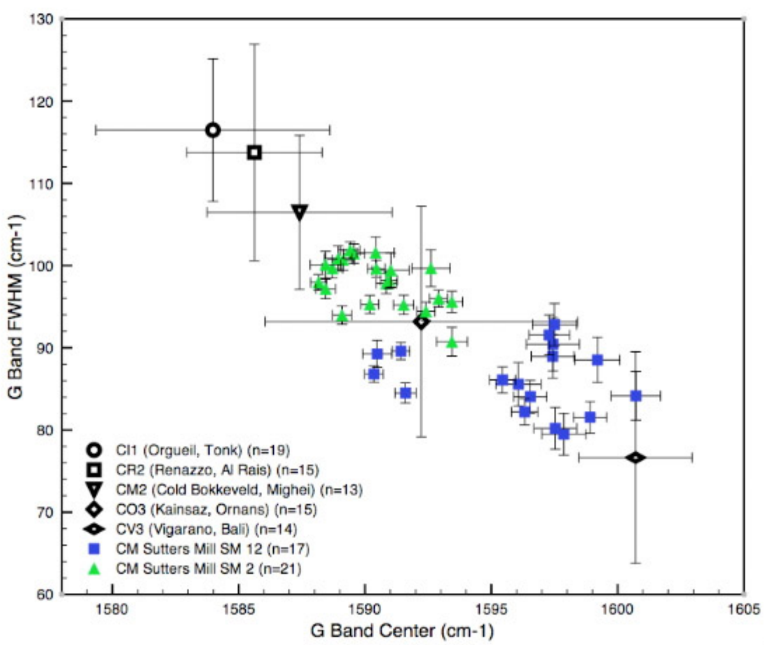

Fig. S33. Raman G-band center and Full Width at Half Maximum (FWHM).

2.16. Liquid Chromatography Mass Spectrometry

Amino acid measurements of a 240 mg chip of SM2 were made at the NASA Goddard Space Flight Center. The single SM2 chip was powdered in a ceramic mortar and pestle and a 146 mg aliquot was sealed in a test tube with 1 ml of Millipore Milli-Q Integral 10 (18.2 MΩ, < 1 ppb total organic carbon) ultrapure water and heated at 100°C for 24 h.

After heating, one half of the water extract was transferred to a separate glass tube, dried under vacuum, and the residue subjected to a 6 M HCl acid vapor hydrolysis procedure at 150°C for 3 h to determine total hydrolyzable amino acid content. The acid-hydrolyzed water extracts were desalted using cation-exchange resin (AG50W-X8, 100-200 mesh, hydrogen form, BIO-RAD), and the amino acids recovered by elution with 2 M NH_4OH (prepared from Millipore water and NH_3(g) (AirProducts, *in vacuo*). The remaining half of each water extract (non-hydrolyzed fraction) was taken through the identical desalting procedure in parallel with the acid-hydrolyzed extracts to determine the free amino acid abundances in the meteorites. The amino acids in the NH_4OH eluates were dried under vacuum to remove excess ammonia; the residues were then re-dissolved in 100 µL of Millipore water, transferred to sterile microcentrifuge tubes, and stored at -20°C prior to analysis. Based on our analysis of amino acid standards taken through the entire extraction and acid hydrolysis procedure, we found no evidence of significant decomposition, racemization, or thermal degradation of the amino acids during extraction or acid hydrolysis.

The amino acids in the NH_4OH eluates were derivatized with OPA/NAC for 15 minutes at room temperature. The abundance, distribution, and enantiomeric compositions of the two- to six-carbon aliphatic amino acids found in SM2 were then measured by ultra performance liquid chromatography fluorescence detection and time of flight mass spectrometry coupled with *o*-phthaldialdehyde/*N*-acetyl-L-cysteine (OPA/NAC) derivatization. The amino acids and their enantiomeric ratios were quantified from the peak areas generated from both fluorescence detection and from the mass chromatogram of their OPA/NAC derivatives. A more detailed description of the analytical technique and quantification methods used is described elsewhere (*39*). The reported amino acid abundances in SM2 below are the average value of three separate LC-FD/TOF-MS measurements (Table S22). The errors given are based on the standard deviation of the average value of three separate measurements.

Table S21. Summary of the amino acid abundances in parts-per-billion (ppb) in the free (non-hydrolyzed) and total (6M HCl- hydrolyzed) hot-water extracts of the Sutter's Mill (SM2) carbonaceous chondrite[a].

Amino Acid	Free (ppb)	Total (ppb)	Amino Acid	Free (ppb)	Total (ppb)
D-aspartic acid	13 ± 10	26 ± 5	L-aspartic acid	16 ± 1	59 ± 5
D-glutamic acid	< 2	29 ± 8	L-glutamic acid	4 ± 2	112 ± 3
D-serine	< 3	5 ± 1	L-serine	< 3	111 ± 12
glycine	72 ± 14	170 ± 20			
D-threonine	< 4	< 8	L-threonine	< 4	< 8
β-alanine	19 ± 11	45 ± 16			
γ-amino-n-butyric acid	3 ± 1	6 ± 3			
D-alanine	< 2	19 ± 16	L-alanine	< 2	35 ± 7
D-β-amino-n-butyric acid	< 2	< 5	L-β-amino-n-butyric acid	< 2	< 5
α-aminoisobutyric acid	< 2	< 5			
D-β-aminoisobutyric acid	< 2	2**	L-β-aminoisobutyric acid	< 2	2**
D-α-amino-n-butyric acid*	< 2	< 3	L-α-amino-n-butyric acid*	< 2	< 3
D-isovaline	< 3	< 8	L-isovaline	< 3	< 8
ε-amino-n-caproic acid***	2 ± 1	87 ± 23			
D-valine	< 4	< 13	L-valine	< 4	37 ± 11

Notes: [a]Extracts were analyzed by OPA/NAC derivatization and UPLC separation with UV fluorescence detection and TOF-MS detection at NASA Goddard Space Flight Center. The uncertainties are based on the standard deviation of the average value of three separate measurements. *Enantiomers could not be separated under the chromatographic conditions; **Tentative identification; ***Not detected by Arizona State University team at equal or higher than 10 ppb.

A similar sized sample of the Murchison had a complex distribution of amino acids with a total C_2 to C_5 amino acid abundance of ~14,000 parts-per-billion (ppb) (*39*). SM2, however, was confirmed to be highly depleted in amino acids and contained trace abundances ranging from ~5 to 170 ppb of glycine, β-alanine, γ-amino-*n*-butyric acid (γ-ABA), and ε-amino-*n*-caproic acid (EACA). Trace amounts of predominately the L-enantiomers of the protein amino acids aspartic and glutamic acids, alanine, serine, and valine were detected above procedural blank levels and indicate that SM2 experienced some terrestrial amino acid contamination after its fall to Earth. Since glycine, β-alanine, γ-ABA, and EACA are all achiral, compound specific carbon isotope

Table S22. Carbon and nitrogen composition and isotopic values from bulk elemental analysis-isotope ratio mass spectrometry. Sample SM2 has the lowest $\delta^{13}C$ and the highest $\delta^{15}N$ values.

Sample	Wt% C	N (ppm)	$\delta^{13}C$ (VPDB)	$\delta^{15}N$ (AIR)
SM2	1.32 ± 0.03	397 ± 7	-13 ± 1	+16.7 ± 0.3
SM12	1.56 ± 0.01	404 ± 29	2 ± 3	-0.2 ± 0.6
SM51	1.62 ± 0.04	405 ± 8	-3 ± 1	+6.2 ± 0.4

measurements will be necessary to establish the origin of these amino acids in SM2. Other non-protein amino acids that are rare on Earth, yet commonly found in other CM meteorites such as α-aminoisobutyric acid (α-AIB) and isovaline, were not identified in SM2 above ppb levels. However, both D- and L-β-AIB (~2 ppb total) were detected in SM2 and could be extraterrestrial in origin.

Bulk carbon and nitrogen abundance and isotopic data of samples SM2, SM12, and SM51 were measured at GSFC and are shown in Table S21. Measurements were acquired using a Costech ECS 4010 combustion elemental analyzer (EA) connected through a Thermo Conflo III interface to a Thermo MAT 253 isotope ratio mass spectrometer (IRMS). Three separate aliquots of each powdered sample (~7 to ~16 mg) were weighed in separate tin cups, folded into small sealed packets, and then loaded into the Costech zero-blank autosampler of the EA, which was purged with ultra-pure helium for 5 min. The tin cups were then dropped into the EA oven set at 1000°C, flash combusted and then subsequently oxidized and reduced to CO_2 and N_2. These gases were separated on a GC column before passing into the IRMS for isotopic measurement. An L-alanine standard of known isotopic composition ($\delta^{13}C$ = -23.33‰, $\delta^{15}N$ = -5.56‰, Iso-Analytical) was used to calibrate the bulk isotopic values measured for the meteorite sample. Carbon and nitrogen abundances were calculated by comparison of peak areas from the meteorite data with calibration curves of peak areas from known quantities of acetanilide. Errors for both abundances and isotopic values are standard deviations for triplicate measurements.

2.17. Gas Chromatography Mass Spectrometry

Two Sutter's Mill fragments were analyzed for soluble organic compounds by Gas Chromatography-Mass Spectrometry (GC-MS) of their water and solvent extracts at Arizona State University. 300 mg of SM2 were powdered in agate mortar, divided in two portions of 100 and 200 mg each and extracted in evacuated vials with, respectively, tripled distilled water and distilled dichlromethane/methanol (9:1 v:v) at 100ºC for 24 hours. A 1.2 g SM12 stone was chiseled into five fragments of approximate equal weight and incremental distance from the crust; these were powdered and extracted in sequence with water and solvent (same conditions as above).

The water extracts were dried cryogenically for the transfer of possible ammonia and amines (*104*) and then processed through (+) cation and (-) anion exchange resins for the separation and collection of amino acids, hydroxyacids and dicarboxylic acids, as described before (e.g., *105*).

Results for amino acids, a report of their decreased abundances with depth of the SM stone suggesting contamination for most as well as the searches of other water-soluble compounds are described in the main text. It should be noted here that the fragments of Sutter's Mill that we analyzed have been the only carbonaceous chondrite samples between those investigated so far not to release free or bound ammonia (*104*).

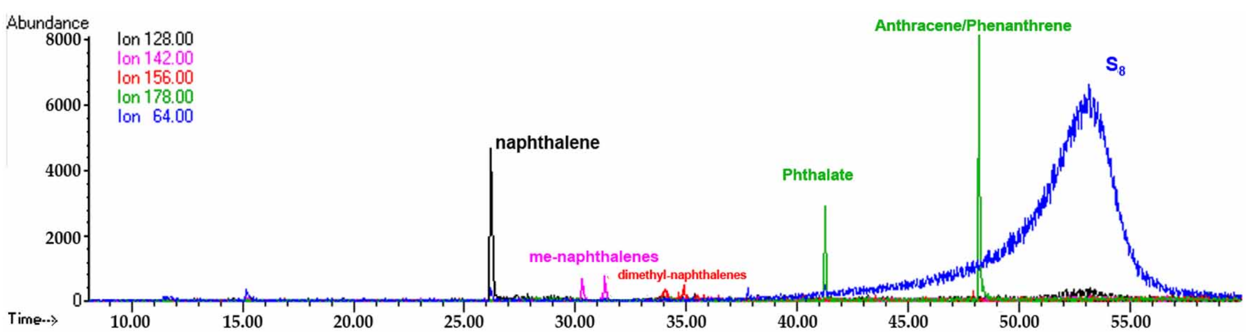

Fig. S34. Single ion GC-MS chromatogram of the aromatic hydrocarbons and sulfur detected in a SM2 solvent extract. Shown are naphthalene (m/z 128), two sets of its higher homologs, methyl- and dimethylnaphthalenes (m/z 142 and 156), a phthalate, antracene and/or phenanthrene (m/z 178), and octatomic sulfur (m/z 64).

The GC-MS analyses of a SM2 dichloromethane/methanol extract are shown in Fig. S34. The amounts of hydrocarbons detected in all SM samples were low and naphthalene was the most abundant compound, varying between samples 2-10 nanomoles/g. Besides the compounds shown, we also recognized in SM2 alkyl hydrocarbons but contamination was likely their source as they were found only as linear species, within a narrow range, 15ºC to 22ºC, and included phytane and two phthalates, known contaminants. The anthracene and/or phenanthrene shown in Fig. S34 was also a contaminant, as it was not found in interior SM12 fragments.

2.18. Thermoluminescence

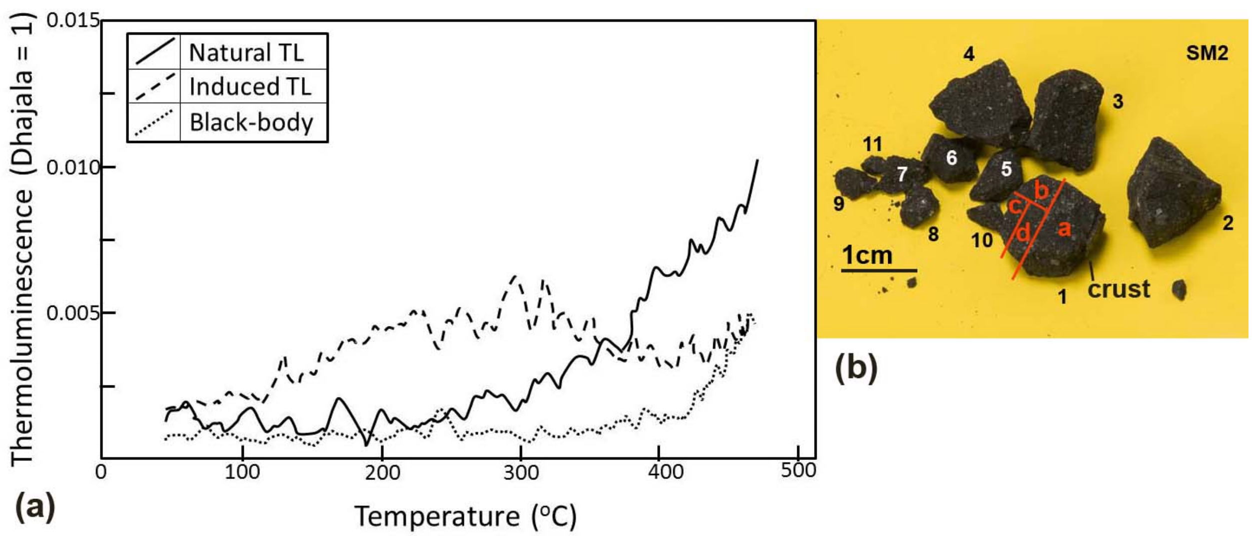

Fig. S35. Single Thermoluminescence (TL) glow curves **(a)** for Sutter's Mill fragment SM2-1d, identified in **(b)**. The luminescence produced (normalized to the TL induced intensity of the Dhajala meteorite which is used as a standard) is plotted against the temperature to which the sample is heated in the laboratory. The signal from the "as received" sample is termed "natural TL" while the signal produced by the sample after heating to 500ºC to remove the natural signal and then exposing to a 250 mCi ^{90}Sr beta source for three minutes is termed the "induced TL". Also shown is the black-body curve produced by the sample after its natural TL signal has been removed.

Thermoluminescence (TL) measurements were made using two separate 4 mg aliquots of SM2-1d, located 0.7-1.0 cm below the remaining fusion crust on fragment SM2-1 (Fig. S35). The samples were examined under the optical microscope, crushed with a pestle and mortar to ~200μm grains, and placed on 5-mm diameter copper pans for TL measurement. The TL was measured in the as received state ("natural TL") and after being irradiated by a dose of beta particles from a 250 mCi ^{90}Sr source ("induced TL"). The TL signal was measured on a Daybreak Nuclear and Medical TL instrument, modified to bring the sample closer to the detector, to screen off unwanted black body from the heating strip, and to incorporate a shutter so the detector (an EMI 96354Q PMT) remains on throughout the experiments. The resulting "glow curves" (plots of TL produced as a function of heating temperature in the laboratory) are shown in Fig. S35, along with the black body (background) curve. A weak but readily detectable signal was observed (S/N ~ 10) for Sutter's Mill in both the natural and induced states. This is unusual since the CM chondrites measured to date had no detectable TL signal. While the induced curve was broad and hummocky, and extended to low heating temperatures, the natural curve consisted of TL only in the higher temperature regions of the glow curve.

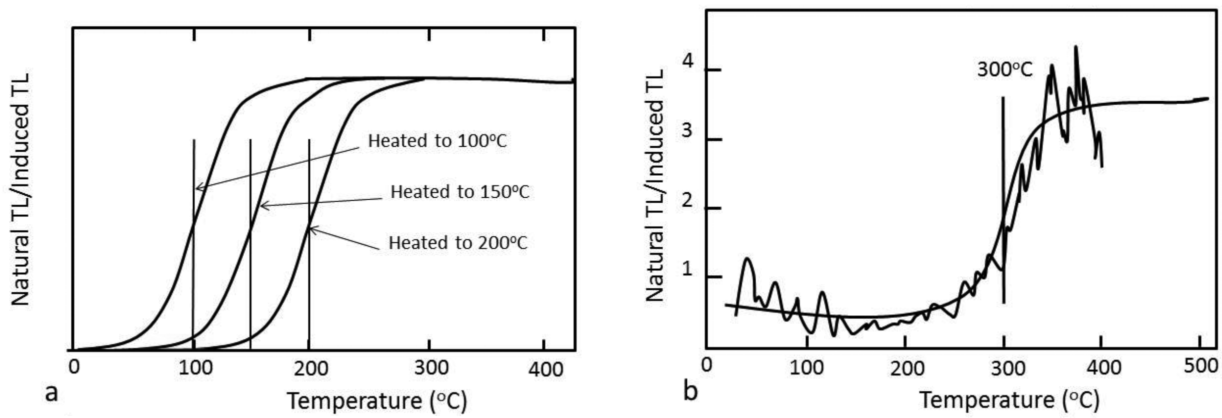

Fig. S36. Plot of the ratio of the natural TL to the induced TL as a function of glow curve temperature. Stepwise laboratory heating causes loss of low temperature TL in a way dependent on the heating temperature (a). The position of the step in the Sutter's Mill data (b) suggests that this meteorite has been heated to ~300ºC.

A ratio of natural TL to induced TL, referred to as the plateau curve (Fig. S36), shows a step at 300±20ºC, suggesting that these two samples of meteorite had been heated to about 300ºC and had not had time for their TL to recover (estimated to take ~0.2 My). This heating event may have been due to passage through the Earth's atmosphere, when temperatures as high as 300ºC may have reached 5-6 mm into the meteorite, although other heating events in the past ~0.2 My, such as recent solar or impact heating, cannot be excluded. The shape and the intensity of the induced TL curve resembles those commonly observed for low petrologic type chondrites (say 3.0-3.1) of the ordinary, CV, and CO classes, but is not identical to anything seen before. This suggests that Sutter's Mill is a unique low petrologic grade chondrite.

References

1. M. Fries, J. Fries, Doppler weather radar as a meteorite recovery tool. *Meteorit. Planet. Sci.* **45**, 1476 (2010). doi:10.1111/j.1945-5100.2010.01115.x

2. P. Jenniskens, M. Zolensky, Sutter's Mill (C). *Meteorit. Bull.* **46**, 1 (2012).

3. Materials and methods are available as supplementary materials on *Science* Online.

4. D. R. Christie, P. Campus, in *Infrasound Monitoring for Atmospheric Studies*, A. Le Pichon, E. Blanc, A. Hauchecorne, Eds. (Springer, Dordrecht, Netherlands, 2010), pp. 29−75.

5. T. A. Ens, P. G. Brown, W. N. Edwards, E. A. Silber, Infrasound production of bolides: A global statistical study. *J. Atmos. Sol. Terr. Phys.* **80**, 208 (2012). doi:10.1016/j.jastp.2012.01.018

6. E. A. Silber, A. Le Pichon, P. Brown, Infrasound detection of a near-Earth object impact over Indonesia on 8 October, 2009. *Geophys. Res. Lett.* **38**, L12201 (2011). doi:10.1029/2011GL047633

7. M. H. Shaddad *et al*., The recovery of asteroid 2008 TC3. *Meteorit. Planet. Sci.* **45**, 1557 (2010). doi:10.1111/j.1945-5100.2010.01116.x

8. K. D. Smith *et al*., Evidence for deep magma injection beneath Lake Tahoe, Nevada-California. *Science* **305**, 1277 (2004). doi:10.1126/science.1101304 Medline

9. H. Haack *et al*., Maribo–A new CM fall from Denmark. *Meteorit. Planet. Sci.* **47**, 30 (2012). doi:10.1111/j.1945-5100.2011.01311.x

10. H. Haack *et al*., in *Workshop on the First Solids in the Solar System*, 7 to 9 November 2011, Koloa, Kauai, Hawai'i (Lunar and Planetary Institute, Houston, TX, 2011), abstr. 9100.

11. K. Nishiizumi, M. W. Caffee, Exposure histories of CM2 carbonaceous chondrites–Update. *Meteorit. Planet. Sci.* **44** (suppl.), 5358 (2009).

12. U. Ott, Noble gases in meteorites–Trapped components. *Rev. Mineral. Geochem.* **47**, 71 (2002). doi:10.2138/rmg.2002.47.3

13. V. S. Heber *et al*., Noble gas composition of the solar wind as collected by the Genesis mission. *Geochim. Cosmochim. Acta* **73**, 7414 (2009). doi:10.1016/j.gca.2009.09.013

14. I. Leya, H.-J. Lange, S. Neumann, R. Wieler, R. Michel, The production of cosmogenic nuclides in stony meteoroids by galactic cosmic-ray particles. *Meteorit. Planet. Sci.* **35**, 259 (2000). doi:10.1111/j.1945-5100.2000.tb01775.x

15. M. Gounelle *et al*., in *The Solar System Beyond Neptune*, M. A. Barucci, H. Boehnhardt, D. P. Cruikshank, A. Morbidelli, Eds. (Univ. of Arizona Press, Tucson, AZ, 2008), pp. 525–541.

16. D. Nesvorný *et al*., Cometary origin of the zodiacal cloud and carbonaceous micrometeorites: Implications for hot debris disks. *Astrophys. J.* **713**, 816 (2010). doi:10.1088/0004-637X/713/2/816

17. K. J. Walsh, M. Delbo, W. F. Bottke, paper presented at the 44th American Astronomical Society/Division of Planetary Sciences Meeting, Reno, NV, 14 to 19 October, 2012, abstr. 305.04.

18. A. Tsuchiyama *et al*., Strength measurement of carbonaceous chondrites and micrometeorites using micro compression testing machine. *Meteorit. Planet. Sci.* **44** (suppl.), 5189 (2009).

19. O. Popova *et al*., Very low strengths of interplanetary meteoroids and small asteroids. *Meteorit. Planet. Sci.* **46**, 1525 (2011). doi:10.1111/j.1945-5100.2011.01247.x

20. D. S. Ebel, M. L. Rivers, Meteorite 3-D synchotron micro-tomography: Methods and applications. *Meteorit. Planet. Sci.* **42**, 1627 (2007). doi:10.1111/j.1945-5100.2007.tb00595.x

21. R. J. Macke, D. T. Britt, G. J. Consolmagno, Density, porosity and magnetic susceptibility of achondritic meteorites. *Meteorit. Planet. Sci.* **46**, 311 (2011). doi:10.1111/j.1945-5100.2010.01155.x

22. D. T. Britt *et al*., paper presented at the Meteoritical Society Meeting, Cairns, Australia, 12 to 17 August 2012, abstr. 5250.

23. M. S. Spergel, R. C. Reedy, O. W. Lazareth, P. W. Levy, L. A. Slatest, Cosmogenic neutron-capture-produced nuclides in stony meteorites. *J. Geophys. Res.* **91**, 483 (1986). doi:10.1029/JB091iB04p0D483

24. P. Rochette *et al*., Magnetic classification of stony meteorites: 2. Non-ordinary chondrites. *Meteorit. Planet. Sci.* **43**, 959 (2008). doi:10.1111/j.1945-5100.2008.tb01092.x

25. J. Gattacceca, P. Rochette, Toward a robust normalized magnetic paleointensity method applied to meteorites. *Earth Planet. Sci. Lett.* **227**, 377 (2004). doi:10.1016/j.epsl.2004.09.013

26. A. Bischoff, E. R. D. Scott, K. Metzler, C. A. Goodrich, in *Meteorites and the Early Solar System II*, D. S. Lauretta, H. Y. McSween Jr., Eds. (Univ. of Arizona Press, Tucson, AZ, 2006), pp. 679−712.

27. R. J. Walker *et al*., Comparative ^{187}Re-^{187}Os systematics of chondrites: Implications regarding early solar system processes. *Geochim. Cosmochim. Acta* **66**, 4187 (2002). doi:10.1016/S0016-7037(02)01003-7

28. Q-Z. Yin, K. Yamashita, A. Yamakawa, R. Tanaka, B. Jacobsen, D. S. Ebel, I. D. Hutcheon, and E. Nakamura, ^{53}Mn-^{53}Cr systematics of Allende chondrules and ε^{54}Cr-Δ^{17}O correlation in bulk carbonaceous chondrites. *Lunar Planet. Sci.* **XL**, abstr. 2006 (2009).

29. J. M. Friedrich, M.-S. Wang, M. E. Lipschutz, Comparison of the trace element composition of Tagish Lake with other primitive carbonaceous chondrites. *Meteorit. Planet. Sci.* **37**, 677 (2002). doi:10.1111/j.1945-5100.2002.tb00847.x

30. E. Tonui, M. E. Zolensky, M. E. Lipschutz, Petrography, mineralogy and trace element chemistry of Y-86029, Y-793321 and LEW 85332: Aqueous alteration and heating events. *Proc. NIPR Symp. Antarct. Meteorites* **15**, 38 (2002).

31. M. Haq, F. A. Hasan, D. W. G. Sears, C. B. Moore, C. F. Lewis, Thermoluminescence and the origin of the dark matrix of Fayetteville and similar meteorites. *Geochim. Cosmochim. Acta* **53**, 1435 (1989). doi:10.1016/0016-7037(89)90075-6

32. G. D. Cody *et al*., Organic thermometry for chondritic parent bodies. *Earth Planet. Sci. Lett.* **272**, 446 (2008). doi:10.1016/j.epsl.2008.05.008

33. E. D. Young, R. D. Ash, P. England, D. Rumble 3rd, Fluid flow in chondritic parent bodies: Deciphering the compositions of planetesimals. *Science* **286**, 1331 (1999). doi:10.1126/science.286.5443.1331 Medline

34. G. K. Benedix, L. A. Leshin, J. Farquhar, T. Jackson, M. H. Thiemens, Carbonates in CM2 chondrites: Constraints on alteration conditions from oxygen isotopic compositions and petrographic observations. *Geochim. Cosmochim. Acta* **67**, 1577 (2003). doi:10.1016/S0016-7037(02)01078-5

35. M. M. Grady, Astronomy by microscope. *Astron. Geophys.* **50**, 4.21 (2009).

36. P. Schmitt-Kopplin *et al.*, High molecular diversity of extraterrestrial organic matter in Murchison meteorite revealed 40 years after its fall. *Proc. Natl. Acad. Sci. U.S.A.* **107**, 2763 (2010). doi:10.1073/pnas.0912157107 Medline

37. G. W. Cooper, W. M. Onwo, J. R. Cronin, Alkyl phosphonic acids and sulfonic acids in the Murchison meteorite. *Geochim. Cosmochim. Acta* **56**, 4109 (1992). doi:10.1016/0016-7037(92)90023-C Medline

38. A. A. Monroe, S. Pizzarello, The soluble organic compounds of the Bells meteorite: Not a unique or unusual composition. *Geochim. Cosmochim. Acta* **75**, 7585 (2011). doi:10.1016/j.gca.2011.09.041

39. D. P. Glavin, M. P. Callahan, J. P. Dworkin, J. E. Elsila, The effects of parent body processes on amino acids in carbonaceous chondrites. *Meteorit. Planet. Sci.* **45**, 1948 (2010). doi:10.1111/j.1945-5100.2010.01132.x

40. J. R. Cronin, S. Pizzarello, Aliphatic hydrocarbons of the Murchison meteorite. *Geochim. Cosmochim. Acta* **54**, 2859 (1990). doi:10.1016/0016-7037(90)90020-L Medline

41. K. Lodders, Solar system abundances and condensation temperatures of the elements. *Astrophys. J.* **591**, 1220 (2003). doi:10.1086/375492

42. E. Jarosewich, R. S. Clarke Jr., J. N. Barrows, Eds., The Allende meteorite reference sample. *Smithson. Contrib. Earth Sci.* **27**, 1 (1986).

43. P. G. Brown *et al.*, The fall, recovery, orbit, and composition of the Tagish Lake meteorite: A new type of carbonaceous chondrite. *Science* **290**, 320 (2000). doi:10.1126/science.290.5490.320 Medline

44. R. N. Clayton, T. K. Mayeda, Oxygen isotope studies of carbonaceous chondrites. *Geochim. Cosmochim. Acta* **63**, 2089 (1999). doi:10.1016/S0016-7037(99)00090-3

45. R. N. Clayton, T. K. Mayeda, J. N. Goswami, E. J. Olsen, Oxygen isotope studies of ordinary chondrites. *Geochim. Cosmochim. Acta* **55**, 2317 (1991). doi:10.1016/0016-7037(91)90107-G

46. R. N. Clayton, T. K. Mayeda, A. E. Rubin, Oxygen isotope compositions of enstatite chondrites and aubrites. *J. Geophys. Res.* **89**, C245 (1984). doi:10.1029/JB089iS01p0C245

47. G. J. MacPherson *et al.*, The Kaidun chondrite breaccia: Petrology, oxygen isotopes, and trace element abundances. *Geochim. Cosmochim. Acta* **73**, 5493 (2009). doi:10.1016/j.gca.2009.06.012

48. E. D. Young, S. S. Russell, Oxygen reservoirs in the early solar nebula inferred from an Allende CAI. *Science* **282**, 452 (1998). doi:10.1126/science.282.5388.452

49. P. Jenniskens *et al.*, CAMS: Cameras for allsky meteor surveillance to establish minor meteor showers. *Icarus* **216**, 40 (2011). doi:10.1016/j.icarus.2011.08.012

50. P. Spurny *et al.*, in *Asteroids Comets Meteors 2012* (Niigata, Japan, 2011), abstr. 6369.

51. P. Brown *et al.*, The fall of the Grimsby meteorite–I. Fireball dynamics and orbit from radar, video, and infrasound records. *Meteorit. Planet. Sci.* **46**, 339 (2011). doi:10.1111/j.1945-5100.2010.01167.x

52. P. Spurný *et al.*, Analysis of instrumental observations of the Jesenice meteorite fall on April 9, 2009. *Meteorit. Planet. Sci.* **45**, 1392 (2010). doi:10.1111/j.1945-5100.2010.01121.x

53. P. Zolqdek, M. Wisniewski, K. Polakowski, Fireball over Denmark on 17 January 2009. *JIMO* **37**, 182 (2012).

54. H. Haack, R. Michelsen, G. Stober, D. Keuer, W. Singer, in *Meteoritical Society 2010*, New York, 26 to 30 July 2010 (2010), abstr. 5085.

55. E. P. Milley, thesis, University of Calgary, Calgary, Canada (2010).

56. P. Jenniskens *et al.*, The impact and recovery of asteroid 2008 TC(3). *Nature* **458**, 485 (2009). doi:10.1038/nature07920 Medline

57. M. Kozubal, F. W. Gasdia, R. F. Dantowitz, P. Scheirich, A. W. Harris, Photometric observations of Earth-impacting asteroid 2008 TC3. *Meteorit. Planet. Sci.* **46**, 534 (2011). doi:10.1111/j.1945-5100.2011.01172.x

58. P. Spurný *et al.*, The Bunburra Rockhole meteorite fall in SW Australia: Fireball trajectory, luminosity, dynamics, orbit, and impact position from photographic and photoelectric records. *Meteorit. Planet. Sci.* **47**, 163 (2012). doi:10.1111/j.1945-5100.2011.01321.x

59. P. A. Bland *et al.*, An anomalous basaltic meteorite from the innermost main belt. *Science* **325**, 1525 (2009). doi:10.1126/science.1174787 Medline

60. J. Llorca *et al.*, The Villalbeto de la Pena meteorite fall: I. Fireball energy, meteorite recovery, strewn field, and petrography. *Meteorit. Planet. Sci.* **40**, 795 (2005). doi:10.1111/j.1945-5100.2005.tb00155.x

61. P. Brown *et al.*, The orbit, atmospheric dynamics, and initial mass of the Park Forest meteorite. *Meteorit. Planet. Sci.* **39**, 1781 (2004). doi:10.1111/j.1945-5100.2004.tb00075.x

62. P. Spurný, J. Oberst, D. Heinlein, Photographic observations of Neuschwanstein, a second meteorite from the orbit of the Príbram chondrite. *Nature* **423**, 151 (2003). doi:10.1038/nature01592 Medline

63. J. Boroviĉka, P. Spurny, P. Kalenda, E. Tagliaferri, The Morávka meteorite fall: 1 Description of the events and determination of the fireball trajectory and orbit from video records. *Meteorit. Planet. Sci.* **38**, 975 (2003). doi:10.1111/j.1945-5100.2003.tb00293.x

64. A. R. Hildebrand *et al.*, The fall and recovery of the Tagish Lake meteorite. *Meteorit. Planet. Sci.* **41**, 407 (2006). doi:10.1111/j.1945-5100.2006.tb00471.x

65. P. Brown *et al*., The orbit and atmospheric trajectory of the Peekskill meteorite from video records. *Nature* **367**, 624 (1994). doi:10.1038/367624a0

66. P. Spurný, Recent fireballs photographed in central Europe. *Planet. Space Sci.* **42**, 157 (1994). doi:10.1016/0032-0633(94)90027-2

67. I. Halliday, A. T. Blackwell, A. A. Griffin, The Innisfree meteorite and the Canadian camera network. *J. R. Astron. Soc. Can.* **72**, 15 (1978).

68. I. Halliday, A. A. Griffin, A. T. Blackwell, Detailed data for 259 fireballs from the Canadian camera network and inferences concerning the influx of large meteoroids. *Meteorit. Planet. Sci.* **31**, 185 (1996). doi:10.1111/j.1945-5100.1996.tb02014.x

69. R. E. McCrosky, A. Posen, G. Schwartz, C.-Y. Shao, Lost City Meteorite–its recovery and a comparison with other fireballs. *J. Geophys. Res.* **76**, 4090 (1971). doi:10.1029/JB076i017p04090

70. Z. Ceplecha, Luminous efficiency based on photographic observations of the Lost City fireball and implications for the influx of interplanetary bodies onto Earth. *Astron. Astrophys.* **311**, 329 (1996).

71. Z. Ceplecha, Multiple fall of Pribram meteorites photographed. 1. Double-station photographs of the fireball and their relation to the meteorites. *BAC* **12**, 21 (1961).

72. E. A. Cloutis, P. Hudon, T. Hiroi, M. J. Gaffey, P. Mann, Spectral reflectance properties of carbonaceous chondrites: 2. CM chondrites. *Icarus* **216**, 309 (2011). doi:10.1016/j.icarus.2011.09.009

73. R. P. Binzel, A. W. Harris, S. J. Bus, T. H. Burbine, Spectral properties of near-earth objects: Palomar and IRTF results for 48 objects including spacecraft targets (9969) Braille and (10302) 1989 ML. *Icarus* **151**, 139 (2001). doi:10.1006/icar.2001.6613

74. J. L. Pouchou, F. Pichoir, A new model for quantitative x-ray microanalysis. Part I: Application to the analysis of homogeneous samples. *Rech. Aerosp.* **3**, 13 (1984).

75. R. E. Van Grieken, A. A. Markowicz, *Handbook of X-Ray Spectrometry*(Marcel Dekker, New York, ed. 2, 2002), vol. 29.

76. K.-J. Kim, in *X-Ray Data Booklet* (LBNL/PUB-490, Center for X-Ray Optics and Advanced Light Source, Lawrence Berkeley National Laboratory, Washington, DC), pp. 2-1–2-17.

77. M. F. Horan, R. J. Walker, J. W. Morgan, J. N. Grossman, A. E. Rubin, Highly siderophile elements in chondrites. *Chem. Geol.* **196**, 27 (2003). doi:10.1016/S0009-2541(02)00405-9

78. M. Fischer-Gödde, H. Becker, F. Wombacher, Rhodium, gold, and other highly siderophile element abundances in chondritic meteorites. *Geochim. Cosmochim. Acta* **74**, 356 (2010). doi:10.1016/j.gca.2009.09.024

79. W. Fujiya, N. Sugiura, H. Hotta, K. Ichimura, Y. Sano, Evidence for the late formation of hydrous asteroids from young meteoritic carbonates. *Nature Communications* **3**, 627 (2012). doi:10.1038/ncomms1635 Medline

80. M. R. Lee, P. Lindgren, M. R. Sofe, C. M. O'D Alexander, J. Wang, Extended chronologies of aqueous alteration in the CM2 carbonaceous chondrites: Evidence from carbonates in

Queen Alexandra Range 93005. *Geochim. Cosmochim. Acta* **92**, 148 (2012). doi:10.1016/j.gca.2012.06.005

81. W. R. Shields, T. J. Murphy, E. J. Catanzaro, E. L. Garner, Absolute isotopic abundance ratios and the atomic weigh of a reference sample of chromium. *J. Res. Natl. Bur. Stand.* **70A**, 193 (1966). doi:10.6028/jres.070A.016
82. A. Yamakawa, K. Yamashita, A. Makishima, E. Nakamura, Chemical separation and mass spectrometry of Cr, Fe, Ni, Zn, and Cu in terrestrial and extraterrestrial materials using thermal ionization mass spectrometry. *Anal. Chem.* **81**, 9787 (2009). doi:10.1021/ac901762a Medline
83. Q.-Z. Yin, From dust to planets: The tale told by moderately volatile elements. *Proc. the Astron. Soc. Pac.* **341**, 632 (2005).
84. H. Palme, Chemical and isotopic heterogeneity in protosolar matter. *Philos. Trans. R. Soc. London Ser. A* **359**, 2061 (2001). doi:10.1098/rsta.2001.0897
85. J. T. Wasson, G. W. Kallemeyn, Compositions of chondrites. *Philos. Trans. R. Soc. Lond.on Ser A* **325**, 535 (1988). doi:10.1098/rsta.1988.0066
86. F. Moynier, Q.-Z. Yin, B. Jacobsen, Dating the first stage of planet formation. *Astrophys. J.* **671**, L181 (2007). doi:10.1086/525527
87. D. P. Glavin, A. Kubny, E. Jagoutz, G. W. Lugmair, Mn-Cr isotope systematics of the D'Orbigny angrite. *Meteorit. Planet. Sci.* **39**, 693 (2004). doi:10.1111/j.1945-5100.2004.tb00112.x
88. Q.-Z. Yin, Y. Amelin, B. Jacobsen, in *40th Lunar & Planetary Science Conference* (Lunar and Planetary Institute, Houston, TX, 2009), abstr. 2060.
89. Y. Amelin, U-Pb ages of angrites. *Geochim. Cosmochim. Acta* **72**, 221 (2008). doi:10.1016/j.gca.2007.09.034
90. G. Brennecka, M. Wadhwa, Uranium isotope compositions of the basaltic angrite meteorites and the chronological implications for the early Solar System. *Proc. Natl. Acad. Sci. U.S.A.* **109**, 9299 (2012) and supporting online material.
91. B. Jacobsen *et al.*, ^{26}Al-^{26}Mg and ^{207}Pb-^{206}Pb systematics of Allende CAIs: Canonical solar initial ^{26}Al/^{27}Al ratio reinstated. *Earth Planet. Sci. Lett.* **272**, 353 (2008). doi:10.1016/j.epsl.2008.05.003
92. H. Warren, Stable-isotopic anomalies and the accretionary assemblage of the Earth and Mars: A subordinate role for carbonaceous chondrites. *Earth Planet. Sci. Lett.* **311**, 93 (2011). doi:10.1016/j.epsl.2011.08.047
93. J. Farquhar, M. H. Thiemens, Oxygen cycle of the Martian atmosphere-regolith system: Δ^{17}O of secondary phases in Nakhla and Lafayette. *J. Geophys. Res.* **105**, 11,991 (2000). doi:10.1029/1999JE001194
94. T. Sharp, A laser-based microanalytical method for the in-situ determination of oxygen isotope ratios of silicates and oxides. *Geochim. Cosmochim. Acta* **54**, 1353 (1990). doi:10.1016/0016-7037(90)90160-M

95. E. D. Young, H. Nagahara, B. O. Mysen, D. M. Audet, Non-Rayleigh oxygen isotope fractionation by mineral evaporation: Theory and experiments in the system SiO_2. *Geochim. Cosmochim. Acta* **62**, 3109 (1998). doi:10.1016/S0016-7037(98)00213-0

96. E. D. Young, A. Galy, H. Nagahara, Kinetic and equilibrium mass-dependent isotope fractionation laws in nature and their geochemical and cosmochemical significance. *Geochim. Cosmochim. Acta* **66**, 1095 (2002). doi:10.1016/S0016-7037(01)00832-8

97. M. F. Miller, Isotopic fractionation and the quantification of ^{17}O anomalies in the oxygen three-isotope system: An appraisal and geochemical significance. *Geochim. Cosmochim. Acta* **66**, 1881 (2002). doi:10.1016/S0016-7037(02)00832-3

98. A. B. Verchovsky *et al*., C, N, and noble gas isotopes in grain size separates of presolar diamonds from Efremovka. *Science* **281**, 1165 (1998). doi:10.1126/science.281.5380.1165

99. A. B. Verchovsky, M. A. Sephton, I. P. Wright, C. T. Pillinger, Separation of planetary noble gas carrier from bulk carbon in enstatite chondrites during stepped combustion. *Earth Planet. Sci. Lett.* **199**, 243 (2002). doi:10.1016/S0012-821X(02)00592-7

100. J. Banhart, Ed., *Advanced Tomographic Methods in Materials Research and Engineering* (Oxford Univ. Press, Oxford, 2008).

101. M. Wilding, C. E. Lesher, K. Shields, Application of neutron computed tomography in the geosciences. *Nucl. Instrum. Methods Phys. Res. A* **542**, 290 (2005). doi:10.1016/j.nima.2005.01.151

102. H.-Y. Tang *et al*., Developing a 3D neutron tomography method for proton exchange membrane fuel cells. *J. Power Sources* **195**, 6774 (2010). doi:10.1016/j.jpowsour.2010.03.060

103. C. Arpesella, A low background counting facility at Laboratory Nazionali del Gran Sasso. *Appl. Radiat. Isot.* **47**, 991 (1996). doi:10.1016/S0969-8043(96)00097-8

104. S. Pizzarello, W. Holmes, Nitrogen-containing compounds in two CR2 meteorites: ^{15}N composition, molecular distribution and precursor molecules. *Geochim. Cosmochim. Acta* **73**, 2150 (2009). doi:10.1016/j.gca.2009.01.022

105. S. Pizzarello, L. B. Williams, Ammonia in the early solar system: An account from carbonaceous meteorites. *Astrophys. J.* **749**, 161 (2012).